DOKUZ EYLÜL UNIVERSITY

GRADUATE SCHOOL OF NATURAL AND APPLIED SCIENCES

DEVELOPMENT AND CHARACTERIZATION OF Al_2O_3 COATINGS WITH DIFFERENT SURFACE MORPHOLOGIES BY ANODIC OXIDATION

by

Sezer BALKAN

September, 2024

İZMİR

DEVELOPMENT AND CHARACTERIZATION OF Al_2O_3 COATINGS WITH DIFFERENT SURFACE MORPHOLOGIES BY ANODIC OXIDATION

A Thesis Submitted to the
Graduate School of Natural and Applied Sciences of Dokuz Eylül University
In Partial Fulfillment of the Requirements for Master of Science in
Department of Nanoscience and Nanoengineering, Nanoscience and Nanoengineering Program

by

Sezer BALKAN

September, 2024

İZMİR

THESIS EXAMINATION RESULT FORM

We have read the thesis entitled **"DEVELOPMENT AND CHARACTERIZATION OF Al_2O_3 COATINGS WITH DIFFERENT SURFACE MORPHOLOGIES BY ANODIC OXIDATION"** completed by **SEZER BALKAN** under supervision of **ASSOC.PROF.DR. METİN YURDDAŞKAL** and we certify that in our opinion it is fully adequate, in scope and in quality, as a thesis for the degree of. Master of Science.

Assoc.Prof.Dr. Metin YURDDAŞKAL

Supervisor

Assoc. Prof. Dr. Tuncay DİKİCİ

Jury Member

Assist.Prof.Dr. Hüseyin Erdem YALKIN

Jury Member

Prof. Dr. Okan FISTIKOĞLU

Director

Graduate School of Natural and Applied Sciences

ACKNOWLEDGMENT

First of all, I would like to express my deepest gratitude to my advisor Assoc. Prof. Dr. Metin YURDDAŞKAL, for his continuous support, patience and guidance throughout my research journey. His invaluable knowledge, experience and encouragement have been instrumental in the completion of this thesis.

I would like to extend my gratitude to my esteemed professor, Assoc. Prof. Dr. Tuncay DİKİCİ, for his friendly attitude towards me and for sharing his valuable experiences.

I would like to thank my beloved girlfriend, İlayda YILDIRIM, who has always been my biggest supporter, standing by my side in every situation and boosting my morale. I would like to thank my dear friends Karun Kaan ÖLÇEN, Tuna Kaan KAYA, Berkay COŞKUN and Onur ÇETİNKAYA for their help me on difficult situations.

Finally, I would like to thank my entire family my mother Esen BALKAN, my father Sümer BALKAN and my sister Sezin BALKAN ERİŞTİREN for their unwavering support, both financially and emotionally, for believing in me and having faith in me from the very beginning.

Sezer BALKAN

DEVELOPMENT AND CHARACTERIZATION OF Al_2O_3 COATINGS WITH DIFFERENT SURFACE MORPHOLOGIES BY ANODIC OXIDATION

ABSTRACT

Aluminum samples were divided into three groups by applying different parameters. Group 1 includes anodized samples with varying voltages as well as non-anodized aluminum. Group 2 samples were anodized at 30V, with four samples being anodized at intervals of 30 minutes, starting from 30 minutes. Both Group 1 and Group 2 samples were subjected to heat treatment. Group 3 shares the same parameters as Group 2 but without heat treatment. The anodization process was carried out in two stages (two-step anodization). For Group 1 samples, after the first anodization lasting 1 hour, an etching process was performed, followed by another 1-hour anodization in the same electrolyte. The same method was applied to Group 2 and Group 3 (e.g., for A30-30: 30 minutes of first anodization - etching - 30 minutes of second anodization). The etching process lasted 1 hour for all samples. In this study, the characteristic properties of anodic aluminum oxide (AAO), such as pore diameter, interpore distance, wall thickness, barrier layer thickness, pore density, and porosity values were measured and compared with the literature. It was shown that the values aligned with the literature except for minor deviations. To obtain information about the surface morphology, a scanning electron microscope (SEM), an atomic force microscope (AFM), and a profilometer for surface roughness were used, and the numerical values of the characteristic properties were obtained using the ImageJ program. X-ray diffraction (XRD) was used to obtain the crystallographic properties of the material surface. In Group 1 samples anodized at different voltages, the pore diameter ranged from 15 to 40 nm, and the interpore distance varied between 51 and 82 nm. In Group 2 and Group 3 samples, these values ranged from 9 to 23 nm and 16 to 44 nm, respectively. It was demonstrated that the pore diameter and interpore distance increased with increasing voltage and duration. The applied heat treatment was found to have no effect on the characteristic properties. Additionally, it was shown that aluminum, which exhibited hydrophilic properties (44°) before anodization, gained hydrophobic properties after anodization, increasing this angle value to 78.4 degrees.

The application range of AAO membranes is quite broad in nanoscience. In light of these results, it has been shown that AAO with desired properties can be produced and that these properties can be easily altered, affecting the porous type membrane structure.

Keywords: Al_2O_3, nanostructures, anodization, anodic aluminum oxide, porous-type.

ANODİK OKSİTLEME YÖNTEMİ İLE FARKLI YÜZEY MORFOLOJİLERİNE SAHİP AL_2O_3 KAPLAMALARIN GELİŞTİRİLMESİ VE KARAKTERİZASYONU

ÖZ

Aluminyum numuneler farklı parametreler uygulanarak 3 gruba ayrılmıştır. Grup 1'de anotlanmamış aluminyum ile beraber farklı voltajlar uygulanarak anotlanan numuneler bulunmaktadır. Grup 2 numunelerine ise sadece 30V uygulanmış ancak 30 dakikadan başlamak üzere 4 numune olacak şekilde 30'ar dakika arayla anotlama yapılmıştır. Grup 1 ve Grup 2 numuneleri aynı zamanda ısıl işleme tabi tutulmuştur. Grup 3' ise Grup 2'nin aynı parametrelerine sahiptir ancak ısıl işlem uygulanmamıştır. Anotlama işlemleri iki aşamada gerçekleştirilmiştir (iki-adımlı anodizasyon). Grup 1 numunelerine 1 saat süren ilk anotlamanın ardından etching işlemi yapılmıştır ardından 1 saat daha aynı elektrolit içinde anotlama işlemi gerçekleştirilmiştir. Grup 2 ve grup 3 için de aynı yöntem uygulanmıştır. Dağlama işlemi tüm numuneler için 1 saattir. Bu çalışmada anodik aluminyum oksit (AAO)'lerın karakteristik özellikleri olan por çapı, porlar arası mesafe, duvar kalınlığı, bariyer katman kalınlığı, por yoğunluğu ve porozite değerleri ölçülmüş ve literatürle kıyaslama yapılmıştır. Literatürle kıyaslandığında değerlerin az miktarda sapma dışında örtüştüğü gösterilmiştir. Yüzeyin morfolojisi hakkında bilgi elde etmek için taramalı electron mikroskobu (SEM), atomik güç mikroskobu (AFM) ve yüzey pürüzlülüğü için profilometre kullanılmış ve karakteristik özelliklerin sayısal değerlerini elde etmek için ImageJ programından yararlanılmıştır. Malzeme yüzeyinin kristalografik özelliklerini elde etmek için X-ışını kırınımı (XRD) kullanılmıştır. Farklı voltajlar uygulanarak anotlanan grup 1 numunelerinde por çapı 15-40 nm, interpore distance değerleri ise 51-82nm aralığında değişiklik göstermiştir. Grup 2 ve grup 3 numunelerinde bu değerler sırasıyla 9-23 nm ve 16-44 nm aralığında değişmiştir. Por çapı ve porlar arası mesafe değerlerinin voltaj ve süre arttıkça arttığı ispatlanmıştır. Uygulunan ısıl işlemin karakteristik özelliklere etki etmediği görülmüştür. Buna ek olarak anotlamadan önce hidrofilik özellik gösteren (44^o) aluminyumun, anotlandıktan sonra bu açı değerini 78.4 derece arttırarak hidrofobik özellik kazandığı da gösterilmiştir. AAO membranların kullanım alanı oldukça geniştir. Bu sonuçların

ışığında istenilen özellikte AAO üretilmesi ve bu özelliklerin kolayca bir şekilde değiştirilmesinin porlu tip membran yapıya etkisi gösterilmiştir.

Anahtar kelimeler: Al_2O_3, nanoyapılar, anotlama, anodik aluminyum oksit, porlu yapı.

CONTENTS

Page

THESIS EXAMINATION RESULT FORM ii
ACKNOWLEDGMENT iii
ABSTRACT iv
ÖZ vi
CONTENTS viii
LIST OF FIGURES xi
LIST OF TABLES xv

CHAPTER ONE INTRODUCTION 1

1.1 Background 1
1.2 Application of Anodic Aluminum Oxide 3

CHAPTER TWO THEORETICAL BACKGROUND 5

2.1 Anodic Aluminium Oxide 5
2.1.1 Types of Anodic Aluminium Oxide 9
2.1.1.1 Barrier-Type Anodic Aluminum Oxide 10
2.1.1.2 Porous-Type Anodic Aluminum Oxide 12
2.1.2 Hard Anodization 15
2.1.3 Mild Anodization 15
2.1.4 Pulse Anodization 18
2.1.5 Cyclic Anodization 19
2.2 Structure of Porous Anodic Aluminum Oxide 19
2.2.1 Pore Diameter (Dp) 21
2.2.2 Interpore Distance (Dc) 23
2.2.3 Barrier Layer Thickness (B) 25
2.2.4 Wall Thickness (W) 28
2.2.5 Porosity 28
2.2.6 Pore Density (n) 29

2.3 Parameters Affecting the Anodic Aluminum Oxide Properties 30
2.3.1 Pre-Texturing 30
2.3.2 Incorporation of Anions 31
2.3.3 Temperature 33
2.3.4 Electrolyte 33
2.3.4.1 Sulfuric Acid (H_2SO_4) 33
2.3.4.1 Oxalic Acid ($C_2H_2O_4$) 34
2.3.4.2 Phosphoric Acid (H_3PO_4) 35
2.3.4.3 Chromic Acid (C_2CrO_4) 35
2.4 Properties of Anodic Aluminum Oxide Membranes 35

CHAPTER THREE MATERIALS AND METHODS 38

3.1 Materials 38
3.2 Method 38
3.2.1 Pore Analysis 39
3.2.2 Scanning Electron Microscope (SEM) Analysis 40
3.2.3 X-Ray Diffraction (XRD) Analysis 41
3.2.4 Atomic Force Microscope (AFM) Analysis 43
3.2.5 Water Contact Angle (WCA) Analysis 44
3.2.6 Surface Roughness Analysis 46

CHAPTER FOUR RESULTS & DISCUSSION 48

4.1 Morphological Analysis 48
4.2 Energy Dispersive Spectrometry (EDS) Analysis 55
4.3 Pore Analysis 56
4.4 XRD Analysis 61
4.5 AFM Analysis 65
4.6 Surface Roughness Analysis 76
4.7 Water Contact Angle Analysis 78

CHAPTER FIVE CONCLUSION & FUTURE WORKS..... 84

REFERENCES..... 85

LIST OF FIGURES

Page

Figure 2.1 Schematic diagram of (a) self-formed oxide layer and (b) the oxidation of anodizing processes. 6

Figure 2.2 Schematic diagram of the annotation mechanism. 7

Figure 2.3 The formation mechanism of the anodic film (Eftekhari, 2008). 8

Figure 2.4 Types and current density-time graphs of anodized aluminum (Domagalski et al., 2021). 9

Figure 2.5 Diffusion of aluminum cations through the oxide layer. 11

Figure 2.6 Parameters of porous-type anodization (Martínez-Viademonte et al., 2020). 12

Figure 2.7 Schematic illustration of the kinetics of porous AAO growth in galvanostic (A) and potentiostatic (B) regimes, with stages of anodic porous oxide development (C) (Eftekhari, 2008). 14

Figure 2.8 A schematic view of two-step mild anodization process for AAO (i) the first anodization step, (ii) removal of disordered porous AAO, and (iii) the second anodization step (Lee, 2010). 16

Figure 2.9 A schematic diagram of current – time for pulse anodization (Deacon Juhl, 2004)..... 18

Figure 2.10 A diagram of potential – time for cyclic anodization (Manzoor et al., 2023)..... 19

Figure 2.11 Ideally structure of AAO (Brudzisz et al., 2021)..... 20

Figure 2.12 Parameters influence on the pore diameter of AAO..... 23

Figure 2.13 Effect of anodizing potential on the barrier layer thickness for AAO in different electrolytes (Eftekhari, 2008) 27

Figure 2.14 Percentage of incorporated anions in the AAO (Eftekhari, 2008)..... 31

Figure 2.15 Schematic profiles of anion concentration in the barrier-type oxide layer in commonly used electrolytes (Eftekhari, 2008). 31

Figure 3.1 Schematic representation of the experiment. 39

Figure 3.2 Scanning electron microscope (Personal Archive) 40

Figure 3.3 Sputter coating (Personal Archive) 41

Figure 3.4 X-ray Diffraction (Personal Archive) 42

Figure 3.5 The operating principle of atomic force microscopy. 43

Figure 3.6 Atomic force microscope. 44

Figure 3.7 Three types of water droplets. 44

Figure 3.8 A contact angle of a water droplet. 44

Figure 3.9 Cassie-Baxter and Wenzel states. 45

Figure 3.10 Instrument used to measure water contact angle (Personal Archive). 45

Figure 3.11 Surface roughness instrument. 47

Figure 4.1 SEM graphs of (a) aluminum, (b) A20, (c) A30, (d) A40, (e) A50, (f) A60. 49

Figure 4.2 Graph of pore diameter values of Group 1. 50

Figure 4.3 Graph of interpore distance values of Group 1. 50

Figure 4.4 SEM images of Group 2. (a) A30-30, (b) A30-60, (c) A30-90, (d) A30-120. 51

Figure 4.5 Pore diameter values of Group 2. 52

Figure 4.6 Interpore distance values of Group 2. 52

Figure 4.7 SEM images of Group 3. (a) aluminum, (b) NA30-30, (c) NA30-60, (d) NA30-90, (e) NA30-120. 53

Figure 4.8 Pore diameter values of Group 3. 54

Figure 4.9 Interpore distance values of Group 3. 54

Figure 4.10 EDS values and SEM images of (a) non-anodized aluminum and (b) anodized aluminum. 55

Figure 4.11 Pore density values of Group 1. 59

Figure 4.12 Pore density values of Group 2. 60

Figure 4.13 Pore density values of Group 3. 60

Figure 4.14 XRD graph of aluminum. 62

Figure 4.15 XRD graphs of Group 1. 63

Figure 4.16 XRD graphs of Group 2. 64

Figure 4.17 XRD graphs of Group 3. 65

Figure 4.18 3D Z-Scan graphs of (a) aluminum, (b) A20, (c) A30, (d) A40, (e) A50, (f) A60. 66

Figure 4.19 Z-Scan and deflection graphs of (a-b) aluminum, (c-d) A20, (e-f) A30, (g-h) A40, (i-j) A50, (k-l) A60. 67

Figure 4.20 Deflection 3D and 2D graphs of (a-b) aluminum, (c-d) A20, (e-f) A30, (g-h) A40, (i-j) A50, (k-l) A60. 69

Figure 4.21 Z-scan 3d graphs of (a) A30-60, (b) A30-90 and (c) A30-120. 71

Figure 4.22 Z-Scan and deflection graphs of (a-b) A30-60, (c-d) A30-90, (e-f) A30-120. 72

Figure 4.23 3D and 2D deflection graphs of (a-b) A30-60, (c-d) A30-90, (e-f) A30-120. 73

Figure 4.24 Z-Scan graphs of (a) aluminum, (b) NA30-30, (c) NA30-60, (d) NA30-90, (e) NA30-120. 74

Figure 4.25 Z-Scan and deflection graphs of (a-b) aluminum, (c-d) NA30-30, (e-f) NA30-60, (g-h) NA30-90, (i-j) NA30-120. 75

Figure 4.26 Deflection 3D and 2D graphs of (a-b) aluminum, (c-d) NA30-30, (e-f) NA30-60, (g-h) NA30-90, (i-j) NA30-120. 76

Figure 4.27 Water contact angle images of Group 1. (a) aluminum, (b) A20, (c) A30, (d) A40, (e) A50, (f) A60. 78

Figure 4.28 Water contact angle images of Group 2. (a) A30-30, (b) A30-60, (c) A30-90, (d) A30-120. 79

Figure 4.29 Water contact angle images of Group 3. (a) aluminum, (b) NA30-30, (c) NA30-60, (d) NA30-90, (e) NA30-120. 80

Figure 4.30 Water contact angle values of Group 1..... 81

Figure 4.31 Water contact angle values of Group 2..... 81

Figure 4.32 Water contact angle values of Group 3..... 82

LIST OF TABLES

Page

Table 2.1 Bases used as electrolytes in the production of barrier-type AAO. 10

Table 2.2 Acids used as electrolytes in the production of porous-type AAO. 13

Table 2.3 Anodizing ratio (B_u) for several anodizing electrolytes 26

Table 2.4 Variation in sulphuric acid anodizing conditions according to product application. 34

Table 3.1 Experimental conditions applied during both anodizing steps for different samples. 38

Table 4.1 Pore diameter and interpore distance values of Group 1. 57

Table 4.2 Pore diameter and interpore distance values of Group 2. 57

Table 4.3 Pore diameter and interpore distance values of Group 3. 57

Table 4.4 Wall thickness, barrier layer thickness and wall thickness/barrier layer thickness values of Group 1 58

Table 4.5 Wall thickness, barrier layer thickness and wall thickness/barrier layer thickness values of Group 2 58

Table 4.6 Wall thickness, barrier layer thickness and wall thickness/barrier layer thickness values of Group 3 58

Table 4.7 Porosity values of Group 1,2 and 3. 61

Table 4.8 Surface roughness values of Group 1. 77

Table 4.9 Surface roughness values of Group 2. 77

Table 4.10 Surface roughness values of Group 3. 77

CHAPTER ONE
INTRODUCTION

1.1 Background

The rapidly advancing science and technology of today have become a significant force for overcoming the challenges humanity faces and pushing the boundaries to their limits. While technology is the turning point in human history, nanotechnology is the most impressive branch of this discipline. Nanotechnology is a multidisciplinary field used in changing, controlling and engineering the properties of nanoscale materials. The term nanotechnology, derived from the suffix "nano", refers to working at nanometer level. The foundation of nanotechnology was laid by physicist Richard Feynman in 1959, when he said "There is plenty of room at the bottom." at a conference. He also had the foresight that an encyclopedia could be studied at the nanoscale by imagining it written on the tip of a pin. In 1974, Norio Taniguchi first used the term "nanotechnology" for nano-sized materials (Var et al., 2015). Nanotechnology is used in many areas of technology and industry, including information technology, energy, environmental sciences, medicine, national security, food safety and transportation. This disciplinary field uses research and knowledge in chemistry, physics, materials science and biotechnology to add diverse and useful properties to materials (Mobasser & Firoozi, 2016). This technology has attracted a lot of attention from the scientific world recently, focusing on obtaining a wide variety of nanostructures by combining it with surface engineering. For instance, structures such as nanopores, nanotubes, nanowires and nanorods have been extensively researched (Eftekhari, 2008). Interest in nanomaterials has increased due to the properties that arise from the nano dimension and add to the material. One of the most commonly used materials fort he production of these materials is anodic aluminium oxide (AAO). The porous structure of AAO is based on the deposition of inorganic, organic or composite materials in these pores (Zaraska et al., 2013). Over the past years, various, complex and expensive methods such as photolithography, scanned beam lithography, molding, embossing and imprinting have been developed for the production of these materials. Since electrochemical techniques are simple and inexpensive, AAO's

prepared by electrochemical method play a major role in the developing field of nanotechnology. It is widely used in the production of nanomaterials due to its optical and electrical properties, ease of production and large surface area. Due to all these features, AAO is an excellent structure for nanotechnological applications. It is used in chemical-biological sensors, desalination, energy generation ve storage devices, photonic crystals and corrosion resistant materials (Liu et al., 2021). AAO films are formed with two different morphologies, depending on the electrolyte; barrier-type or porous-type oxide films. Properties such as hardness, corrosion and creep resistence can be obtained by anodizing aluminum in acidic electrolytes, and the high porosity that occurs when anodized adds good adhesion properties to the material, making it useful for electroplating, painting and coloring (Lee & Park, 2014). (Masuda et al., 1996) proposed a two-step anodization method to obtain AAO. One-step anodization causes the formation of a more irregular oxide layer than two-step anodization, and then this oxide layer is removed by a chemically and anodized again to obtain a more regular pore structure (Ateş et al., 2018). (Zaraska et al., 2016) reported that two-step anodization is the best way to achieve the hexagonal pore pattern. Nanoporous AAO can be produced using acidic electrolytes such as sulfuric, oxalic, phosphoric and chromic acid. In addition, AAO can be produced in a barrier-type structure as opposed to a porous structure by using basic electrolytes (C. Cheng & Ngan, 2015). Boric acid or another organic acid salts can be used in the production of barrier-type AAO (Eessaa & El-Shawy, 2023). It has been found that properties such as pore diameter and interpore distance of AAO depend on parameters such as the electrolyte used, applied voltage, temperature and anodizing time (Zaraska et al., 2013). It is also known that porosity, pore density, barrier layer thickness and wall thickness depend on these parameters (Zaraska et al., 2016).

In this research, anodization process was applied to two groups of aluminum at different voltages (20-60 V) and at constant 30 V for different times (30-120 min) at room temperature for 60 min each samples. The anodization process was carried out at room temperature. Oxalic acid was chosen as the electrolyte solution. The nanopore structure, surface roughness and topography, photocatalytic, crystallographic and hydrophilic properties of the formed AAO were examined.

1.2 Application of Anodic Aluminum Oxide

AAO is an electro-synthetic method that modifications the surface of the metallic through oxidation. During this method, a self-coordinated, incredibly demanded cluster of spherical and hole shaped pores can be made with controllable pore widths, periodicity, and thickness. These properties have interaction AAO layers for use as formats in numerous nanotechnology applications without the need for highly priced lithographical systems (Manzoor et al., 2023).

Moreover, AAO membranes have been widely used as templates for synthesizing high aspect ratio nanostructures. These nanostructures are typically grown through electrochemical methods or pore-wetting processes, showcasing the versatility of AAO in nanotechnology applications (Bridges et al., 2013). The fabrication of nanodots, nanorods, nanowires, nanotubes, and nanocomposite materials has been facilitated by AAO templates, demonstrating its significance in material science (Ying et al., 2019). Additionally, AAO has been explored for its potential in enhancing the electrical and mechanical properties of aluminum alloys, showcasing its utility in engineering applications (T. C. Cheng & Chou, 2015).

Popat et al (2007) examined the effect of stomal cells in the bone marrow of mice on cell adhesion, proliferation and viability by placing them in a nanoporous alumina produced by a two-step anodization process. Its benefits on biocompatibility and bone cell growth were stated. In conclusion, AAO has shown potential for use as a coating material for orthopedic implants. Morel X (1998) placed a porous alumina ball as an implant into the eye sockets of rabbits and achieved promising results in anophthalmic sockets for humans due to tissue tolerance and rapid fibrovascular growth.

Flamme et al (2005) used nanopore AAO membranes to encapsulate therapeutic cells as a treatment for diabetes. They placed the AAO membrane produced by two-step anodization on a polymer layer. The diffusion behavior of glucose, IgG and insulin was examined, the function of the encapsulated MIN6 cells were tested, and living cells were imaged under a confocal microscope. The data showed that the device transported molecules such as glucose and insulin. It was also observed that the

encapsulated cells were able to respond to glucose entry signals. This method has shown to provide an alternative encapsulation strategy for the treatment of diabetes.

Nanotextured polymer surfaces were created using a nano-imprint process to study their anti-cell adhesion properties. NIH 3T3 fibroblast cells were cultured on these surfaces to evaluate the results. A flexible, rubber-like silicon polymer known as polydimethylsiloxane (PDMS) (provided by Dow Corning, Co.) was chosen as the imprinting stamp. The flexibility of the PDMS stamp allowed for conformal contact with curved surfaces. This nanotextured PDMS stamp was initially replicated from a nanoporous alumina mold and subsequently used to fabricate nanotextures on a biocompatible polymer through the nano-imprinting process. In conclusion, the surface nanotexturing technique provides lasting anti-cell adhesion properties without the need for chemical treatments. Han et al's study serves as a preliminary validation of cell behavior, highlighting that issues like platelet adhesion before cell adhesion need to be addressed before conducting in-vivo tests (E. D. Han et al., 2017).

Current techniques for sternum replacement involve the use of metallic prostheses. However, this method has various drawbacks. (Bertin et al., 2018) have developed a porous alumina ceramic sternum, which exhibits biocompatibility, bacterial resistance, and compatibility with radiotherapy, and investigated its use for sternum replacement. The surgeries were performed in France. No complications occurred in the patients, and healing was successful.

CHAPTER TWO
THEORETICAL BACKGROUND

2.1 Anodic Aluminium Oxide

Recently, anodization of aluminum has become one of the most important and widespread methods used fort he synthesis of ordered nanostructures of great commercial importance. This method is used to create ordered nanostructure consisting of tightly packed cells containing nanopores in a hexagonal arrangement. Additionally, various applications of aluminum have attracted great attention in the last decades. Some of these applications are the production of dielectric films for electrical capacitors, increasing the oxidation resistance of materials, creating decorative layers with the use of organic or metallic pigments and increasing wear resistance. These developments have increased the scientific and technological importance of anodic aluminum oxide and aluminum (Eftekhari, 2008). The porous AAO film formed on aluminum consists of a thin barrier oxide layer and a relatively thick porous oxide film with nanoporous (Lee & Park, 2014). The formation of pores occurs vertically on the material surface, and the properties of this structure are highly dependent on the experimental conditions and parameters. Specific features of AAO include pore diameter, pore density, porosity, pore length and interpore distance (Manzoor et al., 2023). Anodization is an electrochemical process that results in the formation of an oxide film on the metal. The existing oxide structure on the material surface affects the new oxide layer formed by anodization. The metal undergoes oxidation in a high-voltage electrolyte and a compact film layer is formed in the early stage of anodization (Fadillah et al., 2021). Figure 2.1 shows the formation of the oxide layer and the oxidation process.

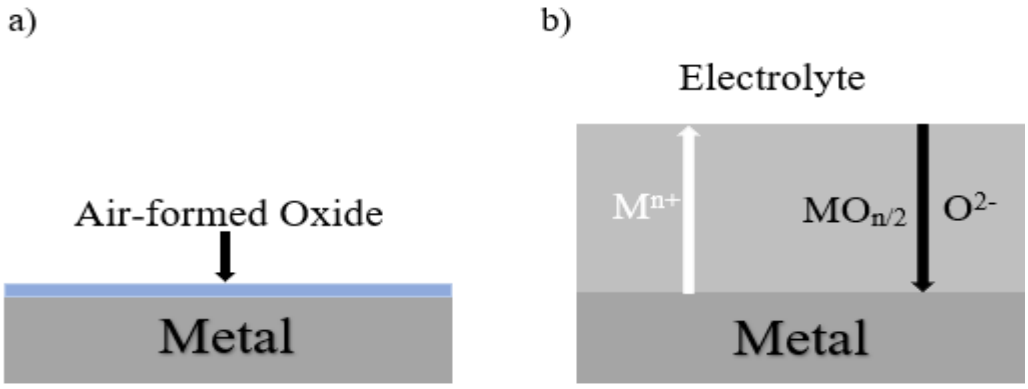


Figure 2.1 Schematic diagram of (a) self-formed oxide layer and (b) the oxidation of anodizing processes.

The $MO_{n/2}$ layer was formed at the metal/film interface by the migration of oxide ions towards the oxide film and the chemical reaction is given in Eq.1.

$$M + nO_2 \longrightarrow MO_{n/2} + 2ne^-$$

The migration of cations that react with water in the electrolyte is given in Eq.2.

$$M^{n+} + n/2\ H_2O \dashrightarrow MO_{n/2} + nH^+$$

The properties of the metal oxide depend on the anodized metal, and if the MO dissolves easily, the metal cannot be protected and will deteriorate. However, if the MO does not dissolve, a barrier layer that protects the metal is formed (Fadillah et al., 2021). Aluminum can be used in all a variety of applications where the metal needs to be protected. The anodization process was used industrially in the 1920s. The application area has expanded by researching and developing this method. Many surface parameters can be controlled. For example, the pore diameter can be adjusted up to 5 nm to 10 micrometers (Poinern et al., 2010). Anodization is an electrochemical process used to oxidize aluminum and its alloys. In a two-electrode cell shown in Figure 2.2, Aluminum serves as the anode and stainless steel or platinum serves as the cathode (Kavas, 2011).

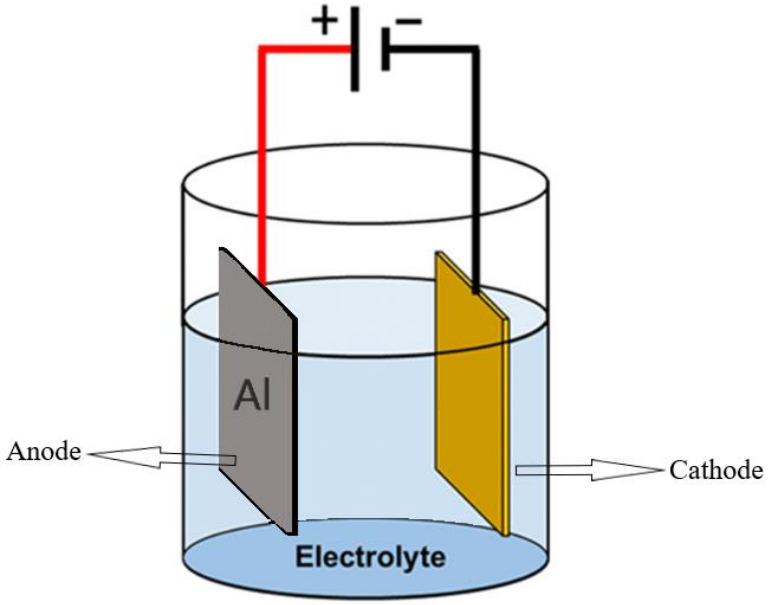


Figure 2.2 Schematic diagram of the annotation mechanism.

When a current of sufficient voltage passes through the electrolyte, an artificial oxide film forms on the aluminum. In aluminum anodization, Al^{+3} cations and O^{-2} or OH^{-} anions are mobile ion species. While Al^{+3} cations are formed at the aluminum/oxide interface O^{2-} or OH^{-} anions are formed at the oxide/electrolyte solution interface. Under high electric current, ion migration occurs, which enlarges the anodic oxide film (Martínez-Viademonte et al., 2020). These anion migrate towards the positively charged anodic layer. Al^{+3} and O^{2-} react with each other, leading to the formation of Al_2O_3 on the metal surface. Since not all Al^{+3} ions react by this interface, Al^{+3} cations can reach the oxide/electrolyte interface from the anode and react with the O^{2-} present there to form additional Al_2O_3 (Abrahami, 2016). As a result, the film morphology will depend on these chemical reactions, that is, the balance between oxide growth and oxide dissolution. The formation mechanism of the anodic film is shown Figure 2.3.

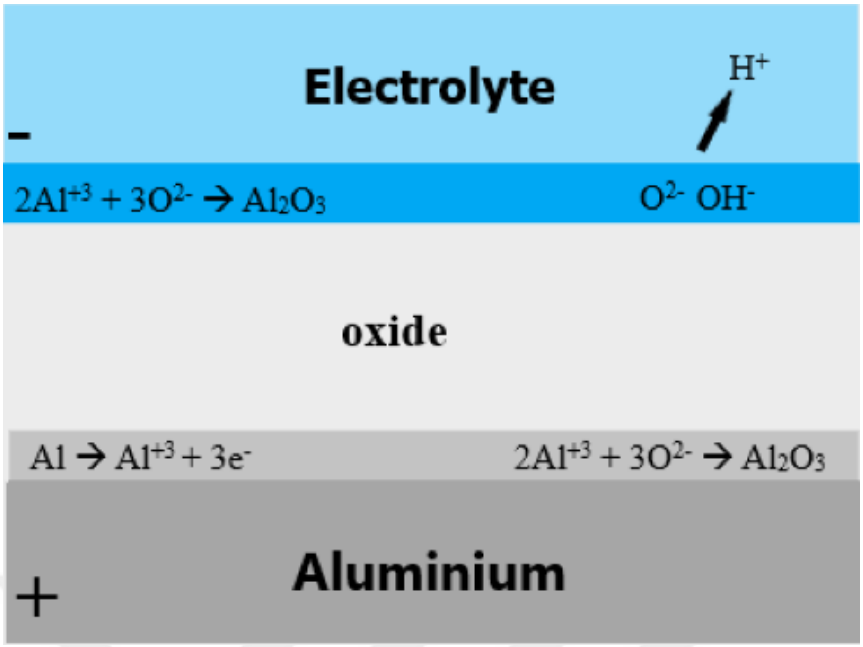


Figure 2.3 The formation mechanism of the anodic film (Eftekhari, 2008).

The substrate we will anodize undergoes an oxidation reaction to form Al_2O_3, and this event can be briefly summarized in 5 steps.

Anodized aluminum forms aluminum ions as a result of the potential given to the system, and these ions move to the oxide layer thanks to the electric field.

$$Al \rightarrow Al^{+3} + 3e^- \quad (1)$$

The water molecules in the electrolyte also dissociate into oxygen and hydroxide ions.

$$H_2O \rightarrow 2H^+ + O^{-2} \quad (2)$$

$$H_2O \rightarrow H + OH^- \quad (3)$$

Hydroxide and oxygen ions formed in (2) and (3) are attracted by the anode and react with aluminum metal to form Al_2O_3.

$$2Al^{+3} + 3O^{2-} \rightarrow Al_2O_3 \quad (4)$$

$$2Al^{+3} + 3OH^- \rightarrow Al_2O_3 + 3H^+ \quad (5)$$

The ions formed in (2) and (3) and the hydrogen ions in the electrolyte dissolve the aluminum oxide into aluminum and water molecules.

$$Al_2O_3 + 6H^+ \rightarrow 2Al^{+3} + 3H_2O \quad (6)$$

Hydrogen ions are affected by the electric field at the cathode and form hydrogen gas.

$$2H^+ + 2e^- \rightarrow H_2 \quad (7)$$

When the reaction rates in steps (6) and (7) reach equilibrium, the dissolution and formation rates become equal (Ku et al., 2023). Thanks to the AAO formed when aluminum is anodized, its volüme increases by more than 30 % (Jessensky et al., 1998).

2.1.1 Types of Anodic Aluminium Oxide

AAO technology is one of the most used technologies in industry and scientific research. It offers self-organization, tunability, good physical and chemical stability compared to other structures (Wei et al., 2019). Due to these features, AAO has become a favorite of research.

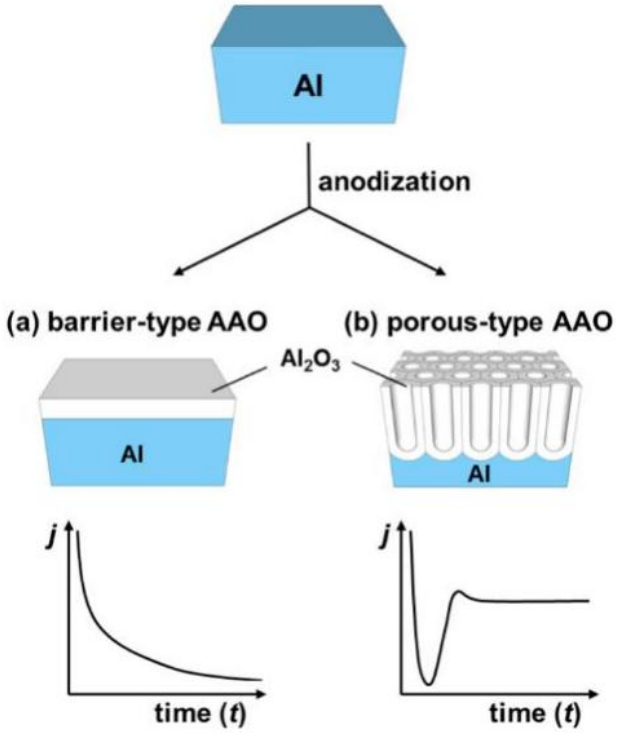


Figure 2.4 Types and current density-time graphs of anodized aluminum (Domagalski et al., 2021).

As seen in Figure 2.4a and 2.4b, AAO is divided into two types; barrier type and porous type, according to its structure. Barrier type AAO has been mostly used in protection and dielectric capacitors. On the other hand, porous type AAO has been used as a template in the synthesis of 1D and 2D dimensional nanostructures in the production of nanowires (Ku et al., 2023). Electrolyte concentration is the most important factor in the formation of these structures. In the formation of a barrier type oxide layer at constant potential, the current decreases over time as seen in Figure 2.4a. This decrease in current flow affects the oxide layer that the electrolyte can penetrate and the thickness decreases. As can be seen in Figure 2.4b, current changes occur during the formation of the nanoporous oxide layer. The decrease in the initial current flow is related to the change in the internal organization of the structure. After this point, the current remains close to constant (Domagalski et al., 2021). As mentioned before, an oxide layer is formed in both cases. However, this is determined by the pH of the electrolyte solution and experimental parameters.

2.1.1.1 Barrier-Type Anodic Aluminum Oxide

Aluminum is a metal that can spontaneously reacth with air and a barrier oxide layer naturally forms on its surface. Formed barrier oxide layer acts as a protective layer to prevent aluminum from chemicals, further oxidation and makes it mechanically strong and resistant to corrosion.

Table 2.1 Bases used as electrolytes in the production of barrier-type AAO.

Base	Concentration	References
Ammonium Adipate	% 15	Li, X., Du, X., Huang, S., & Xiong, L. (2021)
Boric Acid	2.2 M	(H. Uchi, 2000)
	0.3 M	(Quebbou et al., 2020)
Sodium Metaborate	0.3 M	(Iwai & Kikuchi, 2021)
Sodium Tetraborate	0.05-0.5 M	(Kikuchi et al., 2019)

In barrier type anodization, the oxide layer grows at both the Al/oxide interface and the oxide/electrolyte interface. As shown in Figure 2.3, it was determined that 60% of the oxide was formed at the Al/oxide interface and 40% of the film thickness was formed at the oxide/electrolyte interface. Film continues to grow until it reaches a level of resistance that blocks the flow of electricity (Martínez-Viademonte et al., 2020). Barrier type AAO films are formed in neutral electrolytes such as borate, oxalate, citrate, phosphate, tungstate and adipate as shown in Table 2.1. The two different types of anodic oxides, barrier and porous, differ from each other in the way oxide formation changes over time. When the barrier type oxide is formed under constant potential, the current density (j) decreases exponentially with time (t). This causes the film growth rate to slow down almost exponentially over time. Restrict the maximum film thickness that can be achieved for barrier type AAO films (Lee & Park, 2014). Since the electrolyte ions are included in the film, the chemical composition of barrier type AAO is not pure alumina. Additionally, barrier films are thin and dielectrically tight (Martínez-Viademonte et al., 2020).

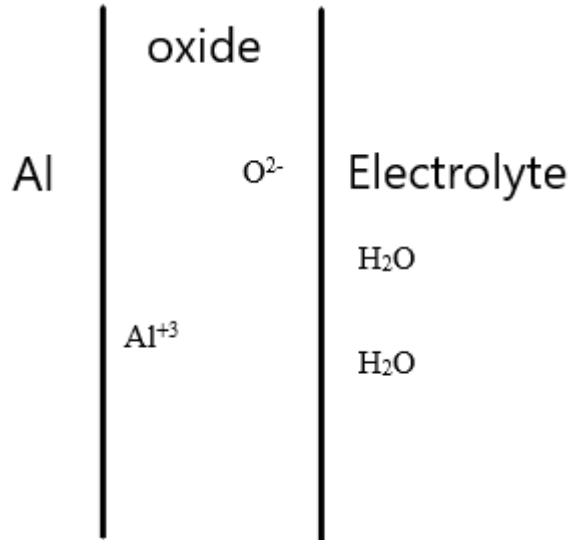


Figure 2.5 Diffusion of aluminum cations through the oxide layer.

Diffusion of oxygen-containing anions (O^{2-}/OH^-) from the electrolyte occurs at the aluminum oxide interface, where they form aluminum oxide. At the same time, aluminum cations (Al^{+3}) diffuse through the oxide layer and accumulate at the oxide/electrolyte interface as alumina. (Kavas, 2011). Figure 2.5 depicts this diffusion.

2.1.1.2 Porous-Type Anodic Aluminum Oxide

Porous AAO film is shown schematically in Figure 2.6. Porous AAO has a honeycomb-like structure and is formed in large numbers in parallel with each other on the aluminum surface. Each nanopore is surrounded by a thin barrier layer at the metal/oxide interface.

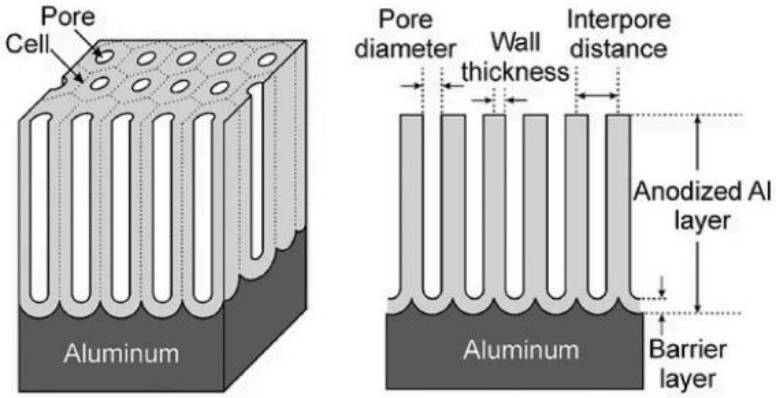


Figure 2.6 Parameters of porous-type anodization (Martínez-Viademonte et al., 2020).

In a proper anodizing system, oxide cells spontaneously form in a certain order in hexagonal geometry. In addition, if the resulting porous structure is removed from the aluminum surface, the surface will be concave. The thickness of the porous layer is directly proportional to the total charge generated in electrochemical reaction. Additionally, the depth of the pores is related to the anodization time. In general, porous AAO structure has important and various structural parameters such as pore diameter (D_p), interpore distance (D_c), barrier layer thickness (B), wall thickness (W), pore density and porosity (Lee & Park, 2014). The parameters of the structure are highly dependent on the anodizing process. Pore diameter, interpore distance, porosity and pore density are the most significant parameters.

Table 2.2 Acids used as electrolytes in the production of porous-type AAO.

Acid	Concentration	References
Oxalic acid	0.3 M	(Sulka & Stepniowski, 2009) (Leontiev et al., 2019) (Li et al., 2016) (Shamsuddin et al., 2021)
	%10	(Choudhary et al., 2017)
Sulfuric acid	0.05-0.2 M	(Pashchanka & Schneider, 2016)
	0.3 M	(Masuda, 1997), (Schwirn et al., 2008)
Phosphoric acid	0.3 M	(Iwai, M., & Kikuchi, T. (2023)
Citric acid	2 M	(Ono et al., 2004)
Malonic Acid	2-5 M	(Ono et al., 2005)

Nanoporous AAO structures are obtained in a more acidic environment compared to barrier-type AAO to increase the solubility of the anodic oxide barrier layer. Table 2.2 shows several acids used in the production of porous AAO structures. Throughout the process, the thickness of the barrier layer remains constant due to a balance between the forming oxide and the dissolving oxide. The structural properties of the resulting porous AAO depend on parameters such as temperature, electrolyte concentration, and applied voltage, similar to barrier-type AAO. However, since porous AAO has variable properties such as pore diameter and pore spacing, these parameters are of greater importance compared to barrier-type AAO (Ruiz-Clavijo et al., 2021). The studies presented in Table 2.2 indicate that increasing the applied voltage results in larger pore diameters and greater distances between pores. A review of the literature shows that oxalic, sulfuric, and phosphoric acids are the most

frequently used, each requiring specific parameters such as temperature, voltage, and anodization time. Besides these common acid solutions, selenic, arsenic, malonic, tartaric, and phosphonic acids, each yielding unique results under specific conditions, have also been utilized. When a constant current is applied to the porous AAO film, the cell voltage initially rises, then gradually decreases, and eventually stabilizes (Kavas, 2011).

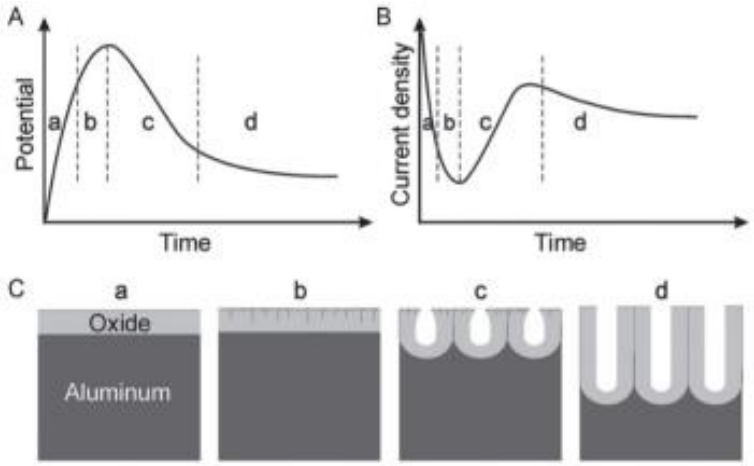


Figure 2.7 Schematic illustration of the kinetics of porous AAO growth in galvanostic (A) and potentiostatic (B) regimes, with stages of anodic porous oxide development (C) (Eftekhari, 2008).

Figure 2.7 shows graphs of voltage and current density over time, along with the stages of oxide film formation. Both the potential and current density graphs, which consist of four stages, exhibit the same characteristic behavior. During constant voltage, the current initially transitions from a high value to a low value and then stabilizes. In stage A, a homogeneous barrier film forms. Some penetration paths develop at the oxide/electrolyte interface. In stage B, because the current takes the path of least resistance, it concentrates in thinner oxide regions on the film, reducing the formation rate of voltage on the film. The previously described Al^{+3} ions turn into pores before they can repair these penetration paths, leading to the arrangement of pores in stage C. The formation of the porous structure decreases the barrier layer thickness, resulting in a drop in potential value. In stage D, the current within the curved barrier layer concentrates in each pore, causing the pores to deepen. (Abrahami, 2016).

2.1.2 Hard Anodization

In the early 1920s, the hard anodization process, commonly used in industry, was performed at a high voltage that exceeded the breakdown voltage. This resulted in cracks in the anodized layer, reducing its mechanical strength. Many attempts were made to address this issue. Through these developments, a hard anodization process was created that produced a high-quality nanoporous oxide structure. It is carried out at a high voltage that does not affect the metal, which allows the oxide film to grow rapidly (typically 50−100 μm per hour). However, the resulting porous film often has numerous cracks, irregular pores, and unstable structures, making it very difficult to control key characteristics such as pore size and spacing. Consequently, undeveloped hard anodization is not used in the field of nanotechnology (Lee & Park, 2014; Manzoor et al., 2023). Chu (2006) reported that in the anodization process using sulfuric acid, the breakdown potential could be increased up to 70 V. Al^{+3} ions dissolved in the solution play a critical role because they ensure the proper growth of porous AAO at high voltages and additionally prevent the burning of AAO films. Schwirn (2008) carried out hard anodization experiments in sulfuric acid solutions with varying Al^{+3} concentrations, within the 27-80 V range. The findings indicated that the high voltage anodization process is primarily influenced by the initial limiting current density rather than the properties of the solution. In the study by (Lee et al., 2006) it was found that HA has more advantages over MA, and current density is an important parameter for nanopore formation. It was observed that the porosity is lower in HA compared to MA (PHA ~3 % - PMA ~10 %), with an interpore distance of 200-300 nm (MA =~100 nm). Additionally, it was determined that the growth rate of the porous oxide film in HA is 25-35 times faster than that in MA. (Lee et al., 2010) conducted a 20-minute anodization process at 0 degrees Celsius in oxalic acid solution at 140, 160, and 180 V, and observed instantaneous current fluctuations in the results.

2.1.3 Mild Anodization

Masuda and Fukuda observed that the lower portion of porous AAO films produced by aluminum anodization in 0.3 M oxalic acid at 40 V gradually acquired a self-ordered pore structure as initially irregular pores were slowly rearranged. Masuda and

Satoh (1995) developed a two-step anodization method. Generally, the first anodization in the two-step process lasts more than 24 hours. After the first step, the irregular pore structures formed are exposed to a solution known as 80 degrees Celsius 0.5 M H_3PO_4 - 0.2 M CrO_3 PC-etching, which results in the aluminum surface adopting a hemispherical concave shape. The second anodization is carried out under the same conditions as the first anodization. Generally, porous AAOs formed by the two-step MA process exhibit a polydomain structure. In Figure 2.8, the formation scheme of two-step AAO is shown: (i) the first anodization, (ii) the removal of the oxide structure through chemical etching, and (iii) the second anodization.

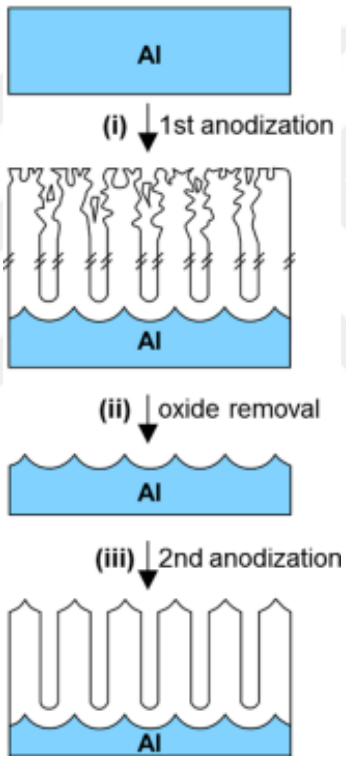


Figure 2.8 A schematic view of two-step mild anodization process for AAO (i) the first anodization step, (ii) removal of disordered porous AAO, and (iii) the second anodization step (Lee, 2010).

After the development of the two-step process based on oxalic acid anodization, researchers not only focused on producing porous AAOs with different pore sizes and densities but also conducted numerous studies, particularly using phosphoric acid and sulfuric acid electrolytes, to understand how pores grow and self-organize during this process. Studies with the mentioned electrolytes have shown that the optimal applied potential values are 25 V for sulfuric acid, 195 V for phosphoric acid, 40 V for oxalic

acid, and 48V for selenic acid. In addition, the interpore distance values were found to be 65 nm, 500 nm, 103 nm, and 112 nm, respectively. Shingubara and colleagues aimed to increase the density of AAO by applying 37 V to an electrolyte containing 0.3 M oxalic and 0.3 M sulfuric acid. Ono and colleagues produced porous AAOs with interpore distances of 300 nm in 5 M 120 V malonic acid, 500 nm in 3 M 195 V tartaric acid, and 600 nm in 2 M 240 V citric acid using the MA process. However, the uniformity of pores with such electrolytes was not as good as those using sulfuric acid, oxalic acid, and phosphoric acid in previous studies, limiting the practicality and application of AAOs in the field of nanotechnology. O'Sullivan and Wood reported an increase in pore diameter of AAOs by a ratio of 1.29 V^{-1}, while Zaraska et al (2010) reported an increase by a ratio of 0.9 V^{-1}. On the other hand, Nielsch et al (2002) proposed that regardless of anodization conditions, an increase in interpore distance occurs at a rate of 2.5 V^{-1}, suggesting that approximately 10 % porosity is required for self-ordering of the pores. However, there are many studies with a wide range of porosity values ranging from 0.8 % to 30 % depending on the MA conditions. For example, Nishinaga and his friends (2013) found a pore diameter of 10.4 nm and an interpore distance of 112 nm at 0 degrees Celsius with a 48 V potential applied to selenic acid electrolyte, which corresponds to a porosity value of 0.8 %. However, there are many studies with a wide range of porosity values ranging from 0.8 % to 30 % depending on the MA conditions. For example, they found a pore diameter of 10.4 nm and an interpore distance of 112 nm at 0 degrees Celsius with a 48 V potential applied to selenic acid electrolyte, which corresponds to a porosity value of 0.8 %. The authors reported that the solubility of the acid in the electrolyte solution has a significant impact on the pore diameter and interpore distance, reaching a pore diameter of 10 nm due to the low solubility of selenic acid. (Chen et al., 2008) demonstrated that the addition of polyethylene glycol (PEG) to the electrolyte reduces the pore diameter, while it has no effect on the interpore distance and barrier layer thickness. Similarly, Martín and his colleagues (2013) demonstrated that organic additives reduce the pore diameter. Martin and colleagues achieved a pore diameter of less than 15 nm using a solution containing sulfuric acid and ethylene glycol (EG).

2.1.4 Pulse Anodization

The technique of pulsed anodization emerged in the early 1960s (Miller, A.M. 1960). Pulsed anodization utilizes alternating low and high voltage pulses to achieve properties of both hard and mild anodization processes on the aluminum surface (Manzoor et al., 2023). Tu, G. and Huang, L.Y. (1987) examined both pulse AC and DC anodization techniques, finding them to offer satisfactory corrosion resistance but to display cracks and high surface roughness. Lee et al (2006) achieved the production of anodic aluminum oxide (AAO) films with varying pore diameters at the nano scale along the pore axes by merging MA and HA anodization techniques. While this method is favored in the aluminum industry for generating high-quality anodic films, its tendency to create irregular pore structures on anodic aluminum has kept it outside of academic research for four decades.

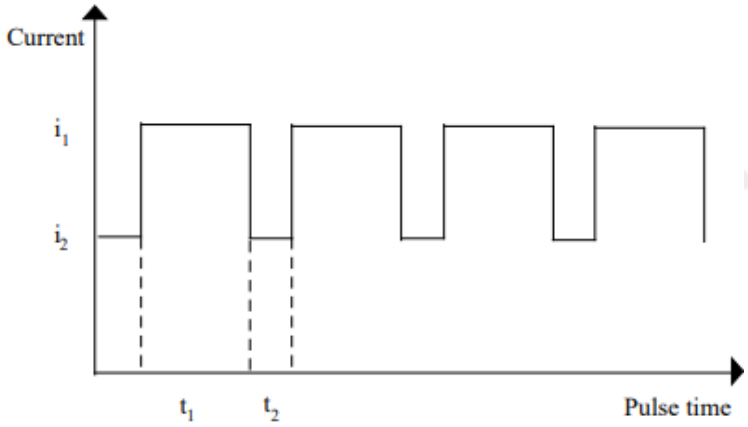


Figure 2.9 A schematic diagram of current – time for pulse anodization (Deacon Juhl, 2004).

Utilizing variable current instead of a constant current value allows for the selection of optimized current values for each process. A schematic diagram of current-time for pulse anodization is seen in Figure 2.9. According to Yokoyama et al in 1982, it's possible to improve materials' resistance to wear and corrosion by inducing oscillations between high and low voltage/current ranges. Additionally, scientific evidence supports the notion that this method enhances the homogeneity of coating thickness and reduces production time. Moreover, for the production of hard coatings, it's viable to increase the low-temperature setting and elevate the maximum achievable coating thickness. (Deacon Juhl, 2004).

2.1.5 Cyclic Anodization

This method, which divides the anodization process into different stages using a periodically changing electrical signal, allows for the formation of a porous structure. As voltage is applied during the process of anodization, pores begin to form within the material. Over time, both the quantity and size of these pores increase, eventually assuming a pear-drop shape under high levels of voltage.

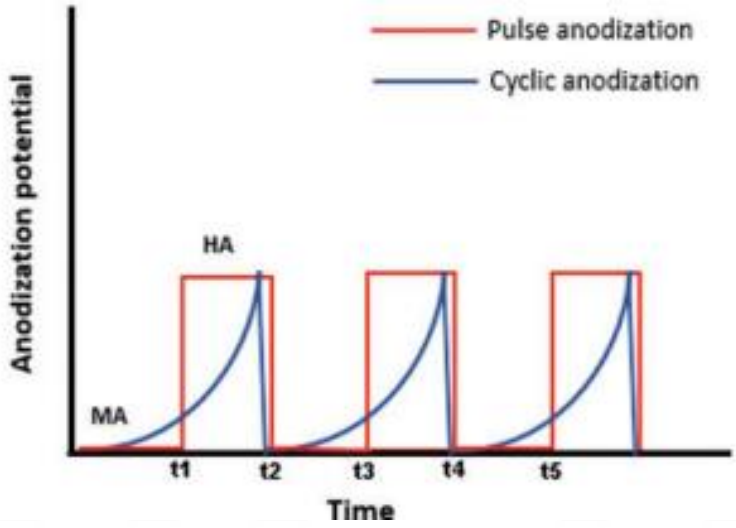


Figure 2.10 A diagram of potential – time for cyclic anodization (Manzoor et al., 2023).

In hard anodization, thin and dense pores are formed, while in soft anodization, larger pores are created. In cyclic and pulsed anodization, as shown in Figure 2.10, the pore length varies depending on the alternating HA and MA processes applied. (Manzoor et al., 2023).

2.2 Structure of Porous Anodic Aluminum Oxide

Figure 2.11 illustrates schematically an ideal porous AAO structure alongside its SEM image. The porous AAO structure resembles a honeycomb-like structure. These numerous adjacent pores form on the surface of the aluminum substrate, and these pores surrounded by the oxide layer are aligned perpendicularly to the substrate. Under appropriate anodization conditions, the oxide cells form in a hexagonal structure.

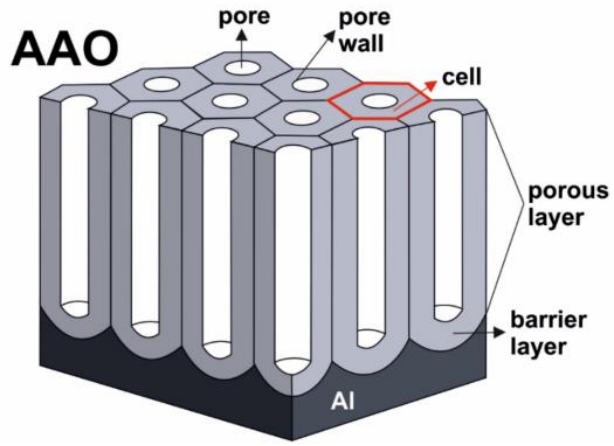


Figure 2.11 Ideally structure of AAO (Brudzisz et al., 2021).

The thickness of the porous AAO layer is directly related to the total charge employed during electrochemical oxidation. Consequently, adjusting the duration of anodization allows for the attainment of oxide nanopore depths ranging from 10 nm to 100 micrometers. Porous AAOs typically exhibit various structural parameters, including interpore distance (D_c), pore diameter (D_p), barrier layer thickness (B), pore wall thickness (W), pore density (n), and porosity (α). The formulas for their theoretical calculation are provided below:

$$Dc = \lambda_C \cdot U \tag{2.1}$$

$$D_p = \lambda_p \cdot U \tag{2.2}$$

It is widely accepted that there is an approximate linear dependence between the anodization potential pore diameter and interpore distance with a proportionally constant of about 0.9 (Zaraska et al., 2010) and 2.5 V^{-1} (Nielsch et al., 2002) respectively. Some sources also consider the pore diameter constant value to be 1.29. D_p is a pore diameter (nm), D_c is a interpore distance and U denotes an anodizing potential (V).

$$n = \frac{2.10^{14}}{\sqrt{3} \cdot D_c^2} \tag{2.3}$$

$$\alpha = 10^{-14} \cdot n \cdot \pi \cdot \left(\frac{Dp}{2}\right)^2 \quad 2.4$$

These structural parameters are significantly influenced by anodization conditions, including factors such as anodizing potential, current density, temperature, anodizing duration, and the type and concentration of electrolyte (Lee & Park, 2014). Porosity (α) and pore density (n), among other significant parameters, can be varied between 5 and 50 % and 10^9 – 10^{11}/cm^2, respectively (Sammi et al., 2020). The development of the oxide layer occurs at the interface between the metal and the oxide in the lower part of the metal. During this process, a naturally formed oxide film is first transformed into a barrier film, then into a porous oxide layer. As the porous oxide layer grows, the barrier layer at the bottom of the pores begins to dissolve under the influence of the electric field. Meanwhile, a new barrier layer forms at the interface between the metal and the oxide. This process repeats continuously, thickening the oxide layer. (Eftekhari, 2008).

2.2.1 Pore Diameter (Dp)

In the obtained porous structure, the pore diameter is directly proportional to the anodization potential. This proportionality constant (λp) is found in the literature at two different values. O'Sullivan et al. (1970) used approximately 1.29 nm/V, while Zaraska et al. (2010) used a value of 0.9 nm/V.

$$D_p = \lambda_p \cdot U \quad 2.2$$

Dp represents the pore diameter, while U abbreviates the applied potential to the electrolyte. The dependence of pore diameter on the anodizing voltage does not significantly differ based on the electrolyte used. In other words, regardless of the electrolyte employed, pore diameter will increase similarly with voltage. In the porous AAO structure, the pores closer to the film surface have larger diameters. This phenomenon can be attributed to two reasons:

Firstly, during the initial stages of the anodization process, irregular growth occurs, resulting in the formation of larger pores. Secondly, through a process known as 'Reorganization' as the anodization process progresses, the pores organize themselves into a more uniform structure. Nevertheless, they remain larger than the pores deeper inside. Other studies have reported that pore diameter is dependent on the anodization potential and current density Beck et al (1958) and O'sullivan et al (1970) illustrates another formula for calculating pore diameter as follows:

$$Dp = D_C - 2 \cdot W \tag{2.5}$$

D_c represents the interpore distance, while W represents the wall thickness (nm). (Palibroda, 1984), investigated how the pore diameter is related to the voltage used during the anodizing process and reported their findings

$$D_p = 4.986 + 0.709U = 3.64 + 18.89 \cdot \frac{U}{U_{max}} \tag{2.6}$$

The critical potential value (U_{max}) is the maximum voltage value that can be safely used on aluminum during the anodization process without excessive gas formation. This value is determined through experiments. (Nielsch et al., 2002), has developed an equation to calculate the diameter of the pores formed on aluminum through anodization:

$$D_P = \sqrt{\frac{2\sqrt{3} \cdot P}{\pi}} k \cdot U \tag{2.7}$$

where P is porosity (P = 0.1 = %10) and k is the proportionality consant (k = 2.5). Based on this equation, the pore diameter is influenced by porosity, the proportionality constant, and the anodization voltage. Researchers have also noted that agitation of the electrolyte during anodization results in heightened local temperatures within the inner oxide layer and an upsurge in current density. This escalated temperature expedites the chemical dissolution of the oxide and facilitates the rapid formation of a new anodic oxide layer. In their study, using sulfuric acid, (Sulka & Parkoła, 2007) demonstrated that electrolyte temperature also influences the pore diameter.

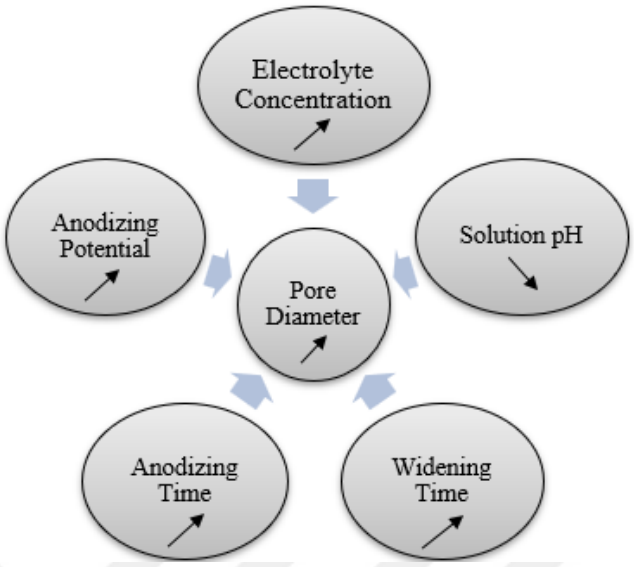


Figure 2.12 Parameters influence on the pore diameter of AAO

The impact of anodization parameters on pore diameter is summarized in Figure 2.12. The ultimate size of pores in the nanostructure formed on aluminum during the anodization process is determined by various factors. Different researchers have observed significant variations in pore diameter even when employing similar anodization conditions and electrolytes. This variation could be attributed to the type of electrolytes used, the duration of anodization, and the applied voltage.

2.2.2 Interpore Distance (Dc)

In AAO, the interpore distance is directly proportional to the anodization voltage used. This proportionality constant is around 2.5 nm V^{-1}. Thus, as the anodization voltage increases, the interpore distance also increases. (Nielsch et al., 2002):

$$Dc = \lambda_C \cdot U \qquad 2.1$$

According to (Keller et al., 1953), the interpore distance can be calculated using the following formula:

$$Dc = 2 \cdot W + Dp = 2 \cdot W_u \cdot U + Dp \quad (2.8)$$

It is generally assumed that the interpore distance in AAO increases linearly with the anodization potential. This assumption is based on the idea that the pore diameter is not influenced by the anodization voltage. Ebihara and colleagues calculated the interpore distance in their studies for oxalic and sulfuric acid using the formulas below:

$$Dc = 12.1 + 1.99U \ (U = 3 - 18V) \quad (2.9)$$

$$Dc = 14.5 + 2.00U (U \leq 20V) \quad (2.10)$$

$$Dc = -1.70 + 2.81U (U \geq 20V) \quad (2.11)$$

The interpore distance for anodization using oxalic acid electrolyte in the range of 20 to 60 V can be expressed as follows:

$$Dc = -5.2 + 2.75U \quad (2.12)$$

The temperature during the anodization process might have a minor influence on the interpore distance. Nevertheless, the overall distribution of pores remains largely unaffected by the process temperature. At the highest temperature examined during anodization, which was 10 °C, there was an approximate 8-10 % increase in interpore distance compared to the distance observed at 1 or -8 °C. Under constant electrical current during anodizing with phosphoric acid, a rise in both the anodizing temperature and the electrolyte strength causes the spacing between pores in nanostructures to shrink (O'sullivan et al., 1970). According to (Marchal & Demé, 2003), the interpore distance in the triangular structure with a hexagonal arrangement of nanopores can be calculated using the following formula:

$$Dc = \frac{4\pi}{\sqrt{3} \cdot Q_{10}} \quad (2.13)$$

where Q_{10} is the position of the first Bragg reflection of the hexagonal arrangement of nanopores.

2.2.3 Barrier Layer Thickness (B)

Aluminum's oxide layer typically acts as a barrier. When oxidation occurs in an acidic environment, this layer turns into a porous structure, and the barrier layer forms at the bottom of the tubes. This layer is thin, dense, and compact, possessing dielectric properties similar to the naturally occurring oxide film in the atmosphere, but it allows current passage due to its structural flaws. The compact barrier layer at the bottoms of the pores makes it difficult for metals to accumulate electrochemically into the pores. Therefore, the thickness of the barrier layer is crucial and affects the future applications of nanostructures obtained through aluminum anodization (Durmuşoğlu E. G., 2012). There is a direct relationship between the anodization potential and the thickness of the barrier layer. Wernick stated that the thickness of the barrier layer in barrier-type coatings is dependent on the anodization potential, and this thickness is approximately 1.3–1.4 nmV^{-1}, while for porous structures, this value is noted as 1.15 nmV^{-1} (Wernick, 1987). Researchers have observed that the thickness of the barrier layer can vary depending on the anodizing potential or the concentration of the electrolyte. Experimental data supports the existence of B_U, also known as the anodizing ratio, which is defined as the ratio between the barrier layer thickness and the anodizing potential.

Table 2.3 Anodizing ratio (B_u) for several anodizing electrolytes (Eftekhari, 2008)

Electrolyte	Current density (mA cm^{-2})	Concentration (M)	B_u (nm V^{-1})
H_3PO_4	100[a]; 80[b]	0.4	0.89[a]; 1.14[b]
	(20-60)[b]	0.42	1.19[b]
	87[b]	1.70; 3.10	0.99; 0.97[b]
$H_2C_2O_4$	(20-60)[b]	0.22	1.18[b]
	3[b]	0.45	1.66[b]
H_2SO_4	15[b]	1.70	1.00
	3[b]	2	1.45[b]
H_2CrO_4	(20-60)[b]	0.26	1.25[b]

When examining the data in Table 2.3, it can be observed that the thickness of the barrier layer per volt varies depending on whether the oxide films are formed at a constant potential or a constant current density. (a) denotes the constant current density anodizing, (b) constant potential anodizing. An increase in anodization temperature reduces the thickness of the barrier layer during anodization at a constant potential. B_u denotes the anodizing ratio for several anodizing electrolytes.

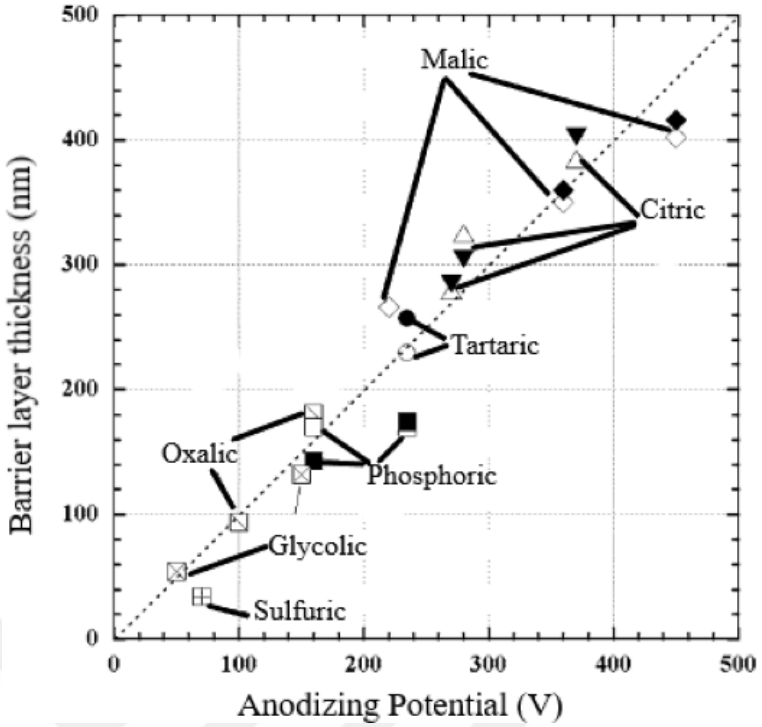


Figure 2.13 Effect of anodizing potential on the barrier layer thickness for AAO in different electrolytes (Eftekhari, 2008)

The thickening of the barrier layer with increasing electrolyte concentration indicates that ionic conduction becomes easier at the specified current density. Therefore, a large portion of the ionic current passes through the microcrystallites in the barrier layer. However, the decrease in the thickness of the barrier layer with increasing electrolyte concentration and anodization temperature is due to the increase in field-assisted dissolution at the oxide/electrolyte interface (Eftekhari, 2008). Chu and colleagues have demonstrated the effect of anodization potential on the barrier layer thickness using various electrolytes, as shown in Figure 2.13 (Chu et al., 2006). Nielsch and his colleagues suggested the following formula regarding the relationship between barrier layer thickness and interpore distance:

$$B \approx \frac{D_C}{2} \qquad 2.14$$

Barrier layer thickness (B) can be calculated using this formula that includes wall thickness value established by Ebihara et al.

$$B = 1.12 \cdot W \qquad 2.15$$

2.2.4 Wall Thickness (W)

Various studies have been conducted to calculate wall thickness. According to Sulka, the calculation of wall thickness is as follows:

$$W = \frac{Dc - Dp}{2} \tag{2.16}$$

O'Sullivan and Wood report that the wall thickness is approximately 71% of the barrier layer thickness. So according to their study, wall thickness can be calculated as follows:

$$W = 0.71 \cdot B \tag{2.17}$$

According to another study, the proportionality between wall thickness and barrier layer thickness in oxalic acid anodization varies slightly with anodization potential ranging from 5 to 40 V (Durmuşoğlu E. G., 2012). In aluminum anodization, a relationship has been observed between the thickness of the oxide layer (wall thickness) obtained and the anodization potential. Between 5 and 20 V potentials, this relationship is approximately linear with a proportionality constant of about 0.66. However, at higher potentials, the proportionality constant gradually increases, reaching up to 0.89 (Eftekhari, 2008).

2.2.5 Porosity

During aluminum anodization, the porosity of the resulting nanostructures can vary widely based on factors such as the rate of oxide growth, the chemical dissolution rate of the oxide in acidic electrolytes, and the specifics of the anodization process (including electrolyte composition, concentration, duration, applied potential, and temperature). Anodization potential and the pH level of the electrolyte solution are particularly influential in determining porosity. Experimental studies have shown that the porosity of anodic porous alumina can range from 8% to 30%, with significant differences observed among various research findings on this topic. In anodization studies conducted using sulfuric acid (Sulka & Parkoła, 2006) and oxalic acid, it has been observed that the porosity decreases exponentially with increasing anodization

potential. While fixed-potential anodization processes are carried out in sulfuric, oxalic, phosphoric, and chromic acids, it has been observed that increasing anodization potential reduces the porosity of nanostructures. Fixed-potential anodization processes are conducted in sulfuric, oxalic, phosphoric, and chromic acids, and it has been observed that increasing anodization potential reduces the porosity of nanostructures (Ono et al., 2004; Ono & Masuko, 2003). Increasing the anodization temperature reduces the porosity of nanostructures formed in oxalic acid (Bocchetta et al., 2002) whereas the opposite effect has been observed in sulfuric acid (Sulka & Parkoła, 2007). Porosity is defined as the ratio of the surface area covered by pores to the total surface area and is characteristic of hexagonal nanostructure porosity:

$$\alpha = \frac{\pi}{2\sqrt{3}}\left(\frac{Dp}{Dc}\right)^2 = 0.907\left(\frac{Dp}{Dc}\right)^2 \quad 2.18$$

Alternatively, according to Ebihara (1983), pore density (1 cm^2) can be calculated as follows:

$$10^{-14} n \cdot \pi \cdot \left(\frac{Dp}{2}\right)^2 \quad 2.19$$

The ideal porosity for the most suitable anodization conditions is determined to be 10 %. These conditions primarily depend on the applied anodization potential. The required potentials to achieve excellent hexagonal ordering in sulfuric, oxalic, and phosphoric acids are 25 V, 40 V, and 195 V, respectively (Eftekhari, 2008).

2.2.6 Pore Density (n)

The microelectronics sector has a keen interest in systematically organized nanomaterials consisting of densely arranged nano-pores or nanotubes. AAO offers optimal packing density due to its hexagonal cell symmetry. Hence, the quantity of pores formed during the anodization process stands out as a critical characteristic of porous alumina. Porosity, denoting the count of pores per unit area within a nanomaterial, is mathematically expressed as follows:

$$n = \frac{10^6}{p_h} = \frac{2 \cdot 10^6}{\sqrt{3} \cdot D_C^2} \qquad 2.20$$

Where Ph is a surface area of a hexagonal cell (Zaraska et al., 2010). According to the formula, an increase in interpore distance would result in a decrease in pore density.

2.3 Parameters Affecting the Anodic Aluminum Oxide Properties

2.3.1 Pre-Texturing

Pre-texturing refers to the process of preparing or treating a surface in a specific manner beforehand. This is often done to achieve a desired pattern or texture on a surface. For instance, the preparatory process involving mechanical or chemical treatments to create a specific pattern on the surface of a material can be termed pre-texturing. This term is commonly used in industrial production and material processing processes. Studies indicate that the pre-texturing stage prepares and primes the surfaces for pore initiation and development. Depending on the growth mechanism, features such as lines, scratches, and geometric surface characteristics enhance curvature, thus providing preferred regions for pore formation and development. (Terryn, 1987) demonstrates that these features facilitate the formation of pores in a regular alignment. For the production of nanostructures, such as in the fabrication of alumina molds, an extremely regular pore arrangement is required. In such cases, a two-step anodization process is employed to achieve a uniform structure, along with intermediate oxide dissolution. During this process, as described earlier, the first step of anodization is created to contour the surface texture. However, due to its time-consuming and costly nature, this method is generally not used in the aerospace industry (Abrahami, 2016).

2.3.2 Incorporation of Anions

Incorporating anions into various materials plays a crucial role in tuning their physical and chemical properties. The incorporation of electrolyte-derived anions into anodic alumina during anodization processes is a well-understood phenomenon, with porous-type anodization showing the greatest incorporation of anions (Lee & Park, 2014). The incorporation of anions into the structure of the anodic oxide layer largely depends on the type of oxide film formed. Figure 2.14 illustrates the most commonly used electrolytes. The anion content of these acids in the oxide layer is presented within.

Electrolyte	H_2CrO_4	H_3PO_4	$H_2C_2O_4$	H_2SO_4
Anion content (%)	0.1–0.3	6–8	2–3	10–13

Figure 2.14 Percentage of incorporated anions in the AAO (Eftekhari, 2008).

This data indicates the typical content of incorporated anions observed for some popular electrolytes. In Figure 2.15, schematic profiles of the anion concentration in the barrier-type oxide layer in commonly used electrolytes, aimed at forming highly regular nanostructures, are depicted.

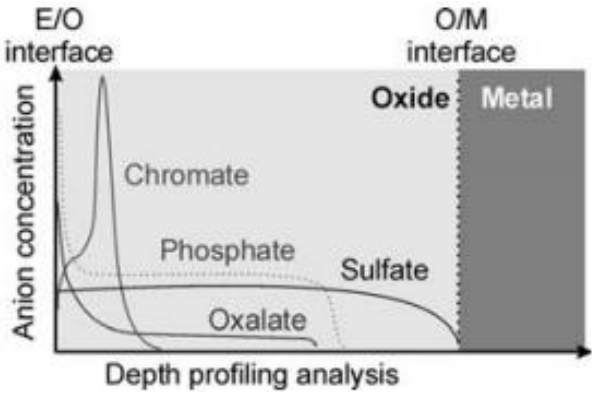


Figure 2.15 Schematic profiles of anion concentration in the barrier-type oxide layer in commonly used electrolytes (Eftekhari, 2008).

In recent years, research has been conducted using various methods such as Auger electron spectroscopy (AES), impedance measurements, Rutherford backscattering

spectroscopy (RBS), secondary ion mass spectroscopy (SIMS), electron probe microanalysis (EPMA), glow discharge optical emission spectroscopy (GDOES), and X-ray photoelectron spectroscopy (XPS) to analyze the depth profiles of barrier-type oxide layers and determine the profiles of the anions contained within. As obtained using the AES method. During the continuous growth of anodic barrier-type films, oxide formation occurs simultaneously at both the electrolyte/oxide and oxide/metal interfaces. This process is associated with the opposite movement of Al^{3+} and O^{2-}/OH^{-} ions. However, some Al^{3+} ions migrate directly into the solution and do not play a role in the formation of the solid oxide film (Thompson, 1997; Xu et al., 1987). For efficient film growth, approximately 40 % of the film material forms on the film surface, while the remainder forms at the oxide/metal interface. Electrolyte anions adsorb at the electrolyte/oxide interface at the bottoms of the pores, and their inclusion in the oxide layer at the pore bottoms occurs as a result of the migration of electrolyte species during porous film growth (Eftekhari, 2008). The electrolyte species can be negative, positive, or neutral: therefore, they may be fixed on the oxide surface or migrate inward and outward at a constant rate. This migration rate varies for different electrolytes. For example, phosphate, sulfate, and oxalate anions migrate inward within the oxide film under the electric field, while chromate anions are characterized by outward migration (Wood et al., 1996). Unlike barrier-type coatings, the growth of porous alumina film occurs only at the oxide/metal interface. Anions migrate to the barrier layer depending on the electric field. The electric field of the porous layer is irregular due to the semispherical shape of the pore base, and the electric field is higher near the electrolyte/oxide interface, closer to the oxide/metal interface at the pore base, and higher than the cell base (Ono & Masuko, 1992). Overall, the incorporation of anions into materials offers a versatile approach to tailor their properties for specific applications. By carefully selecting and incorporating anions with desired characteristics, researchers can fine-tune the physical, chemical, and electrochemical properties of materials, opening up new possibilities for advanced technologies and functional materials.

2.3.3 Temperature

While the temperature parameter may not be very effective for the barrier layer, it is not the case for the porous structure. At high temperatures, local dissolutions occur in the porous structure, leading to an increase in ion transfer and the rate of oxide formation (X. Y. Han & Shen, 2011). In an experiment conducted by Aerts and his friends (2007) using sulfuric acid, they demonstrated that due to the increased rate of oxide dissolution at high temperatures, the porosity value, which was 4% at 5 degrees, increased to 32% when raised to 55 degrees (Aerts et al., 2007). Dissolution effects, while pronounced in the outer layer of the oxide, do not affect the distance between pores, leading to pore enlargement (Abrahami, 2016).

2.3.4 Electrolyte

The physical, chemical, and morphological properties of the porous oxide film are highly dependent on the electrolyte solution used during anodization. The electrolytes used for barrier-type oxide structure and porous oxide structure are provided in Tables 2.1 and 2.2. Acidic electrolytes with low pKa values are used for porous oxide structure.

2.3.4.1 Sulfuric Acid (H_2SO_4)

Gower et al., corrosion prevention and surface enhancement of aluminum and its alloys by anodizing with sulfuric acid (H_2SO_4) have been patented. Sulfuric acid has since then, due to its low cost, extended from laboratory research to industrial applications, becoming the most common electrolyte used to create porous aluminum oxide structures. Sulfuric acid anodization is generally performed at low voltages, typically ranging from 15 to 40 V, compared to the potentials applied to other electrolytes. The pore diameters in the porous oxide film formed in this electrolyte are at their lowest values (Kikuchi et al., 2015). The solution initially contained approximately 25 wt% sulfuric acid based on film properties, but later the acid concentration decreased to 10-20 wt%. In standard anodization processes, a current density of 1-2 A/dm^2 and a voltage between 10 and 22 V are typically used. The

process generally takes place at temperatures between 15-24°C and lasts up to 60 minutes. These conditions depend on the application and desired film properties. Particularly in sulfuric acid anodizing, minor changes such as electrolyte temperature can significantly affect film properties, hence they should be carefully monitored. Using dilute solutions and lower temperatures promotes the formation of harder coatings. In contrast, using more concentrated solutions, higher temperatures, and longer operating times, which enhance the dissolution of the coating in the electrolyte, can result in powdery or spongy coatings that are easily worn off. Table 2.4 shows the areas of application of AAOs made using sulfuric acid, electrolyte concentrations, current density values, applied voltages, and film thicknesses.

Table 2.4 Variation in sulphuric acid anodizing conditions according to product application.

Product	Electrolyte concentration (% by wt of H_2SO_4)	Current density (A/dm^2)	Voltage (V)	Film thickness (microns)
Bright trim	18-24	1.0-1.2	14-15	30-35
Architectural	15-18	1.4-1.8	17-20	40-50
Hard anodizing	15-16	2.0-3.0	25-50	80+

2.3.4.1 Oxalic Acid ($C_2H_2O_4$)

In 1923, Kujirai et al. obtained a patent. Despite initially being developed in Japan, oxalic acid, which has a low dissolution constant, saw wider usage in Germany. More expensive than sulfuric acid, this acid finds extensive industrial applications and is typically operated within the range of 20-65 V (Kikuchi et al., 2015). It forms a harder and more yellowish film compared to coatings created with other electrolytes and can sometimes be mixed with sulfuric acid as well (Kutlu. F., 2014).

2.3.4.2 Phosphoric Acid (H_3PO_4)

Phosphoric acid, as reported by Taylor et al. in 1945, is generally operated at high voltages (60 - 195 V), yielding cell diameters of up to 500 nm. When anodized, the oxide film structure becomes light blue in color due to the formation of widely spaced cells on the substrate surface and is commonly used in nanotechnology (Taylor et al., 1945; Kikuchi et al., 2015). Compared to sulfuric acid and oxalic acid, the cell walls are thinner in this electrolyte, resulting in lower corrosion resistance. It has been observed that the corrosion resistance against moisture is increased due to the phosphate anion formed on the surface.

2.3.4.3 Chromic Acid (C_2CrO_4)

Bengough et al., 1923 yılında kromik asidin patentini almışlardır, ki bu en eski anodizasyon elektrolitlerinden biridir (GD Bengough, 1923). For many years, chromic acid has been used in industrial applications for surface improvement of aluminum and its alloys. Generally operated within the range of 20-50 V, chromic acid has recently fallen out of favor due to the toxicity of hexavalent chromium (Cr^{6+}) when used. Additionally, this electrolyte is not preferred for achieving an ideal hexagonal cell structure (Kikuchi et al., 2015).

2.4 Properties of Anodic Aluminum Oxide Membranes

These structures are highly versatile nanomaterials that artificially combine the fixed and definitively dynamic properties of ceramics. With a homogeneous nanostructure, these structures have adjustable pore spacing and lengths. AAO has a large surface area and can accommodate atoms of different sizes. The extraordinary properties and tunability of the AAO structure make them suitable for numerous applications

The unique properties of AAO membranes make them usable in many fields. Due to the ability to precisely control the pore structures, they provide great advantages in various technical and industrial applications. Thanks to their flexible nanostructures, AAO structures can be effective at both the atomic level and the macroscale.

Combined with the high surface area and ability to accommodate molecules of these membranes, the AAO structure plays an important role in fields such as materials science, biotechnology, and nanotechnology.

As a result, the tunable pore structure and flexible nanostructures of the AAO structure allow it to have a wide range of applications. The properties of these structures are being evaluated in a wide range of areas, from scientific research to industrial applications. The flexibility and high performance offered by AAO membranes also hold great potential for future technological developments. The following are the features that have made these structures so popular (Manzoor et al., 2023).

1) **Electrostatic Properties:** AAO membranes have a structure that can adjust the electrostatic properties of the inner pore surface and the local acidity within the nanochannels. Due to the amorphous structure of the alumina layer during anodization, these membranes create a positive charge on the nanochannel surface. The conditions during the anodization process greatly affect the surface electrostatic properties of AAO membranes, and the acidity of the liquid medium in the pore channels varies depending on the pore diameter. This provides adjustability of the membrane's surface charge and associated electrostatic potentials (Kovaleva et al., 2020).
2) **Wettability:** The wettability of a droplet on a surface depends on the energy difference between the liquid and the surface. In AAO membranes, where the pore diameter increases, the contact angle of water also increases. This energy difference determines whether the liquid can enter the pores or not. Electrochemical anodized aluminum surfaces modified with fluorosilane solutions can form long-term stable AAO membranes with superhydrophobic and corrosion-resistant properties. For membranes prepared by this method, a contact angle of approximately 165° and a sliding angle of <2° have been reported. (Zhang et al., 2015). Besides, also hydrophilic surface can be obtained.
3) **Mechanical Properties:** Nanoindentation technique is used to measure the mechanical properties of AAO membranes. This method analyzes properties such as surface hardness, scratch resistance, and surface roughness. Membrane hardness depends on pore size; hardness decreases with increasing pore size.

Additionally, thermal treatments applied after membrane production can lead to significant changes in mechanical properties, and these treatments increase hardness. Therefore, the performance and applications of AAO membranes can be improved by pore size and applied thermal treatments. It has been reported that the mechanical strength of these membranes can be increased with silicon doping and that they exhibit better performance in biomedical applications (Manzoor et al., 2023).

4) **Biocompatibility:** AAO nanopores exhibit high biocompatibility with four basic tissue type cells, platelets, and various microorganisms. Therefore, AAO has found wide applications in the biomedical field. AAO membranes prepared in barrier type are used in tissue engineering, biosensors, bone implant coatings, and biocapsules for drug delivery. Short-term experiments in living organisms have shown that these applications have positive results in terms of organism compatibility, drug release capability, and mechanical durability (Manzoor et al., 2023).

In conclusion, AAO possesses a unique combination of properties that make it a valuable material for a wide range of applications in nanotechnology, optics, electronics, and other fields. Researchers continue to explore new ways to harness the exceptional properties of AAO for innovative technologies and devices.

CHAPTER THREE
MATERIALS AND METHODS

3.1 Materials

Aluminium 6XXX series rod was obtained from AKG Termoteknik Sistemler San. ve Tic. Ltd. Şti. These Al rods were cut and anodized in oxalic acid solution. Details will be given in the following sections. Acetone and ethanol were used for degreasing. Sodium hydroxide (NaOH), nitric acid (HNO_3) and perchloric acid ($HClO_4$) were used in alkaline etching and electropolishing processes. Chromic acid (H_2CrO_4) and phosphoric acid (H_3PO_4) were used chemical etching.

3.2 Method

Aluminum specimens were cut with STRUERS, LABOTOM-5 and then sanded with 800, 1200 and 1600 sandpaper with PRESI, MECAPOL P230. Aluminum alloys were degreased in acetone and ethanol by using ultrasonic bath for 15 min (BLULAB). For anodization process Before the anodization process alkaline etching and electropolishing were applied to the samples. 1 M NaOH - % 10 wt HNO_3 and $HClO_4$: EtOH (1:4) solutions were used for alkaline etching and electropolishing processes respectively.

Table 3.1 Experimental conditions applied during both anodizing steps for different samples.

<table>
<tr><th colspan="6">Annealed</th><th colspan="3">Not Annealed</th></tr>
<tr><th colspan="3">Group 1</th><th colspan="3">Group 2</th><th colspan="3">Group 3</th></tr>
<tr><th>Name</th><th>Voltage (V)</th><th>Time (min)</th><th>Name</th><th>Voltage (V)</th><th>Time (min)</th><th>Name</th><th>Voltage (V)</th><th>Time (min)</th></tr>
<tr><td>A20</td><td>20</td><td rowspan="5">60</td><td>A30-30</td><td rowspan="4">30</td><td>30</td><td>NA30-30</td><td rowspan="4">30</td><td>30</td></tr>
<tr><td>A30</td><td>30</td><td>A30-60</td><td>60</td><td>NA30-60</td><td>60</td></tr>
<tr><td>A40</td><td>40</td><td>A30-90</td><td>90</td><td>NA30-90</td><td>90</td></tr>
<tr><td>A50</td><td>50</td><td rowspan="2">A30-120</td><td rowspan="2">120</td><td rowspan="2">NA30-120</td><td rowspan="2">120</td></tr>
<tr><td>A60</td><td>60</td></tr>
</table>

For the anodization process, 9 aluminum parts were cut. Five of these were subjected to different voltages for the same duration, while the remaining four were subjected to the same voltage (30 V) but different anodization durations. The first step anodization as well as the second step anodization lasted for 1 hour. Detailed experimental conditions and schematic represantation are given in Table 3.1 and Figure 3.1 respectively. First anodization process for all aluminum samples was conducted at room temperature in 0.3 M oxalic acid electrolyte solution. After the first anodization, a chemical etching process was applied at 60 ^{o}C in a solution containing 6wt% H_3PO_4, 1.8 % H_2CrO_4 for 1 hour. Pt grid was used a cathode and a distance between sample and cathode was about 3 cm. Then second anodization was conducted under the same anodizing process as was used in the first anodization step. After the re-anodization, samples were rinsed with distilled water and dried. Then Group 1 and Group 2 samples were annealed for 3 hours at 450 ^{o}C (PROTHERM). Group 3 samples were not annealed.

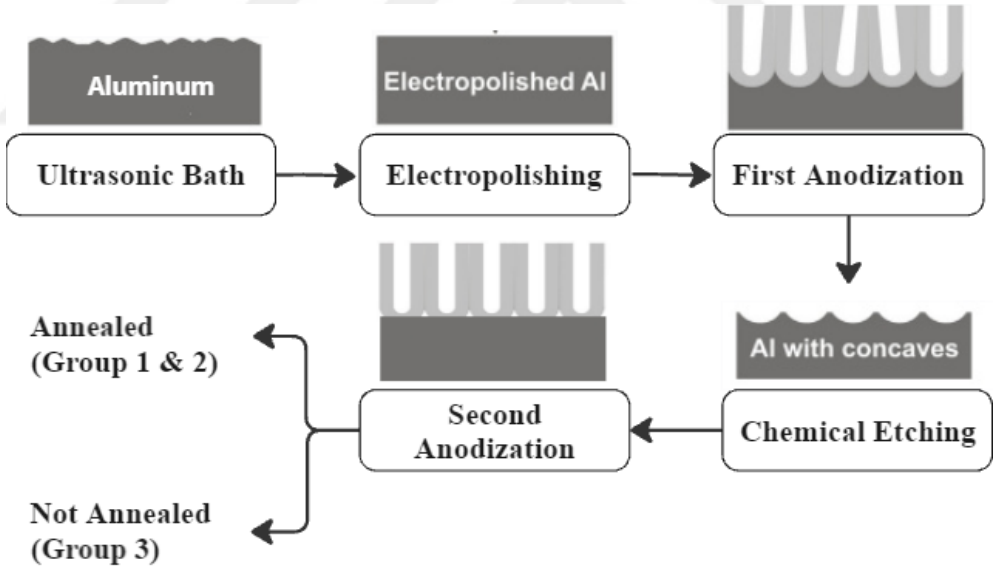


Figure 3.1 Schematic representation of the experiment.

3.2.1 Pore Analysis

The surface of the anodized samples was cleaned with distilled water and dried before being examined under an Scanning electron microscope (SEM) device at a

magnification range of x50k - x350k. The pore diameter and interpore distance values were measured from these images using the ImageJ software. It was observed that in all samples of the groups, in addition to densely packed, round, and irregularly arranged pores, defects were also present. After calculating the pore diameters and interpore distance values using ImageJ, they were also compared with the theoretical formulas shared in the literature in the earlier sections of this thesis. The pore diameter was obtained using formula 2.2 and 2.6, and the interpore distance values were obtained using formula 2.1.

3.2.2 Scanning Electron Microscope (SEM) Analysis

The scanning electron microscope (SEM) is in Figure 3.2 a powerful tool that allows scientists to view materials from a completely new perspective. By using beams of electrons instead of light, this microscope succeeds in creating detailed images of structures that are invisible to the naked eye. The operating principle of SEM is based on the scanning of the sample surface by a focused beam of electrons. These electrons interact with the atoms in the sample, producing signals that contain information about the surface topography and chemical composition. These signals are detected and transferred to a computer. As a result, SEM produces a high-resolution image that represents the material in three dimensions.

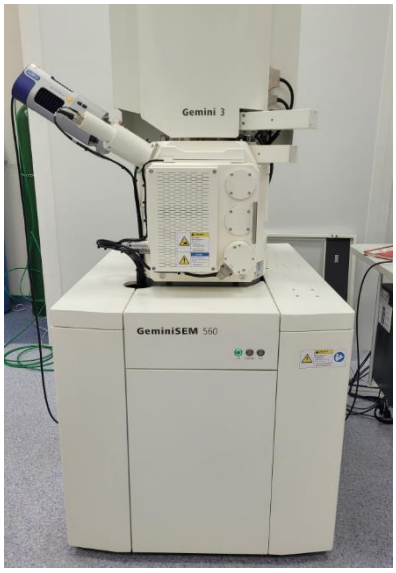


Figure 3.2 Scanning electron microscope (Personal Archive)



Figure 3.3 Sputter coating (Personal Archive)

In this thesis, the surfaces of the samples were imaged using an SEM device. Before imaging, the anodized samples were coated with gold using sputter coater QUORUM SC7620 (Fig. 3.3). Sputter coater device applies ion bombardment to deposit a thin layer of gold onto the sample surface. It is frequently used in electron microscopy, such as in SEM and transmission electron microscope (TEM), to enhance the conductivity of samples. After this process, images were taken at magnifications of x50k, x100k, x200k, and x350k under 3kV. The numerical values of pore diameter and interpore distance were measured from the obtained images using the ImageJ software. 30 values were measured for each feature and averaged. For comparison, an SEM image of the unanodized aluminum sample was also taken.

3.2.3 X-Ray Diffraction (XRD) Analysis

X-ray diffraction (XRD) is a highly effective analytical method used to determine the crystal structure, chemical composition, and various properties of materials. The technique involves directing a beam of X-rays at a crystalline sample and then examining the patterns produced by the interaction of the X-rays with the sample. These patterns provide detailed information about the arrangement of atoms within the

crystal, allowing for precise identification and analysis of the material's structural characteristics.



Figure 3.4 X-ray Diffraction (Personal Archive)

XRD peaks are produced when a monochromatic beam of X-rays is scattered at specific angles by the lattice planes within a specimen. The intensity of these peaks is determined by the positions of atoms within the lattice planes. Consequently, the XRD pattern serves as a fingerprint of the material's periodic atomic structure. The sample diffracts X-rays at angles that follow Bragg`s Law, given by

$$n\lambda = 2\,d\,sin\,\theta \qquad 20$$

where n is an integer, d is the interplanar spacing, and θ is the incident. This law describes the relationship between the wavelength of the X-rays, the spacing between lattice planes in the crystal, and the angle of diffraction. The X-rays are diffracted in specific directions, and an area detector or film captures these reflections as the X-ray source moves in an arc over the sample. The position and intensity of these reflections provide information about the atomic arrangement and spacing within the unit cell of the material (Khan et al., 2020). In this study, the samples were scanned in the range of 3° - 90° at a scan rate of 2°/min by using Thermo Scientific ARL X'TRA (Fig. 3.4).

3.2.4 Atomic Force Microscope (AFM) Analysis

Atomic force microscope (AFM) is an analytical method developed by Binnig in 1986, frequently used in nanostudies to image atomic topography and measure interaction forces (Seo & Jhe, 2008). In the AFM technique, a small and sharp probing tip is scanned while being held over the surface of the sample. The distance between this tip and the surface is so close that atomic-level forces are formed between the tip and the atoms on the surface. The force acting on the probe at the end of the cantilever can be determined by detecting the deflection of the cantilever.

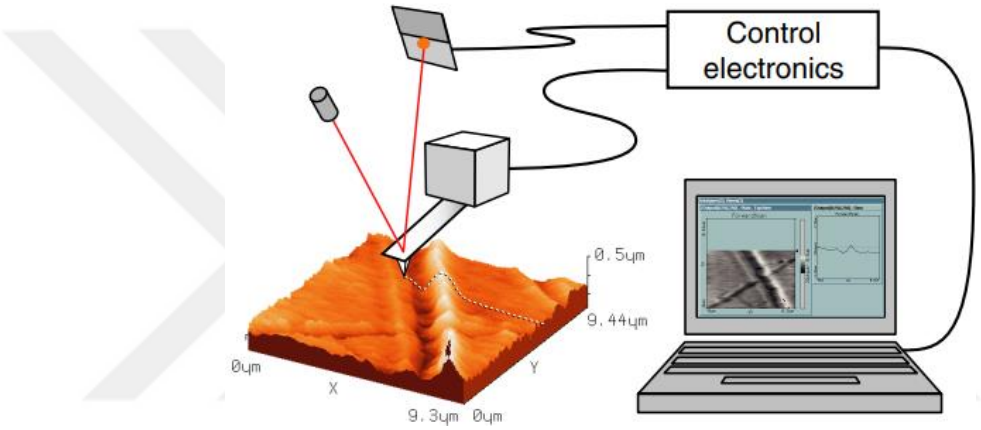


Figure 3.5 The operating principle of atomic force microscopy.

AFM can be used in both static and dynamic operation modes. The AFM cantilever is a microfabricated cantilever with an integrated tip mounted on a cantilever holder chip (Fig. 3.5 and Fig. 3.6). When the sensor tip makes contact with the sample, a repulsive force increases as the tip-sample distance decreases. In the static force mode, the deflection of the cantilever due to the force on its tip is measured using a laser beam deflection system. In dynamic operating modes, the cantilever is stimulated using a piezo element, which oscillates at a fixed amplitude and frequency close to the natural resonance frequency of the cantilever. The repulsive force exerted on the tip alters the resonance characteristics of the cantilever, leading to a reduction in its vibration amplitude. The laser beam deflection system detects these vibrations of the cantilever. In this study, imaging in deflection and z-axis modes was performed on an area of 62.3 x 62.3 micrometers square for Group 1, 2 and 3.

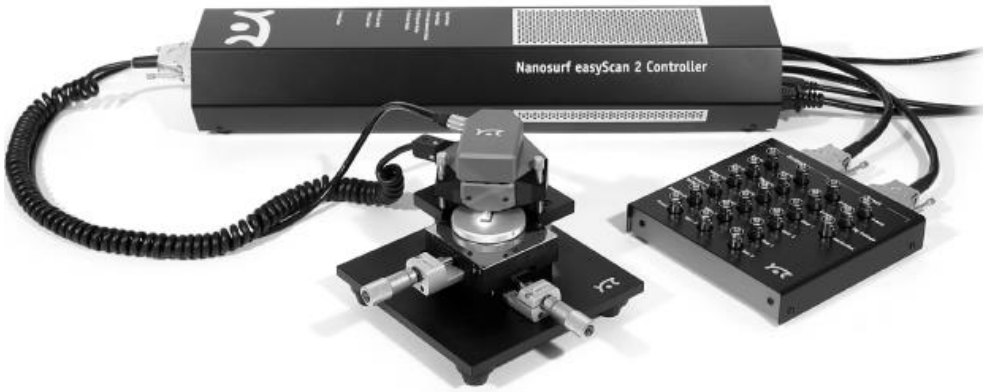


Figure 3.6 Atomic force microscope.

3.2.5 Water Contact Angle (WCA) Analysis

A contact angle indicates how well a liquid spreads over a surface, varying based on the physical properties of the materials. The Figure 3.7 below shows three droplets on a surface: the left-most droplet has a large contact angle and does not spread, while the right-most droplet has a low contact angle and spreads well. This spreading is known as wetting, and a droplet either wets or dewets when placed on a surface.



Figure 3.7 Three types of water droplets.

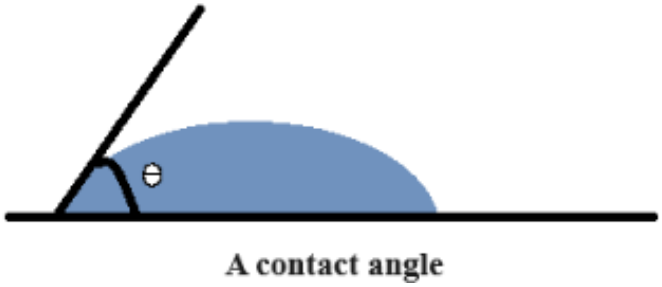


Figure 3.8 A contact angle of a water droplet.

Superhydrophobic surfaces can be obtained by manipulating materials with micro- or nano-corrugations. This phenomenon is called the lotus effect and is named after lotus leaves. When a water droplet is placed on a lotus leaf, it forms a high contact angle with the leaf surface. Superhydrophobicity consists of two states: Cassie-Baxter and Wenzel (Fig. 3.9). In the Cassie-Baxter state, the droplet does not penetrate the surface cavities. In the other state, Wenzel, the liquid is in contact with the entire surface of the solid. In both states, the contact angle is high, but lower angles are achieved in the Cassie-Baxter state (Giacomello et al., 2012). The method for measuring the contact angle of a water droplet placed on a sample is shown in Figure 3.8.

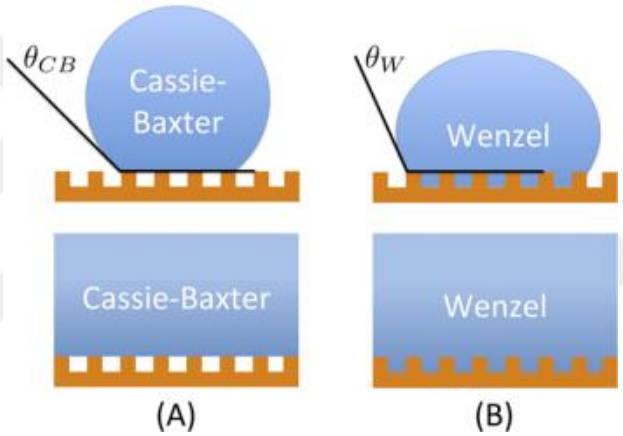


Figure 3.9 Cassie-Baxter and Wenzel states.

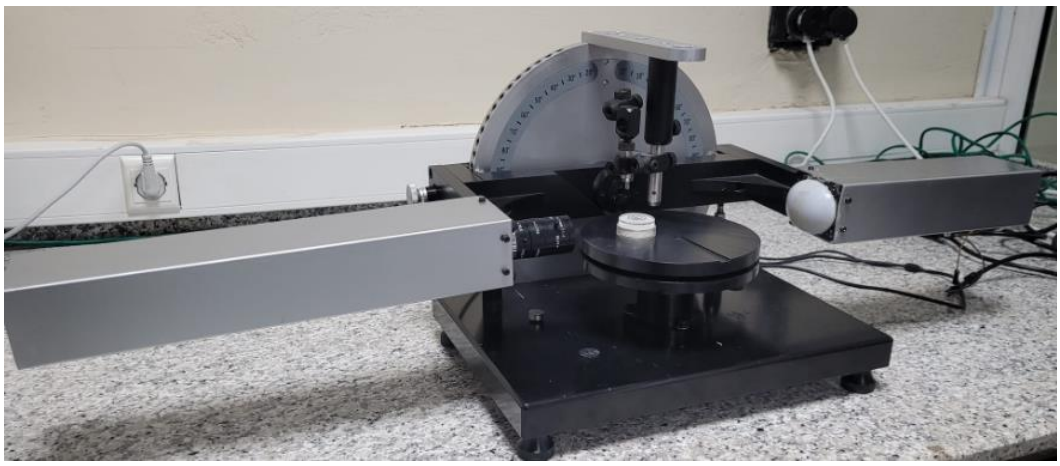


Figure 3.10 Instrument used to measure water contact angle (Personal Archive).

Water contact angle (WCA) was measured with a water droplet by measuring instrument (Figure 3.10) in air at room temperature. As a result of anodization, a WCA test with distilled water was performed on Group 1,2 and 3 to control the hydrophilic properties of the samples.

3.2.6 Surface Roughness Analysis

Surface roughness tests assess the texture and quality of a surface by measuring irregularities and deviations, which can impact the material's performance and appearance. Here are some commonly measured roughness parameters:

- Ra (Average Roughness): The arithmetic average of the absolute values of the surface height deviations.
- Rq (Root Mean Square Roughness): The root mean square average of the surface height deviations. More sensitive to large deviations, providing a more comprehensive measure of surface roughness.
- Rz (Average Maximum Height of the Profile): The average of the heights of the five highest peaks and the depths of the five deepest valleys.
- Ry (Maximum Roughness Depth): The vertical distance between the highest peak and the lowest valley.

A surface roughness test was conducted on Groups 1, 2, and 3. Each sample cleaned to remove any debris or contaminants that affect the measurement. The values of Ra, Rq, Rz, and Ry were measured five times and their averages were calculated.



Figure 3.11 Surface roughness instrument.

Surface roughness tests are critical in various industries, including manufacturing, automotive, aerospace, and medical devices. These tests help improve product quality, performance, and durability by ensuring that surfaces meet required specifications. Figure 3.11 shows a typical surface roughness measurement device.

CHAPTER FOUR
RESULTS & DISCUSSION

4.1 Morphological Analysis

The pore structures formed after the anodization process were examined using an SEM device, and images were taken at magnifications ranging from x50k to x350k for each sample and for comparison purposes, an image of a non-anodized aluminum sample was also taken (Figure 4.1). From the SEM images, it is evident that we have altered and manipulated the surface of the aluminum. As mentioned in the earlier sections of the thesis, the pores formed when we anodized the aluminum are visible in the SEM images. As seen in Table 4.1, 4.2 and 4.3, various parameters were tested. It was observed that as the voltage increased, a more defined porous structure was achieved, the pore diameters increased, and surface defects decreased. Subsequently, SEM images of the AAO samples obtained by applying constant voltage and variable durations were taken. It was found that the duration also affected the pore diameters and pore arrangement. Although sufficient effect was not achieved at the 30-minute anodization duration, visible improvements on the surface were observed at 60, 90, and 120 minutes. Nanopores were observed on all specimens but nano-cavities. It was also observed that thermal treatment had no effect on the pore diameter and interpore distance values. The pore diameter and interpore distance values of the three groups were calculated using ImageJ (Table 4.1, 4.2 and 4.3). The pore diameter and interpore distance values of the samples in our study were compared with the theoretically provided formulas in the literature. In our study, it was observed that as the voltage

and duration increased, the pore diameter and interpore distance values increased, aligning with the literature (Belwalkar et al., 2008).

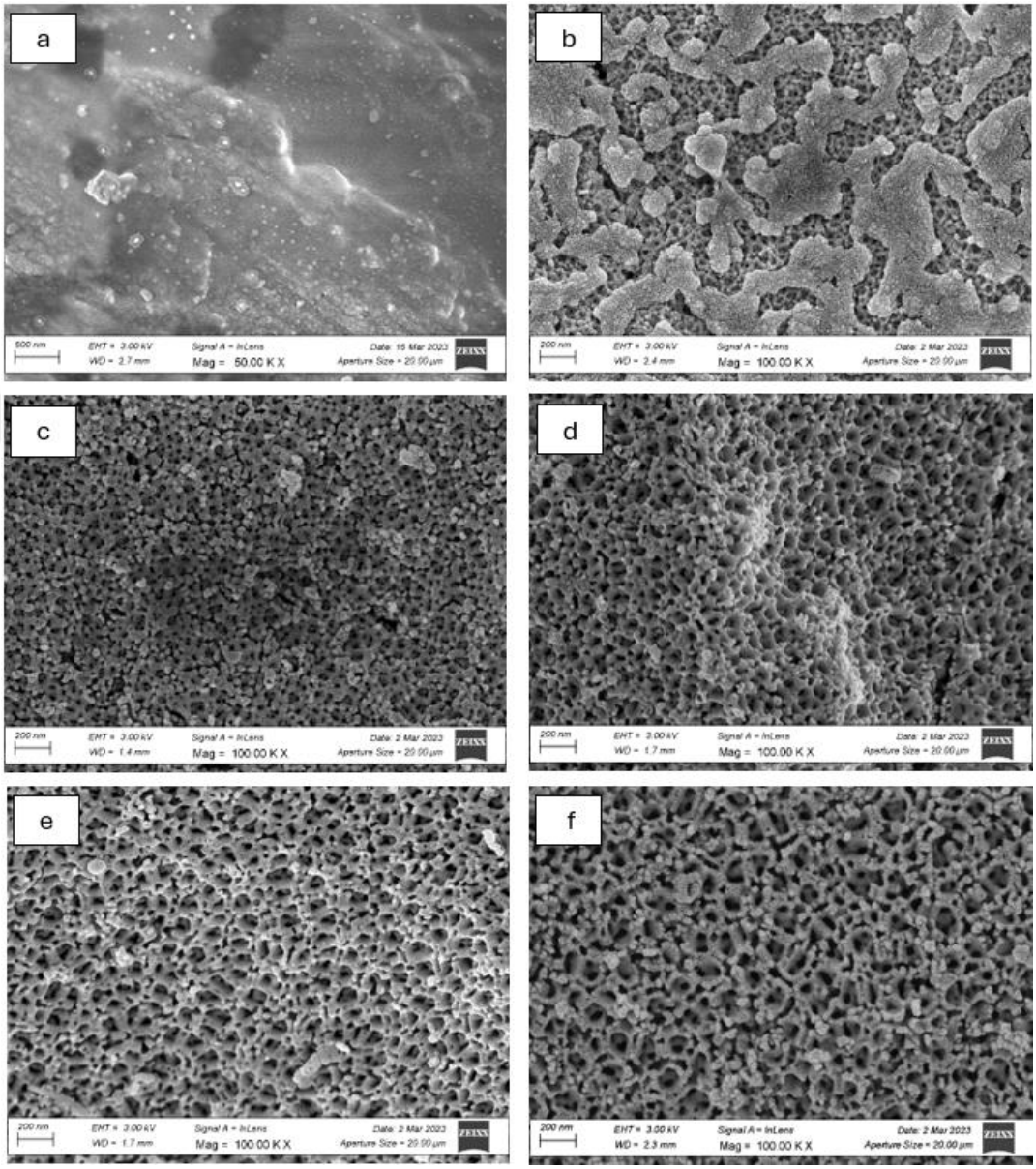


Figure 4.1 SEM graphs of (a) aluminum, (b) A20, (c) A30, (d) A40, (e) A50, (f) A60.

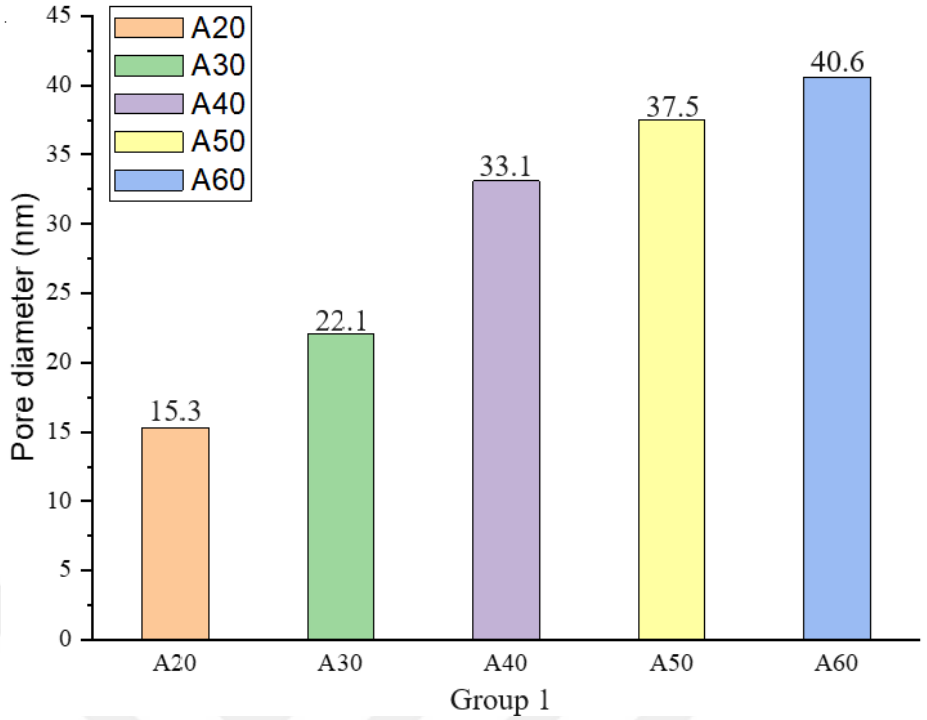


Figure 4.2 Graph of pore diameter values of Group 1.

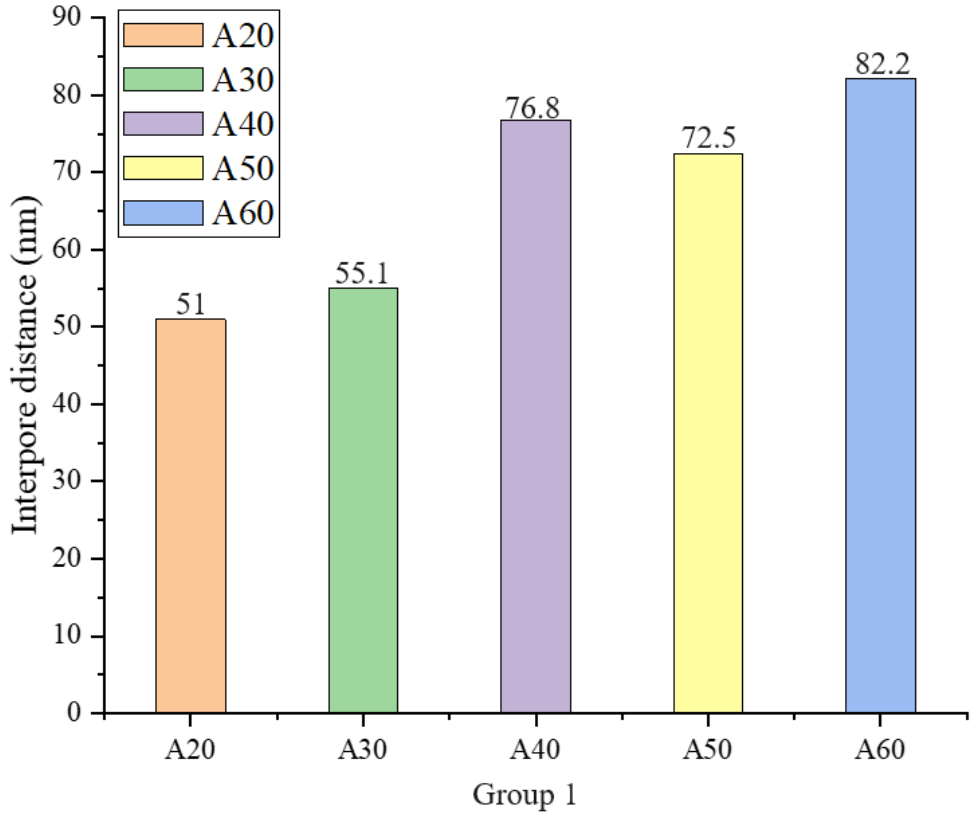


Figure 4.3 Graph of interpore distance values of Group 1.

Figure 4.1 shows the SEM images of Group 1. The images were taken at 100kx magnification. As a result of anodization performed in a 0.3 M oxalic acid electrolyte, it was observed that the pore diameters of Group 1 samples (A20, A30, A40, A50, A60) varied in the range of 15-40 nm, while the interpore distance values varied in the range of 51-82 nm. Increases in pore diameters and interpore distance values were observed as the applied potential increased. The pore diameter and interpore distance values of Group 1 are shown in Figure 4.2 and Figure 4.3 respectively. A linear relationship was observed between the applied potential and the pore diameter and interpore distance values. Thus, the pore diameter and interpore distance values are adjustable parameters. Since they vary depending on the application, the desired diameters and distances can be achieved simply by changing the applied potential.

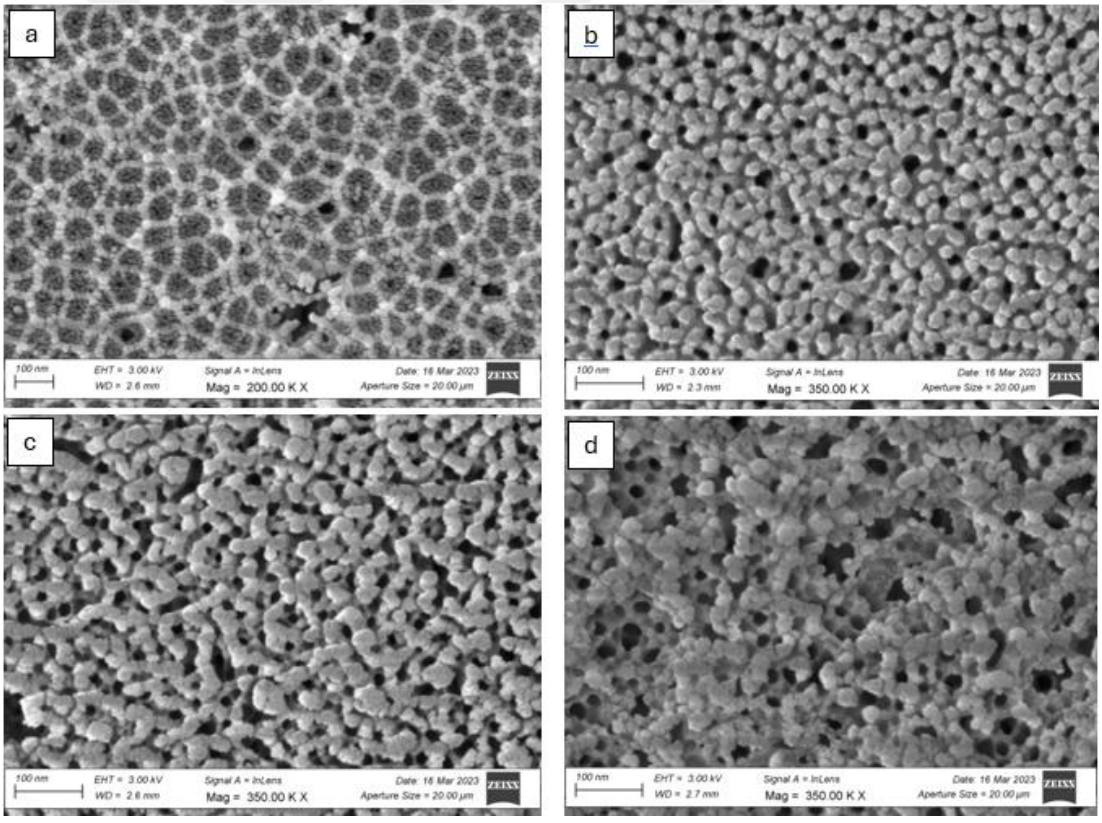


Figure 4.4 SEM images of Group 2. (a) A30-30, (b) A30-60, (c) A30-90, (d) A30-120.

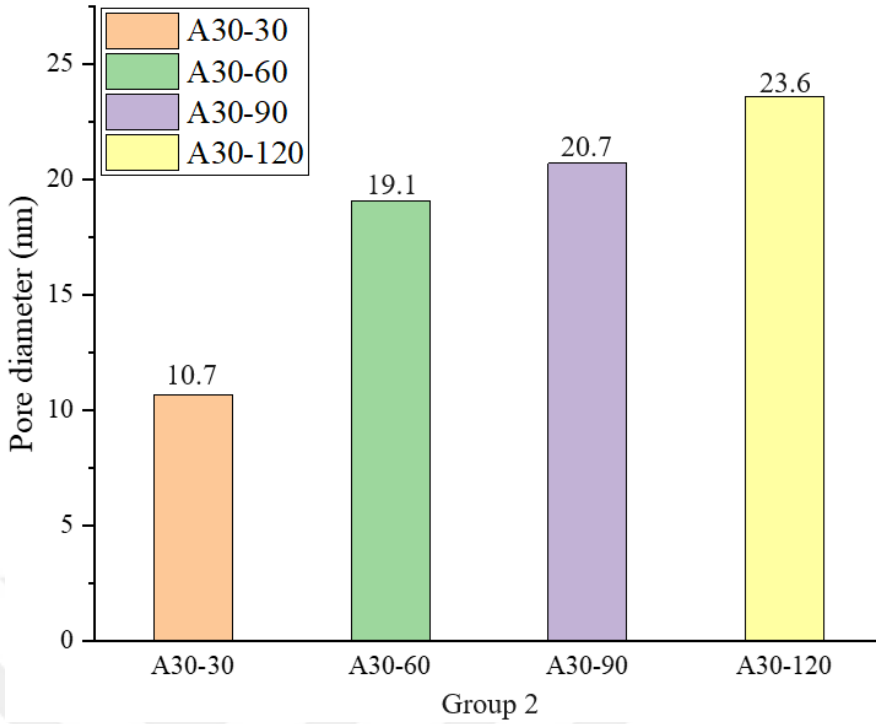


Figure 4.5 Pore diameter values of Group 2.

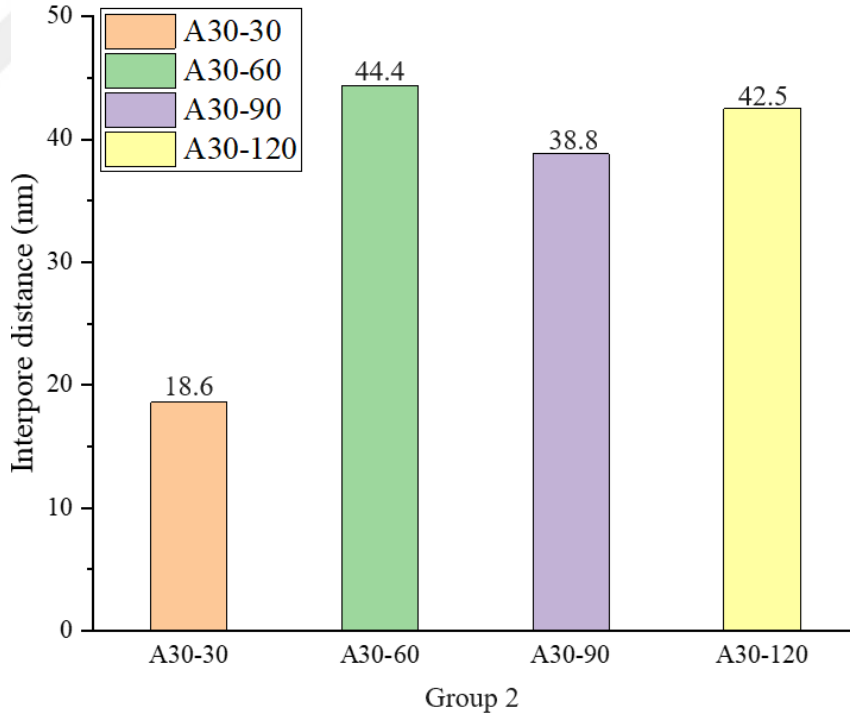


Figure 4.6 Interpore distance values of Group 2.

After the anodization of Group 1, a constant voltage (30 V) was selected, and for the subsequent experiments, a fixed voltage (30 V) and different durations (30-60-90-120 min.) were applied. The SEM images of Group 2 are shown in Figure 4.4. It was observed that a 30 minute anodization duration was sufficient for pore formation, but the desired pore structure was not achieved. In the anodization process conducted at different voltages, the effect of increasing voltage was found to be very significant; however, the differences in durations at the same voltage (excluding 30 and 60-90-120 min.) did not have a major impact. This indicates that a 30-minute anodization duration is too short. In the Group 2 samples, the pore diameter and interpore distance values were observed to range from 10-23 nm and 18-42 nm, respectively (Fig. 4.5 and Fig. 4.6).

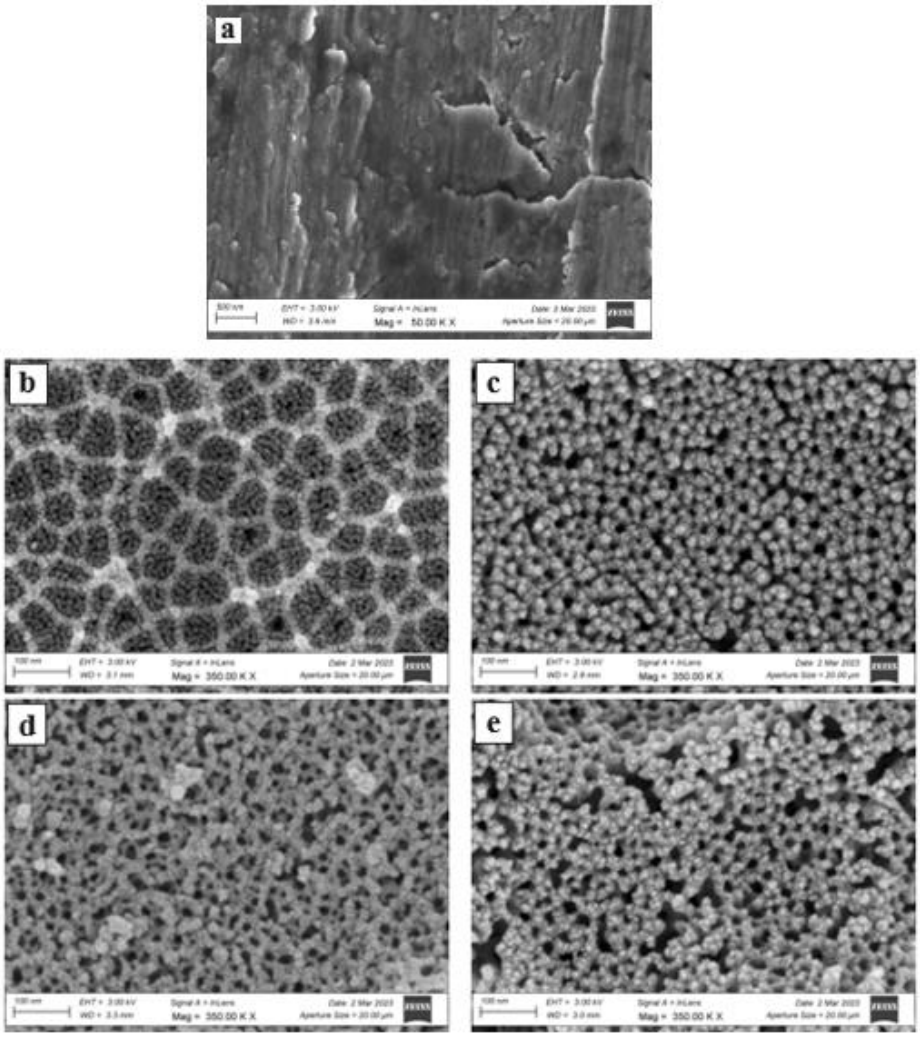


Figure 4.7 SEM images of Group 3. (a) aluminum, (b) NA30-30, (c) NA30-60, (d) NA30-90, (e) NA30-120.

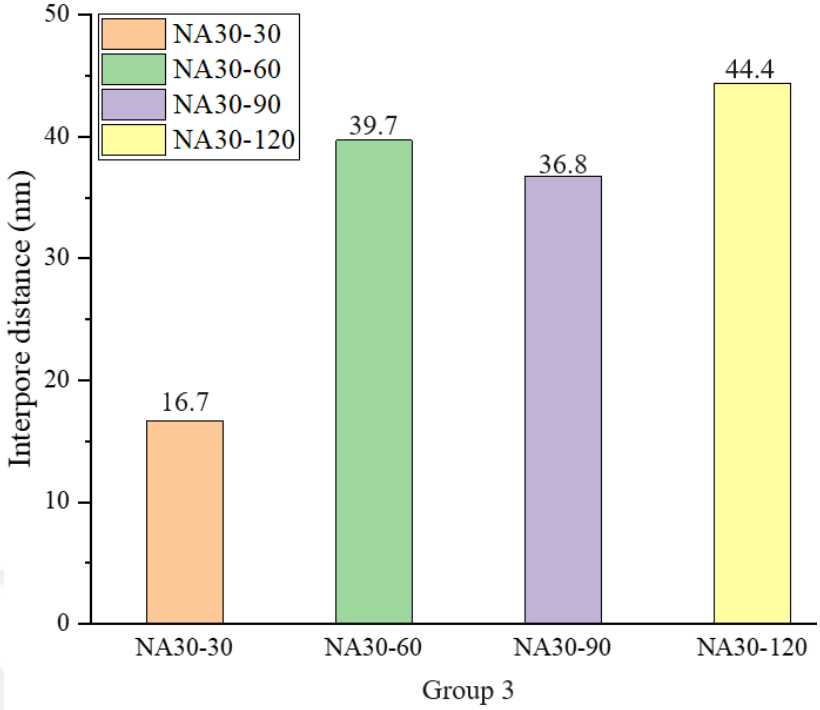


Figure 4.8 Pore diameter values of Group 3.

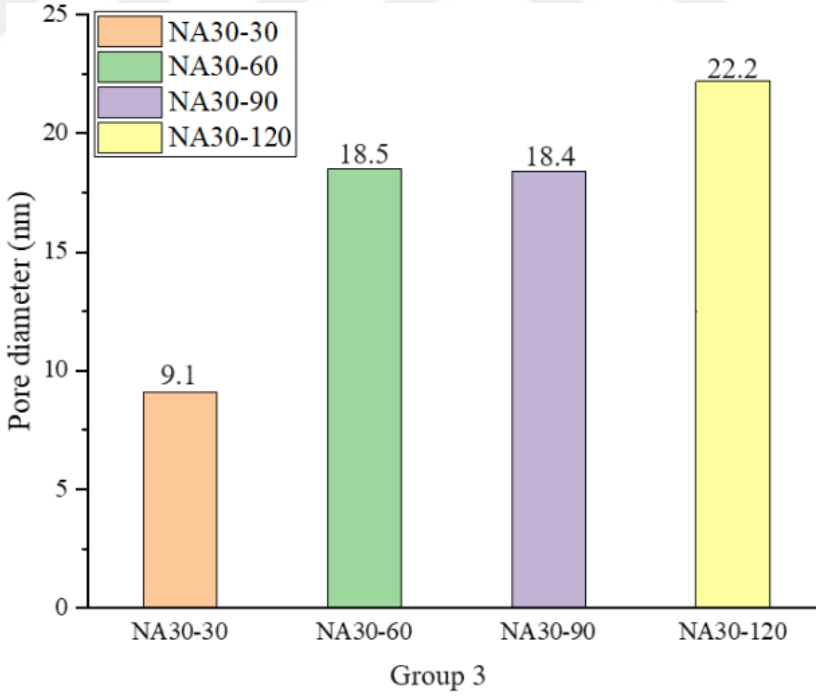


Figure 4.9 Interpore distance values of Group 3.

The SEM images of Group 3 are shown in Figure 4.7. As mentioned in the previous sections, Group 2 and Group 3 have the same anodization parameters, with the only

difference being that Group 3 underwent thermal treatment. In the Group 3 samples, the pore diameter and interpore distance values were observed to range from 9-22 nm and 16-44 nm, respectively (Fig. 4.8 and Fig. 4.9). These values are very similar to those of Group 2, indicating that thermal treatment does not affect the pore diameter and interpore distance values. Everything mentioned for Group 2 is also applicable to Group 3. It was observed in this group as well that the differences in durations at the same voltage (excluding 30 and 60-90-120 min.) did not have a significant impact.

4.2 Energy Dispersive Spectrometry (EDS) Analysis

EDS results of a non-anodized and an anodized sample were obtained to see the contents of the aluminum alloy. The EDS results are shown in Figure 4.10a and 4.10b. As mentioned earlier, aluminum has a natural oxide layer, and in Figure 4.10a, oxygen is seen at a low peak. On the other hand, in the anodized sample, the oxide layer is denser, so the oxygen peak is seen at a higher level. This also proves that the aluminum has been anodized.

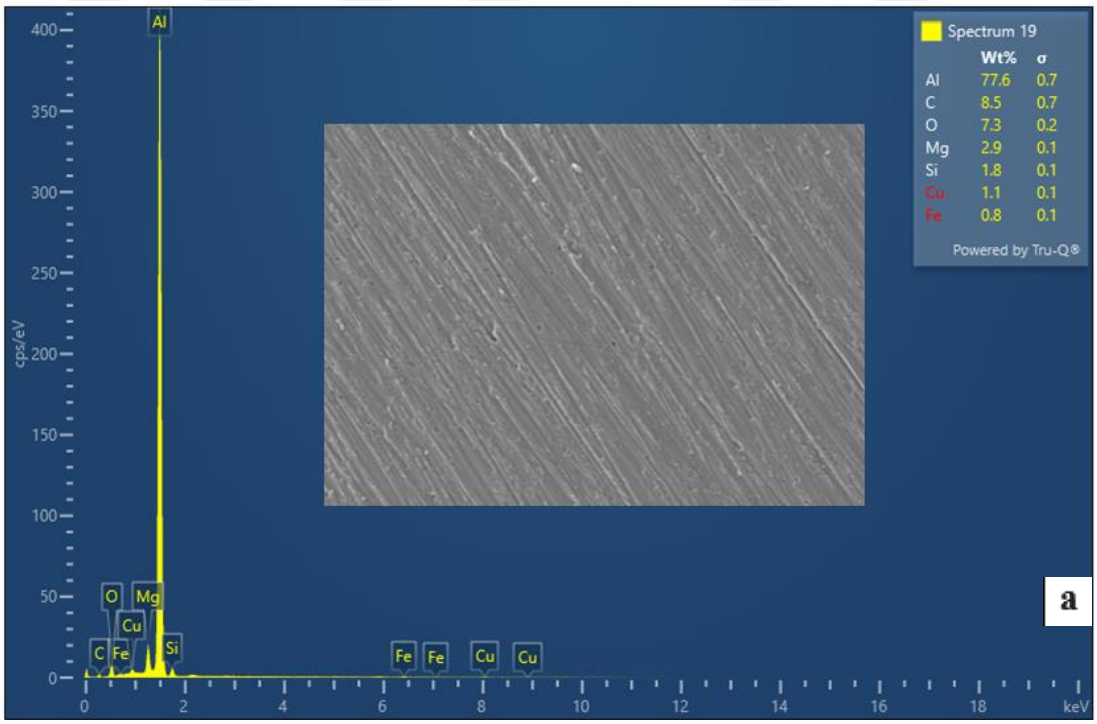


Figure 4.10 EDS values and SEM images of (a) non-anodized aluminum and (b) anodized aluminum.

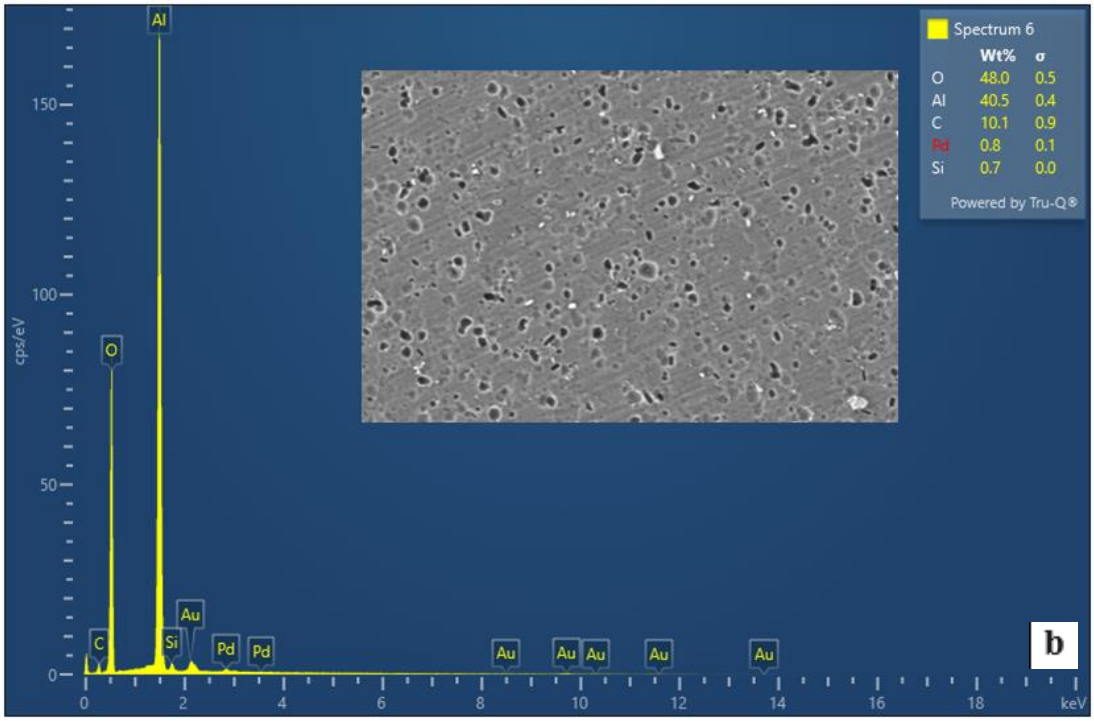


Figure 4.10 (continued) EDS values and SEM images of (a) non-anodized aluminum and (b) anodized aluminum.

The reason for the Au peak in Figure 4.10b is due to the gold coating applied before taking the SEM image. Gold coating is done to prepare the sample surface for SEM analysis, making the surface more conductive and providing a clearer image. Sputter Coating that used in this work. Besides the peaks in the images, the changes occurring on the aluminum surface can also be observed.

4.3 Pore Analysis

Pore analyses of Groups 1, 2, and 3 were conducted using SEM images and numerical values are calculated by using the ImageJ software. For each group's sample, the pore diameter and interpore distance values were measured for 30 instances and averaged, then recorded in Tables 4.1, 4.2, and 4.3. Additionally, comparisons were made with theoretical formulas obtained from the literature.

Table 4.1 Pore diameter and interpore distance values of Group 1.

Group 1	Pore Diameter (nm)			Interpore Distance (nm)	
	Our data	Data from Eq. 2.2	Data from Eq. 2.6	Our data	Data from Eq. 2.1
A20	15.3	18	19.1	51	50
A30	22.1	27	26.2	55.1	75
A40	33.1	36	33.3	76.8	100
A50	37.5	45	40.4	72.5	125
A60	40.6	54	47.5	82.2	150

Table 4.2 Pore diameter and interpore distance values of Group 2.

Group 2	Pore Diameter (nm)			Interpore Distance (nm)	
	Our data	Data from Eq. 2.2	Data from Eq. 2.6	Our data	Data from Eq 2.1
A30-30	10.7	27	26.2	18.6	75
A30-60	19.1			44.4	
A30-90	20.7			38.8	
A30-120	23.6			42.5	

Table 4.3 Pore diameter and interpore distance values of Group 3.

Group 3	Pore Diameter (nm)			Interpore Distance (nm)	
	Our data	Data from Eq. 2.2	Data from Eq. 2.6	Our data	Data from Eq. 2.1
NA30-30	9.1	27	26.2	16.7	75
NA30-60	18.5			39.7	
NA30-90	18.4			36.8	
NA30-120	22.2			44.4	

Pore analysis was conducted for all groups. In Table 4.1, 4.2 and 4.3 it was observed that pore diameter and interpore distance values were directly proportional to the applied potential. Additionally, the anodizing time was found to have an effect as well. According to all literature sources, pore diameter and interpore distance values are shown to be directly proportional to the applied potential, and our values, despite some

deviations, were found to be consistent with the literature. Although the 30-minute differences applied in Group 2 and Group 3 did not have a significant impact, it is predicted that extending this duration would noticeably increase the pore diameter and interpore distance values.

Table 4.4 Wall thickness, barrier layer thickness and wall thickness/barrier layer thickness values of Group 1

Group 1	W (nm)	B (nm)	W/B
A20	17.8	19.9	0.89
A30	16.5	18.4	
A40	21.8	24.4	
A50	17.5	19.6	
A60	20.8	23.2	

Table 4.5 Wall thickness, barrier layer thickness and wall thickness/barrier layer thickness values of Group 2

Group 2	W (nm)	B (nm)	W/B
A30-30	3.95	4.42	0.89
A30-60	12.65	14.1	
A30-90	9.05	10.1	
A30-120	9.45	10.5	0.9

Table 4.6 Wall thickness, barrier layer thickness and wall thickness/barrier layer thickness values of Group 3

Group 3	W (nm)	B (nm)	W/B
NA30-30	3.8	4.2	0.90
NA30-60	10.6	11.8	
NA30-90	9.2	10.3	
NA30-120	11.1	12.4	

In addition to pore diameter and interpore distance, other important properties such as wall thickness (W) and barrier layer thickness (B), pore density, and porosity values were also calculated for each group.

The wall thickness and barrier layer thickness have been calculated using formulas 2.16 and 2.15, and the values are shown in Table 4.4, Table 4.5 and Table 4.6. The barrier layer thickness is a distinctive feature for porous AAO films.

Ebihara and his friends (1983), observed a small relationship between wall thickness and barrier layer thickness during anodization in oxalic acid electrolyte at voltages between 5 and 40 V. The constant between A and B was measured to be approximately 0.66 in the range of 5-20 V. However, as the voltage increased, this constant increased to approximately 0.89. In our values, it can also be seen that the W/B ratio is 0.89.

Pore density (n) refers to the number of pores in the volume of a material. It is usually expressed as a percentage of pores per unit volume. In this study, numerical values for each group were calculated using the formula 2.20 and plotted as the number of pores per 1 micrometer. Figure 4.11 presents the pore density values of Group 1. Pore density decreases as interpore distance increases because an increase in interpore distance causes an increase in pore diameter, which consequently reduces the number of pores per unit area (Stępniowski, 2011). While high pore density in porous materials implies a higher surface area, it can also lead to a decrease in mechanical strength.

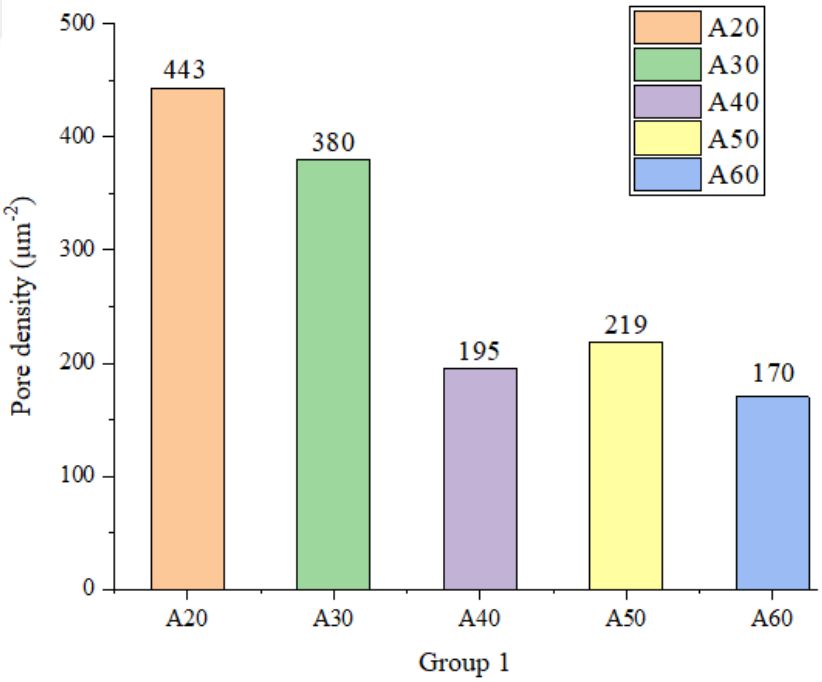


Figure 4.11 Pore density values of Group 1.

As expected, as the voltage increases, in other words, indirectly as the interpore distance increases, a decrease in pore density values has occurred. The voltage parameter is highly important not only for changing the interpore distance value but

also for affecting the pore density value (Wang et al., 2013; Sulka, 2008). Figures 4.12 and 4.13 present the pore density values of Group 2 and Group 3. A similar decrease is observed as in the samples from Group 1. It can be said that voltage and time have a significant effect on pore density.

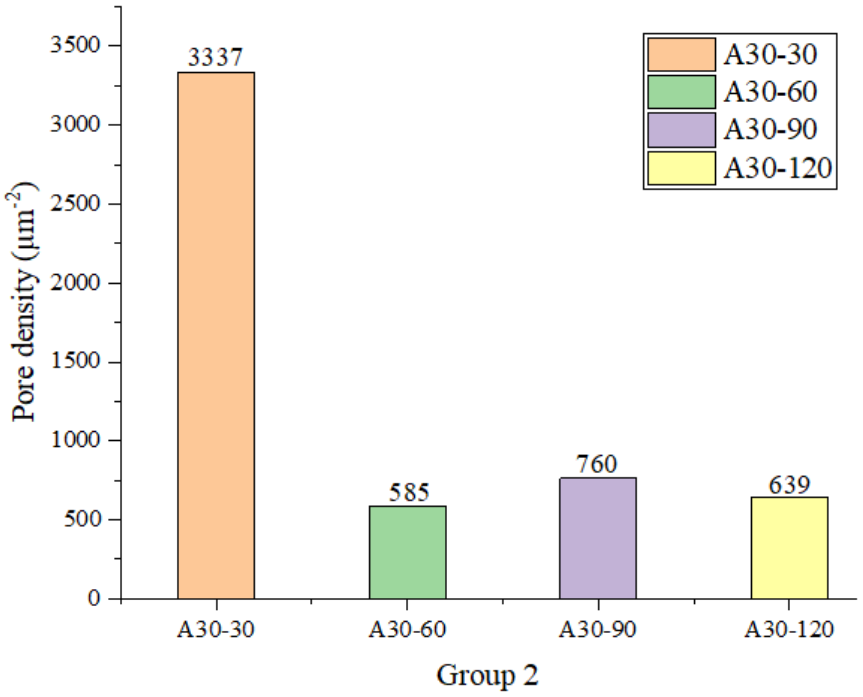


Figure 4.12 Pore density values of Group 2.

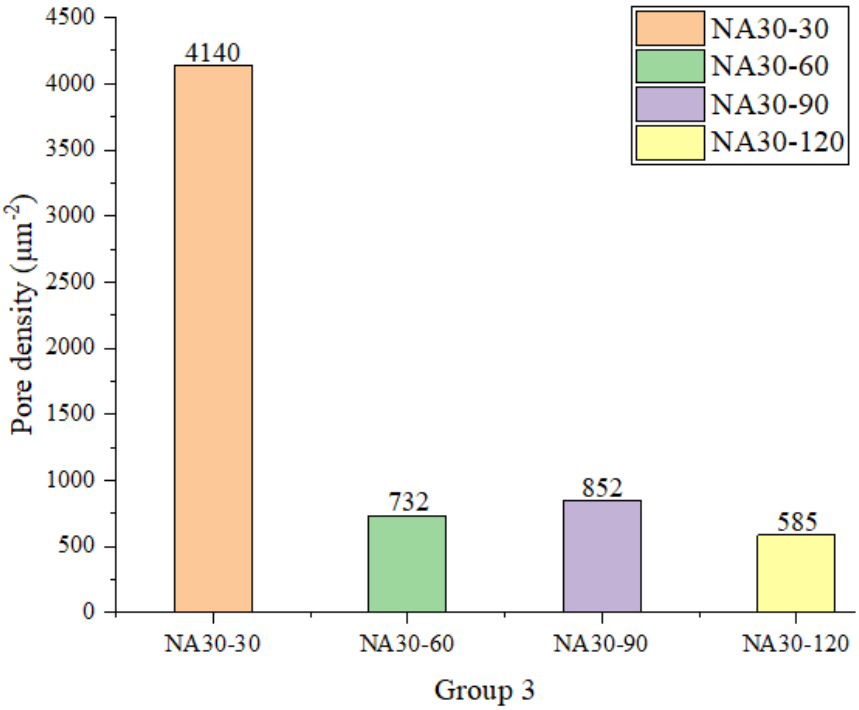


Figure 4.13 Pore density values of Group 3.

As seen from the SEM images and numerical values, in the A30-30 and NA30-30 samples, due to the short duration of anodization and the insufficient widening of pore diameters, there are many pores in the micrometer-square area compared to other samples. When we increase the anodization time to 1 hour, we can say that these small pores merge with other small pores to form a new pore, in other words, the pore diameters increase and the number of pores per unit area decreases (Ling. Z., & Li. Y., 2015).

Table 4.7 Porosity values of Group 1,2 and 3.

Group 1	Porosity (%)	Group 2	Porosity (%)	Group 3	Porosity (%)
A20	8.16	A30-30	30.0	NA30-30	26.9
A30	14.6	A30-60	16.8	NA30-60	19.7
A40	16.8	A30-90	25.8	NA30-90	22.7
A50	24.3	A30-120	28.0	NA30-120	22.7
A60	22.1				

Table 4.7 provides the porosity values for Group 1, Group 2, and Group 3. The porosity of nanostructures depends on the rate of oxidation and chemical dissolution. As an anodization parameter, it depends on the type of electrolyte, its temperature, concentration, and the anodization duration. The parameter that most significantly affects porosity is the voltage applied to the electrolyte and the pH of the electrolyte solution. There are inconsistencies in the literature regarding the data on this property. The porosity value ranges between 8 % and 30 %. The porosity rule, which was originally formulated for the AAO under ideal anodizing conditions, generally dictates that self-organized anodic porous alumina should have a porosity level of 10%, regardless of the anodizing potential, electrolyte type, or conditions (Wang et al., 2013).

4.4 XRD Analysis

XRD analysis was performed on all groups to examine the crystallographic structure of the materials. In Figure 4.14, the XRD patterns of un-anodized aluminum alloy are shown, while in Figure 4.15, the XRD patterns of samples anodized at

different voltages are presented. In the first graph, the specific peaks of aluminum at 37.71°, 44.06°, 77.68°, and 81.84° correspond to the (111), (200), (311), and (222) planes, respectively (Syamdri et al., 2020). The peaks at 18-21 degrees are attributed to the compounds formed by the interaction of Mg, Si, and Al elements within the Al 6XXX series. After anodization, the theta values of the un-anodized aluminum have shifted by 1-2 degrees to the right (X. Y. Goh., et al 2023; Xu et al. 2019). The characteristic peak values of aluminum were found to be consistent with the literature

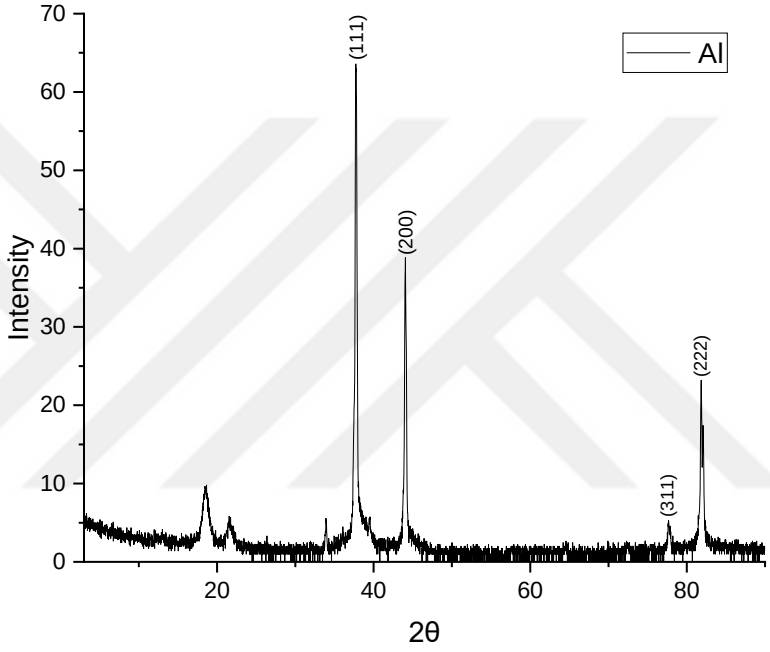


Figure 4.14 XRD graph of aluminum.

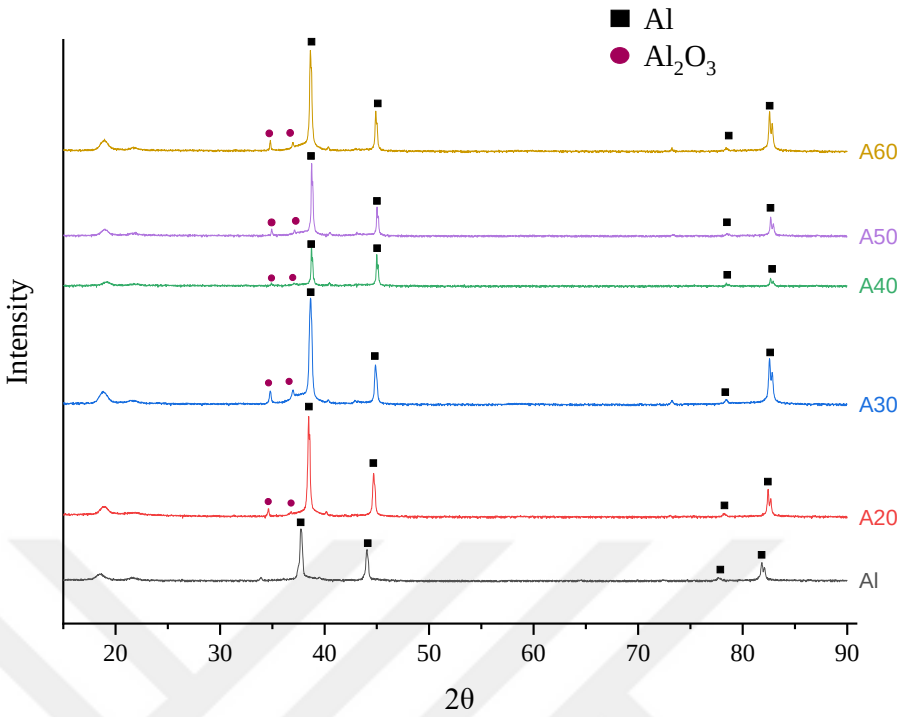


Figure 4.15 XRD graphs of Group 1.

The XRD analysis of Group 1 is shown in the graph above. The values ranging from 34.70 to 38.68 degrees are attributed to Al_2O_3. Additionally, the intensity values have increased compared to the non-anodized sample, except for the 40 V sample. It can be said that the oxide films contained both crystalline and non-crystalline phases. There are also different peaks corresponding aluminum oxide and silicon oxide phases (Zhu et al., 2021). As mentioned above, the reason for the shifts could be due to changes in the ratios or distributions of elements on the surface of the aluminum alloy during the anodization process, which can affect the parameters of the crystal structure and consequently lead to shifts in the XRD patterns (Pandey et al., 2020).

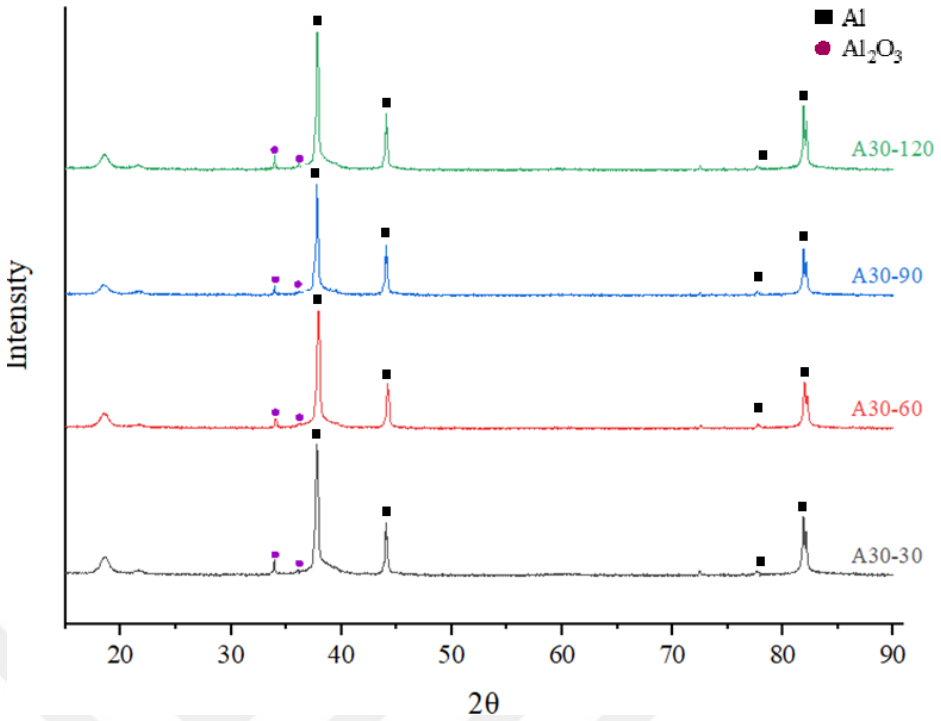


Figure 4.16 XRD graphs of Group 2.

The XRD graph of Group 2 is shown in Figure 4.16. Al_2O_3 peaks were found at 33.90 and 36.09 for A30-30, at 34.02 and 36.21 for A30-60, at 33.92 and 36.15 for A30-90, and at 33.90 and 36.09 for A30-120. These observations align with the previous data that specified Al_2O_3 peaks at particular 2θ values for each sample (Zhu et al., 2021). The similarity in peak positions suggests that the same crystalline phases are present in all samples, with slight variations in their peak positions and intensities. The intensity values of Group 2 were also higher than the intensity values of the non-anodized aluminum alloy.

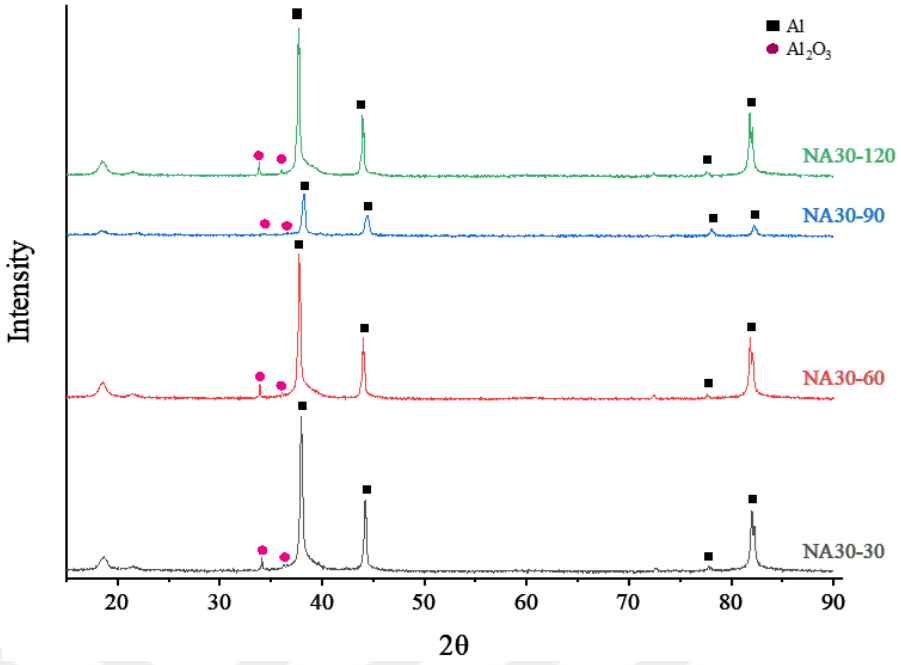


Figure 4.17 XRD graphs of Group 3.

The XRD images of Group 3 are given in the graph in Figure 4.17. The peaks corresponding to Al_2O_3 for NA30-30 are at 34.13 and 36.25. For NA30-60, the peaks are at 33.91 and 36.08. For NA30-90, they are at 34.27 and 36.63, and finally, for NA30-120, the peaks are at 33.86 and 36.01. The intensity values are similar to those of Group 1 and Group 2. According to the XRD results obtained from anodic oxidation, the Al_2O_3 peaks were also found to be consistent with the literatüre (Shamsuddin et al., 2021).

4.5 AFM Analysis

Atomic force microscopy (AFM) is a crucial tool in the analysis of nanoporous anodic aluminum oxide (AAO) membranes. AFM plays a significant role in the analysis and characterization of AAO membranes and nanostructures. Its ability to provide high-resolution imaging and detailed surface analysis makes it a valuable tool in studying the properties and behavior of nanoporous materials.

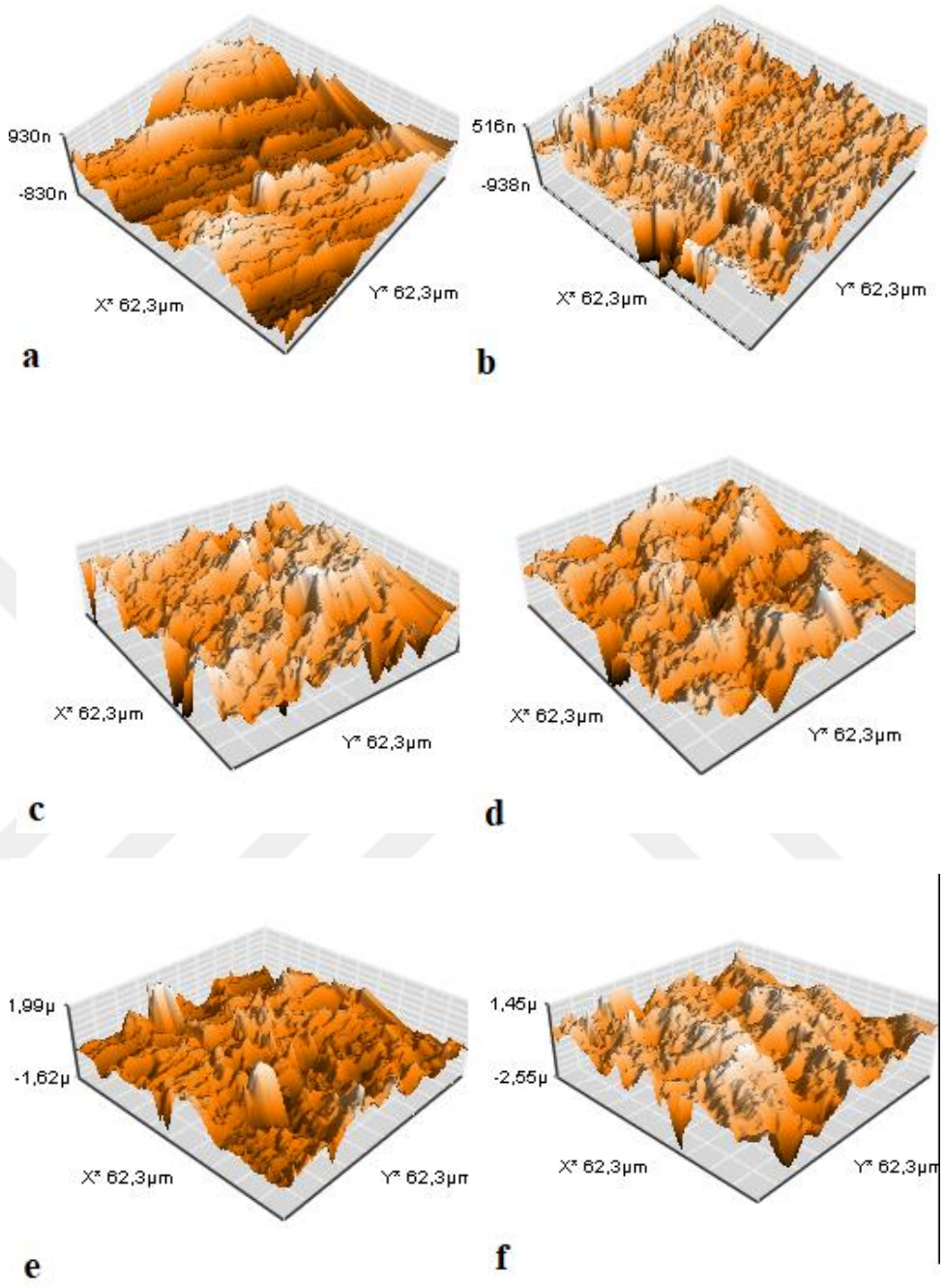


Figure 4.18 3D Z-Scan graphs of (a) aluminum, (b) A20, (c) A30, (d) A40, (e) A50, (f) A60.

AFM analysis was performed on the all samples, as well as on non-anodized aluminum. Deflection and Z-scan analyses were conducted on all samples except A30-30. If we look at the 3D Z-scan images in Figure 4.18, we can say that we encounter a more peaked and indented surface compared to unanodized aluminum.

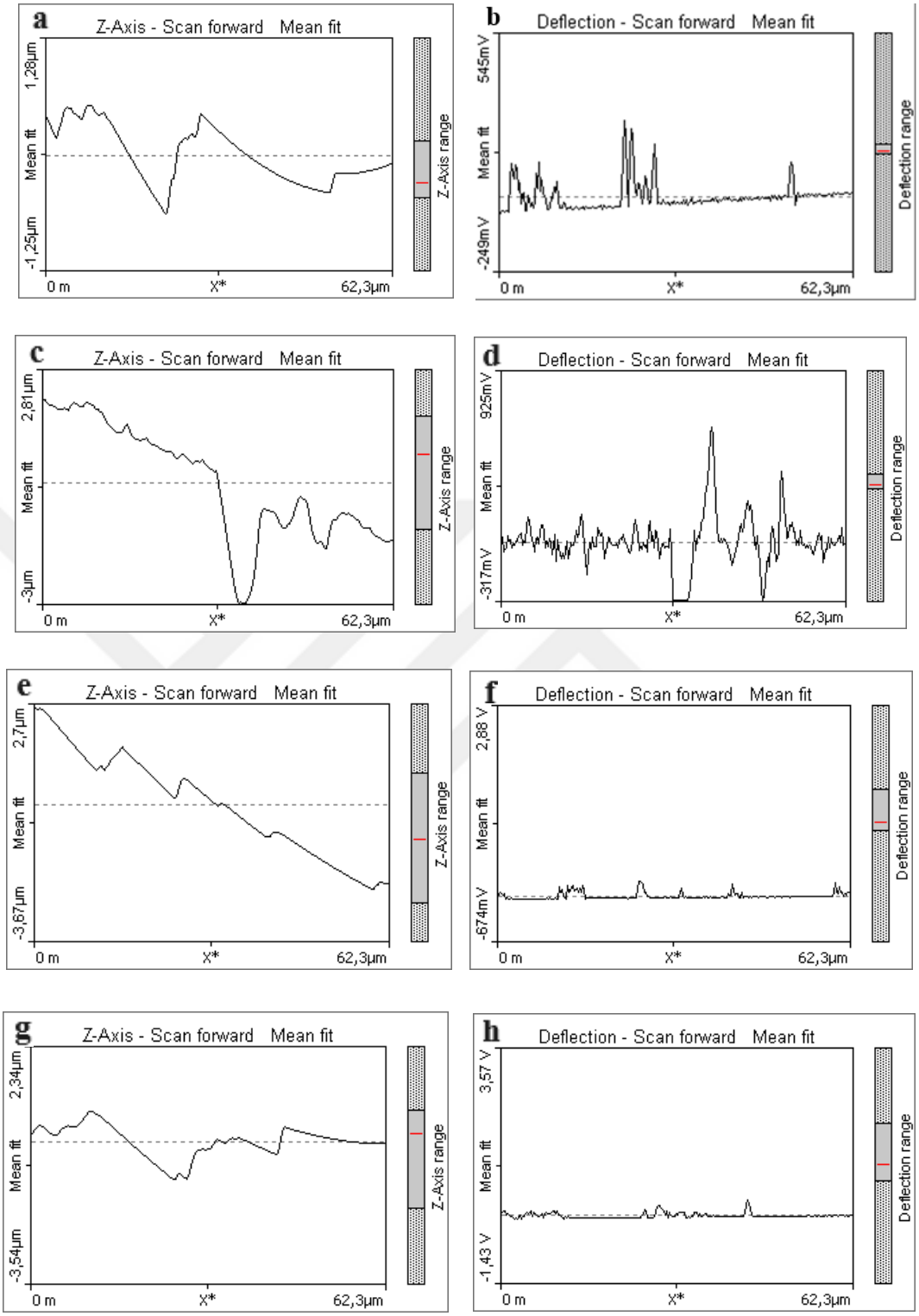


Figure 4.19 Z-Scan and deflection graphs of (a-b) aluminum, (c-d) A20, (e-f) A30, (g-h) A40, (i-j) A50, (k-l) A60.

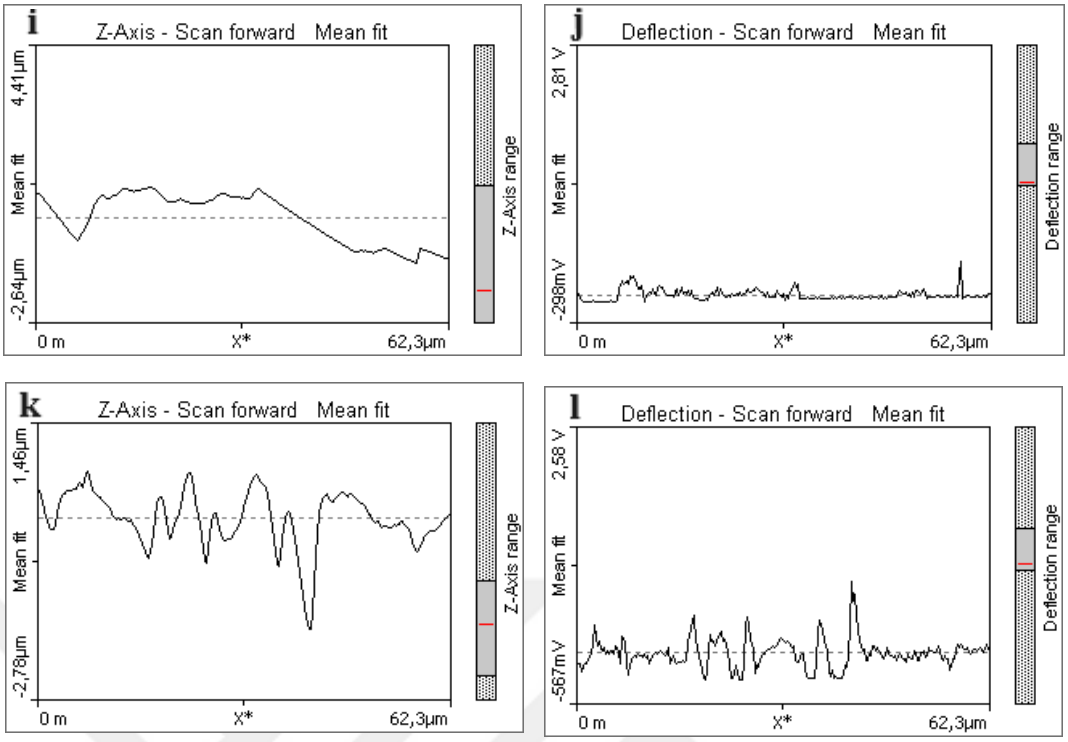


Figure 4.19 (continued) Z-Scan and deflection graphs of (a-b) aluminum, (c-d) A20, (e-f) A30, (g-h) A40, (i-j) A50, (k-l) A60.

The AFM analysis was conducted by scanning at a Scan Rate of 1 Hz over an area of 62.3 x 62.3 micrometers square for all specimens of Group 1,2 and 3 except A30-30.The aluminum surface exhibited a rougher and more scattered pattern of pits and peaks after the anodization process for both groups. Deflection images (Figure 4.19) show the deviations that occur during the interaction of the probe with the surface. High deflection indicates hard or elevated areas on the surface, while low deflection indicates soft or low areas. Z-scan images (Figure 4.19) show the vertical movements of the probe along the surface. They provide information about the surface height profile. Elevated areas are represented by upward movement along the Z-axis, while low areas are represented by downward movement along the Z-axis. Since the surface of the unanodized sample is irregular, deviations are observed in the deflection graph. As the samples are anodized, these deviations decrease. The deviations in the A20 sample (Figure 4.19d) are due to the presence of many impurities and the insufficient voltage, as previously described and seen in the SEM images. This results in an

irregular or incomplete formation of the oxide layer, making its surface much rougher compared to the other samples.

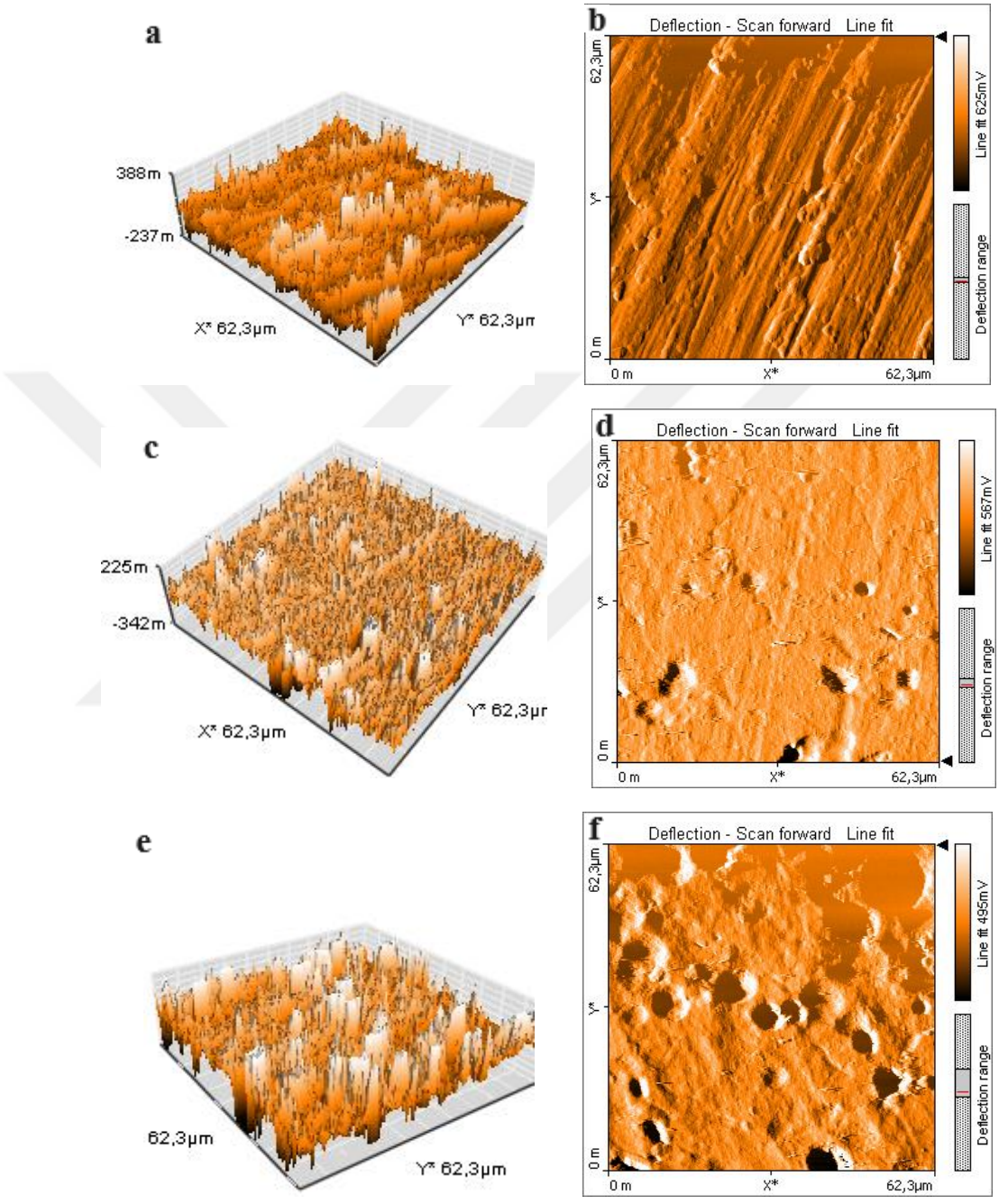


Figure 4.20 Deflection 3D and 2D graphs of (a-b) aluminum, (c-d) A20, (e-f) A30, (g-h) A40, (i-j) A50, (k-l) A60.

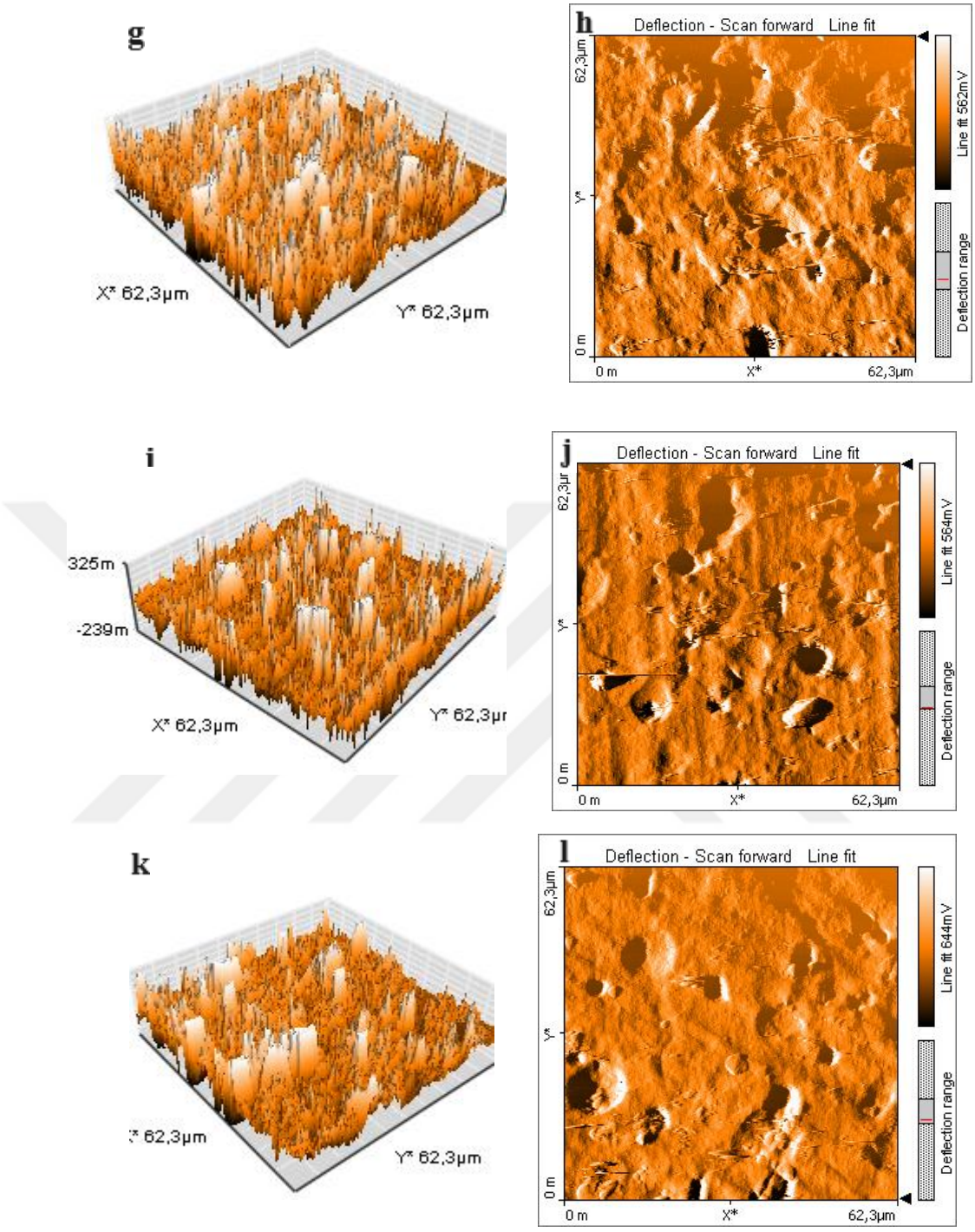


Figure 4.20 (continued) Deflection 3D and 2D graphs of (a-b) aluminum, (c-d) A20, (e-f) A30, (g-h) A40, (i-j) A50, (k-l) A60.

Figure 4.20 shows the deflection 2D and 3D images of Group 1 samples and unanodized aluminum. The surface of the unanodized sample and the pits on the surfaces of the anodized samples are clearly visible.

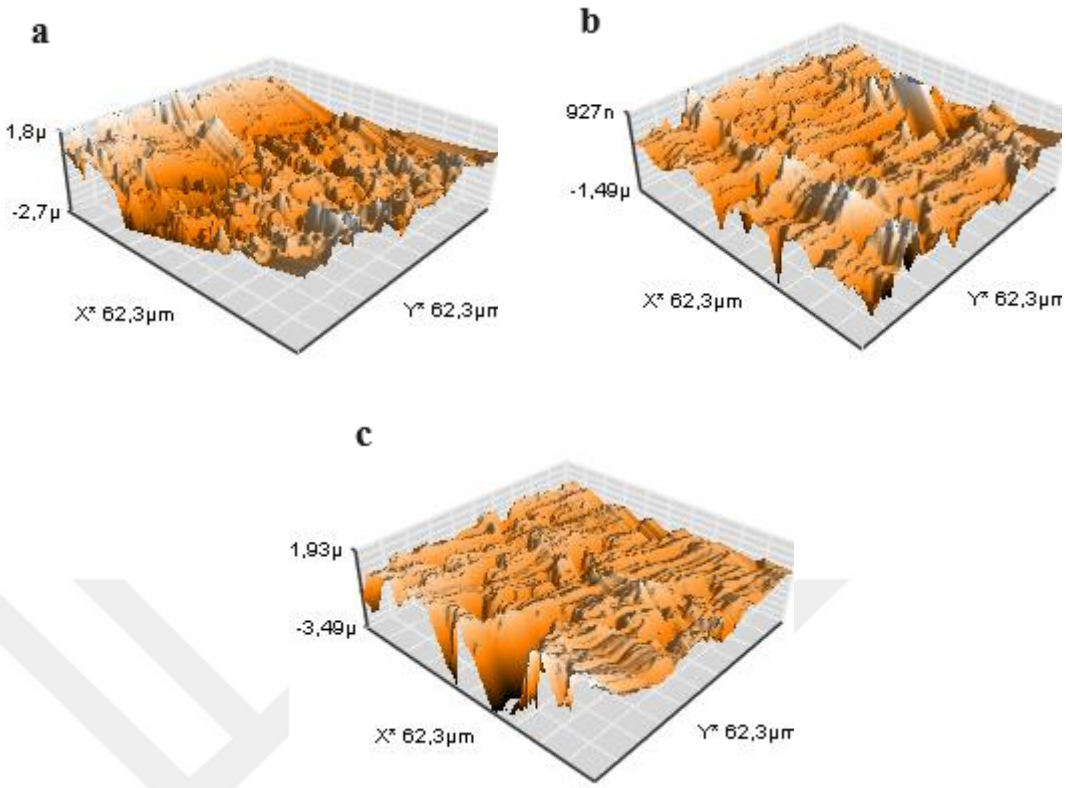


Figure 4.21 Z-scan 3d graphs of (a) A30-60, (b) A30-90 and (c) A30-120.

When Figure 4.21 is examined, it can be observed that in the Z-scan graphs, compared to unanodized aluminum, there are more peaks, or in other words, more frequent probe movement in the Z direction, in the A30-60, A30-90, and A30-120 graphs like the Group 1.

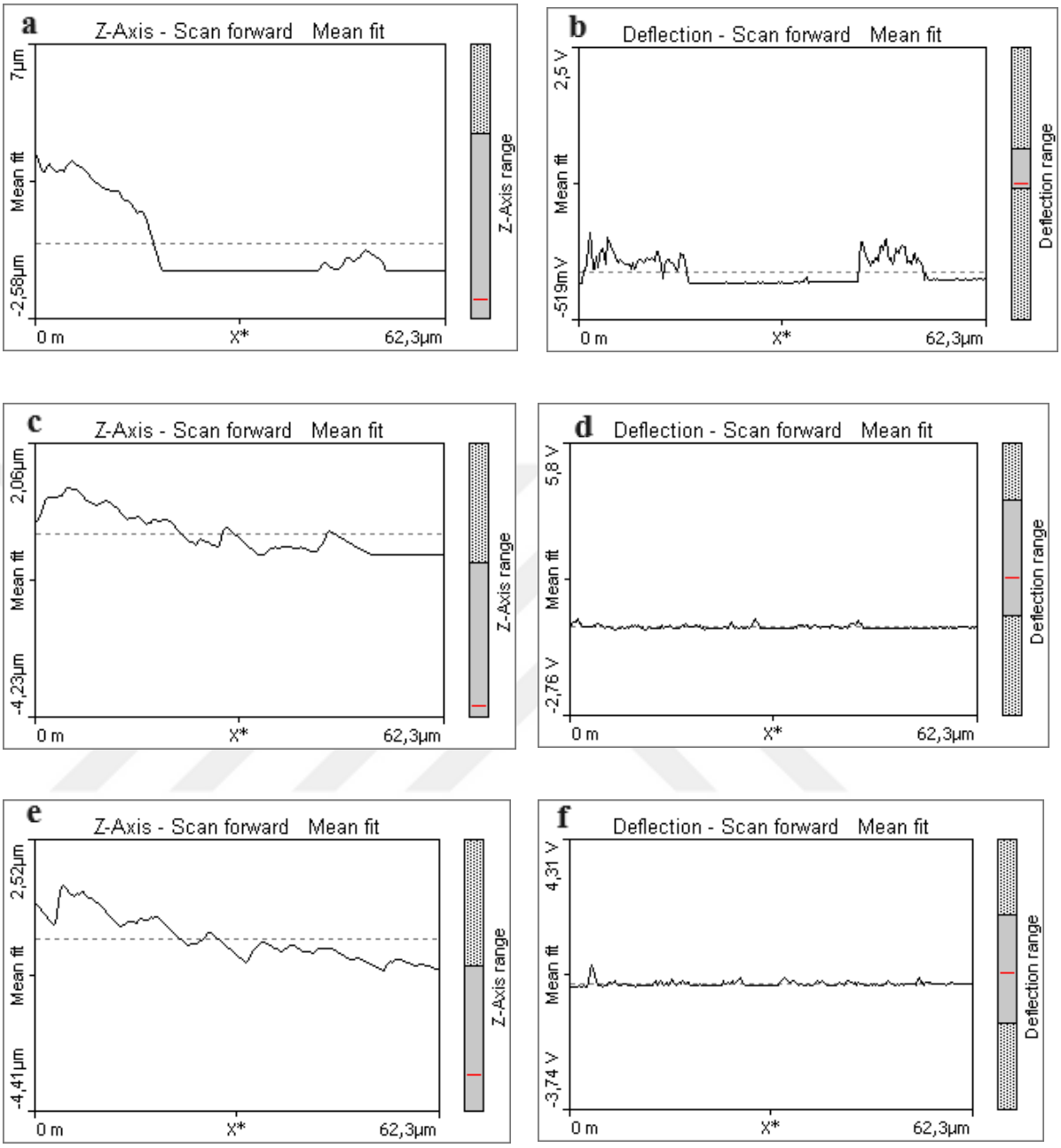


Figure 4.22 Z-Scan and deflection graphs of (a-b) A30-60, (c-d) A30-90, (e-f) A30-120

In the deflection graph in Figure 4.22, the deflection value of unanodized aluminum is much higher compared to the group 2 samples. This is because the surface of unanodized aluminum is much rougher, whereas after anodization, the surface becomes smoother.

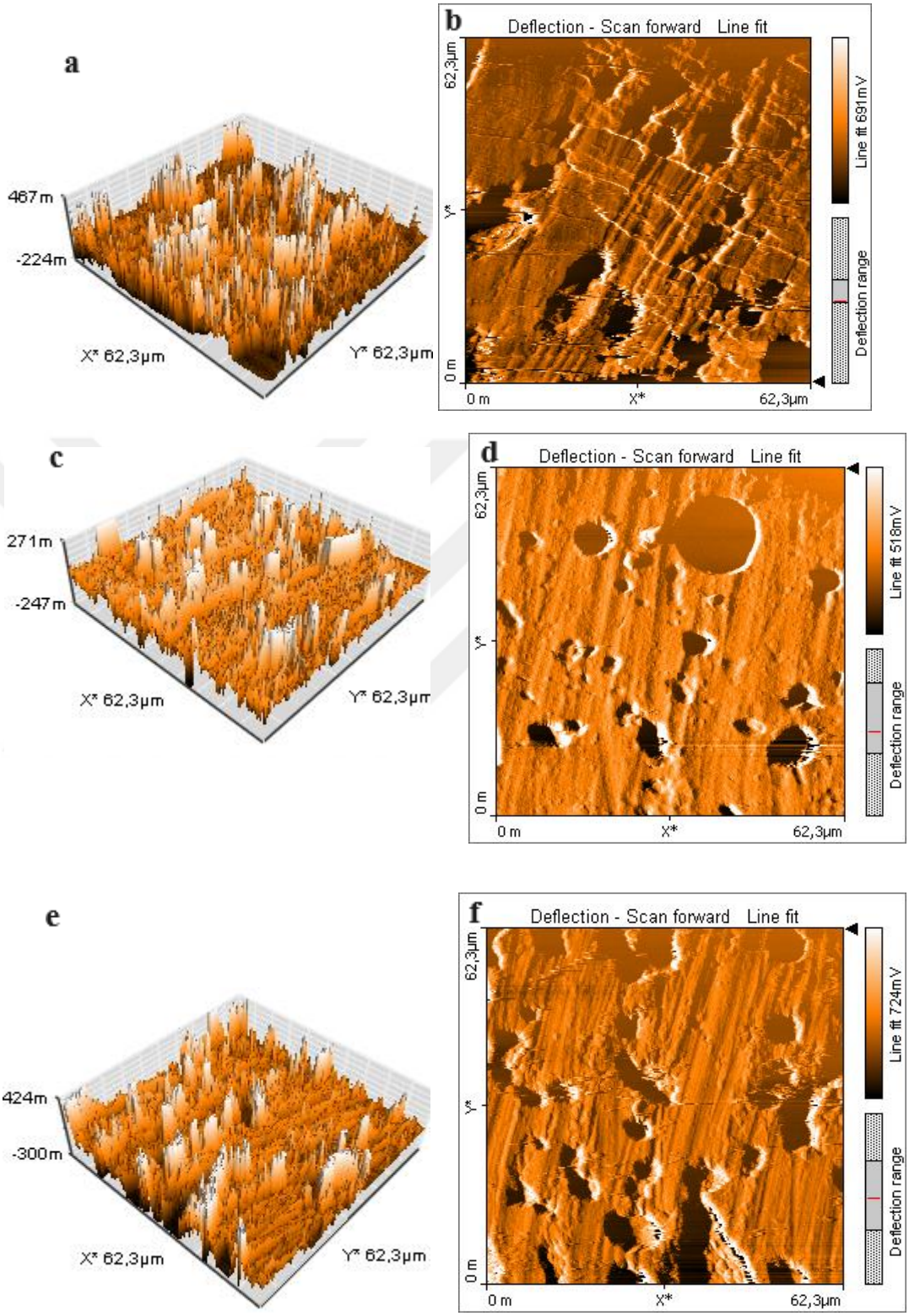


Figure 4.23 3D and 2D deflection graphs of (a-b) A30-60, (c-d) A30-90, (e-f) A30-120.

The Line fit values in the 2D graphs indicate the scale of the deflection signal in millivolts. This scale shows the range of deflection values measured during the AFM scan. The mV value represents the maximum deflection value fitted to a line during the scan. Figure 4.23 shows 3D and 2D deflection graphs. In the 2D deflection graph of the non-anodized aluminum, no pits are visible, whereas pits and surface variations are observed in the anodized samples. The microstructures of these samples correspond to the bottom of the nanopores or the protrusions of the barrier layer (Ling-Bin et al., 2003).

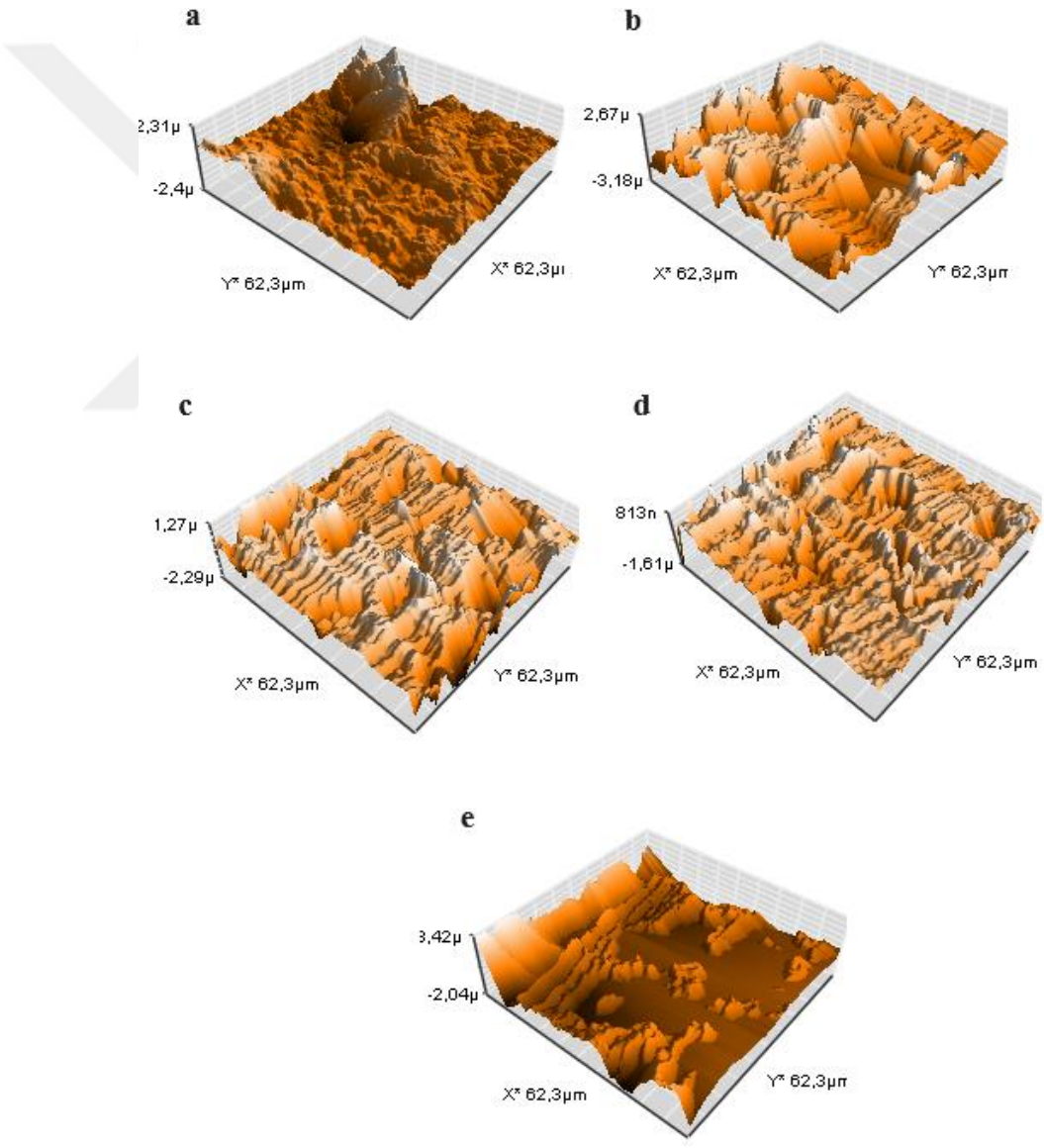


Figure 4.24 Z-Scan graphs of (a) aluminum, (b) NA30-30, (c) NA30-60, (d) NA30-90, (e) NA30-120.

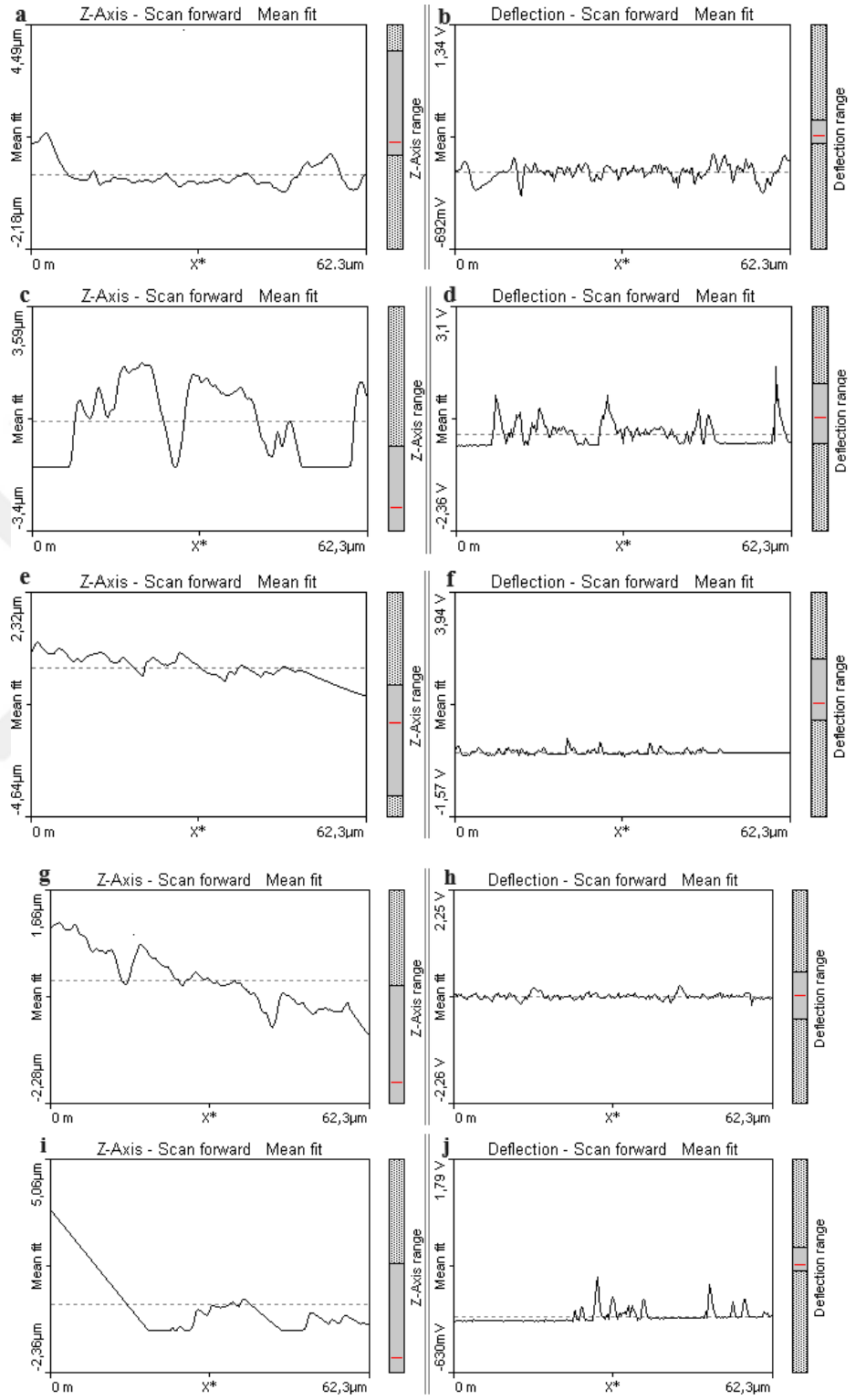


Figure 4.25 Z-Scan and deflection graphs of (a-b) aluminum, (c-d) NA30-30, (e-f) NA30-60, (g-h) NA30-90, (i-j) NA30-120.

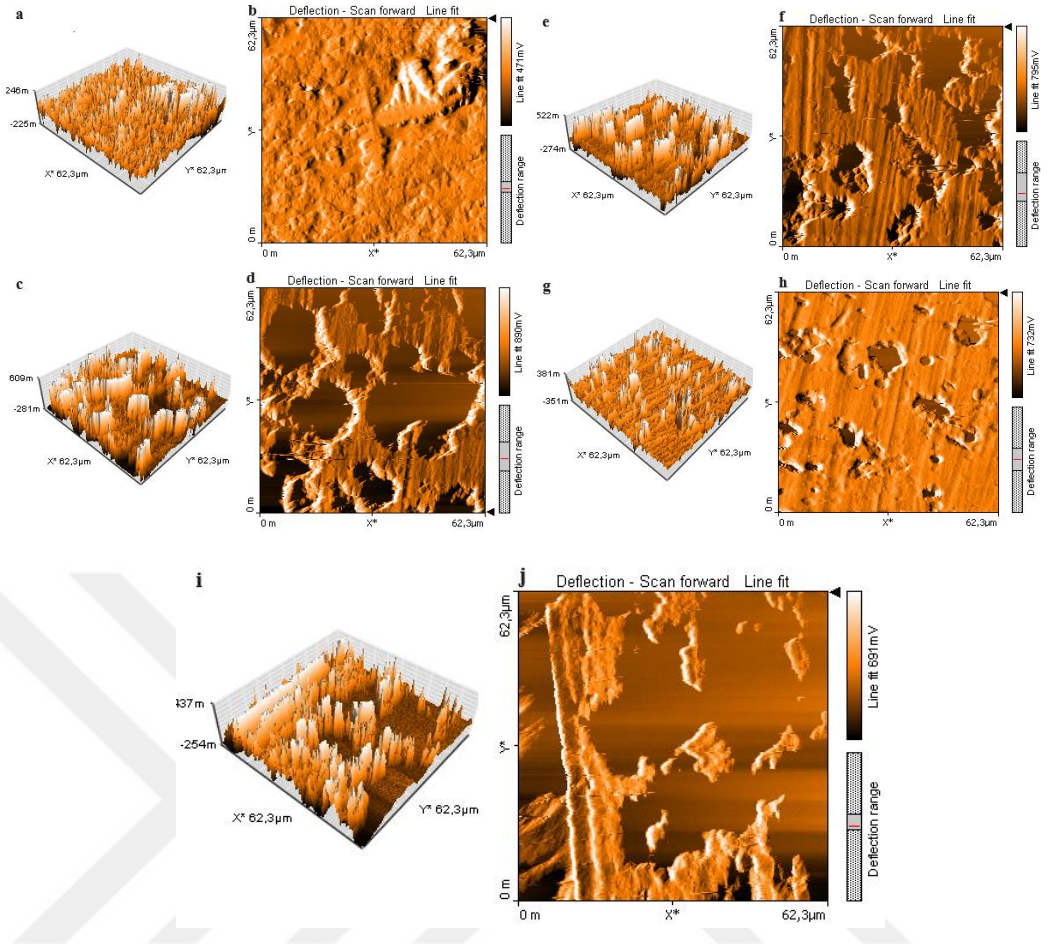


Figure 4.26 Deflection 3D and 2D graphs of (a-b) aluminum, (c-d) NA30-30, (e-f) NA30-60, (g-h) NA30-90, (i-j) NA30-120.

Similar images to the other results were obtained in Figure 4.24. Differences are observed between the surface of the non-anodized aluminum and the surfaces of the anodized samples. In Figure 4.25, the deflection values of the anodized samples are lower compared to the non-anodized sample. This indicates that the surface is more uniform and suggests that the lateral forces or obstacles detected by the probe are fewer. Supporting 3D and 2D deflection images for this are shown in Figure 4.26.

4.6 Surface Roughness Analysis

Surface roughness analysis is a method used to determine the surface roughness of a material, typically conducted using various parameters and metrics. The profilometer is commonly used as a contact method, where a probe or stylus moves along the surface and measures its height. R_a is the arithmetic average roughness. R_y (R_{max})

represents the maximum roughness height. R_z is the sum of the highest peak height and the depth of the lowest valley over the evaluation length, and R_q is the root mean square roughness (Mohamed, 2019).

Table 4.8 Surface roughness values of Group 1.

Group 1	Al	A20	A30	A40	A50	A60
R_a	0.35	0.21	0.62	0.50	0.39	0.41
R_y	2.94	1.91	5.04	5.78	3.22	3.4
R_z	2.52	1.33	3.99	3.89	2.47	2.50
R_q	0.57	0.30	0.81	0.76	0.50	0.53

Table 4.9 Surface roughness values of Group 2.

Group 2	A30-30	A30-60	A30-90	A30-120
R_a	1.91	0.64	1.16	0.72
R_y	10.7	2.51	4.35	6.74
R_z	8.80	1.51	6.18	5.05
R_q	2.4	0.4	1.58	1.09

Table 4.10 Surface roughness values of Group 3.

Group 3	NA30-30	NA30-60	NA30-90	NA30-120
R_a	1.84	1.28	1.40	1.32
R_y	9.86	11.1	10.52	9.10
R_z	8.25	8.45	8.28	7.02
R_q	2.15	1.96	2.05	1.70

Surface roughness is utilized to measure the texture of a surface and is determined by the vertical deviations of a real surface from its ideal form. Large deviations indicate a rough surface with higher friction coefficients. Conversely, small deviations correspond to a smooth surface with lower friction coefficients. Roughness significantly influences how an object interacts with its environment. The surface roughness value can be used to predict the mechanical performance of an individual mechanical component; irregularities on the surface may act as nucleation sites for cracks or corrosion, leading to reduced fatigue life and corrosion resistance (E. K. S. Maawad, 2012). Generally, in Table 4.8, the Group 1 values show that the A30 sample

has a higher surface roughness compared to the other samples. In Table 4.9, the highest roughness is observed in the A30-30 sample, while the lowest is in the A30-120 sample. Similarly, in Table 4.10 for Group 3, the values resemble those in Group 2 regarding the time parameter. The NA30-30 sample has the highest roughness, and the NA30-120 sample the lowest. In both Group 2 and Group 3 samples, surface roughness decreases as the time increases. This is because the surface roughness tends to increase with the porosity of the aluminum oxide layer. Coatings with a higher O/Al ratio were observed to be rougher (Choudhary et al., 2017). For the non-heat-treated Group 3 samples, the R_a values range between 1.32 µm and 1.84 µm, whereas, for heat-treated Group 1 and Group 2 samples, the R_a values range between 0.21 µm - 0.62 µm and 0.64 µm - 1.91 µm, respectively.

4.7 Water Contact Angle Analysis

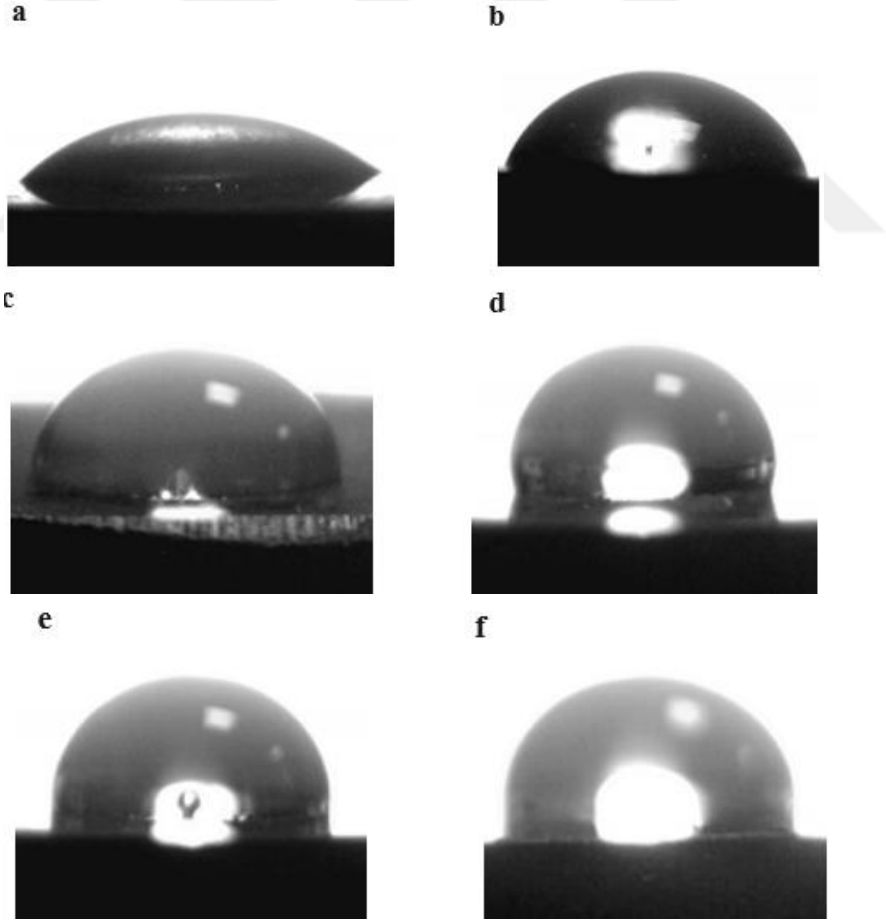


Figure 4.27 Water contact angle images of Group 1. (a) aluminum, (b) A20, (c) A30, (d) A40, (e) A50, (f) A60.

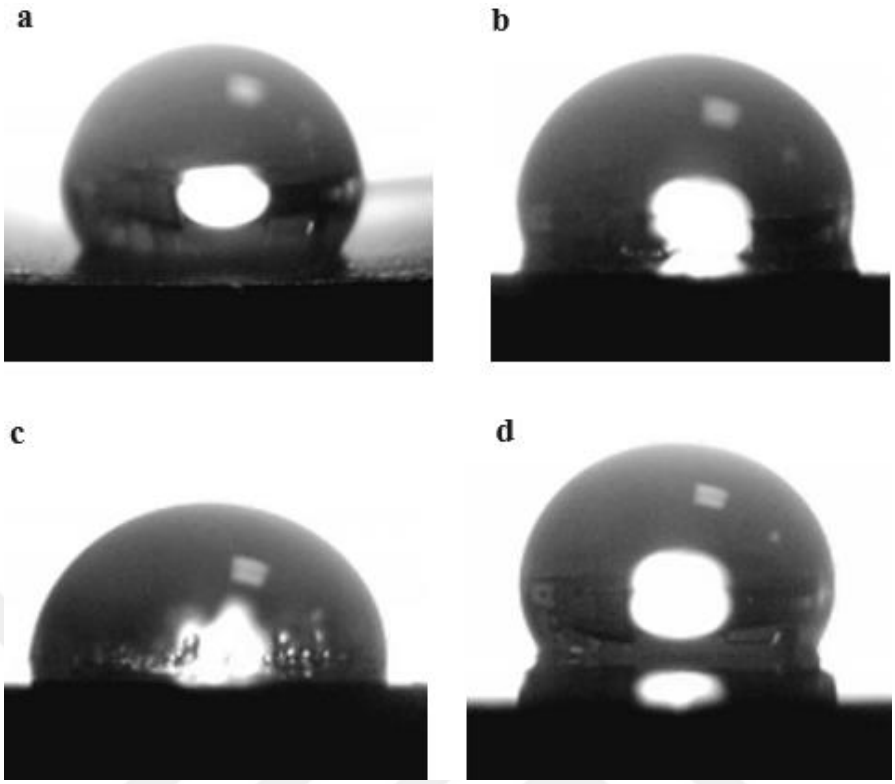


Figure 4.28 Water contact angle images of Group 2. (a) A30-30, (b) A30-60, (c) A30-90, (d) A30-120.

Water contact angle values were measured on the samples at room temperature using a syringe to apply droplets. For each value, three angle measurements were taken, and their average was calculated. The contact angle values ranged from 44.72 to 123.2 degrees. It has been proven that the anodization process imparted hydrophobic properties to the samples. The interaction of surfaces with liquids has been analyzed using the Wenzel and Cassie-Baxter models. These models describe how increasing surface roughness can transform a water-resistant surface into one that is superhydrophobic. The Cassie-Baxter model, in particular, explains the heterogeneous wetting state where air trapped in surface pores surrounds the water. This situation minimizes the solid-water interface and maximizes the air-water interface, causing water droplets on the surface to form a spherical shape (Mokhtari et al., 2017).

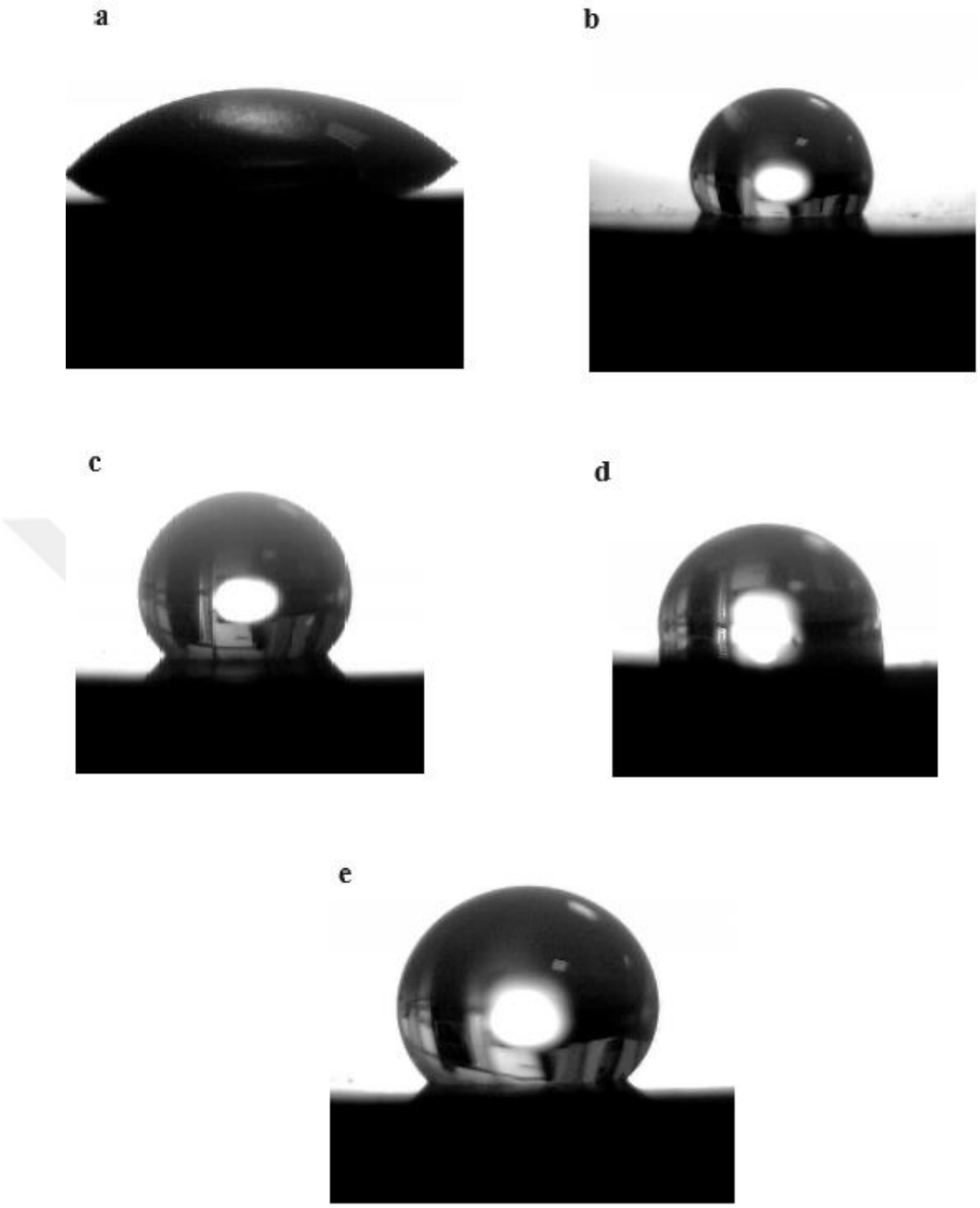


Figure 4.29 Water contact angle images of Group 3. (a) aluminum, (b) NA30-30, (c) NA30-60, (d) NA30-90, (e) NA30-120.

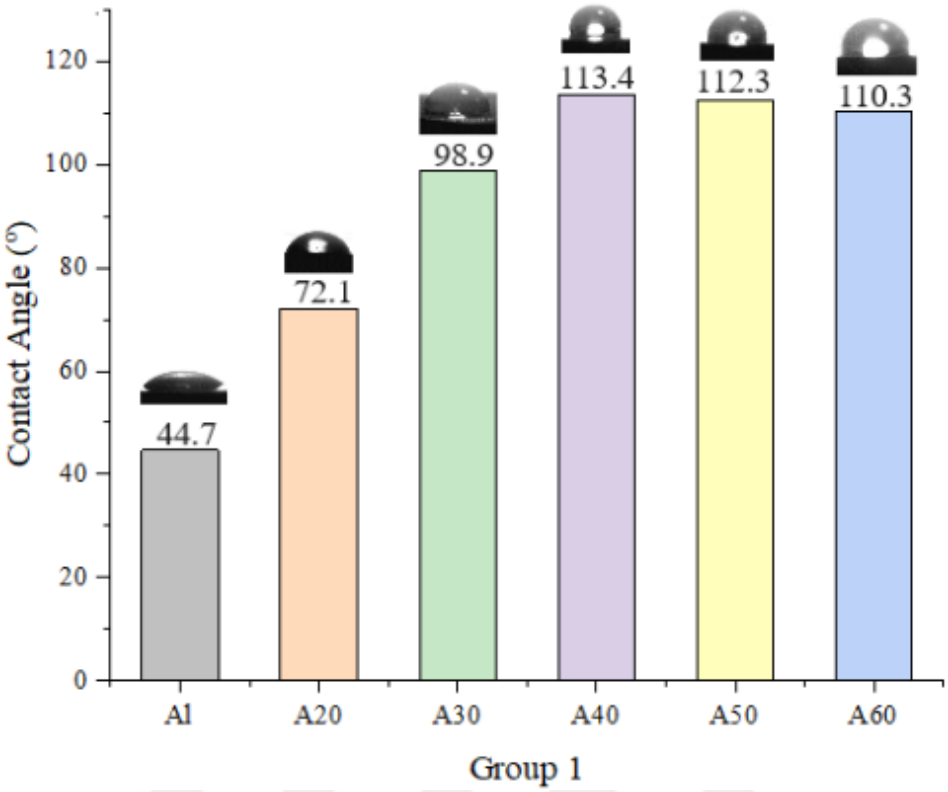


Figure 4.30 Water contact angle values of Group 1.

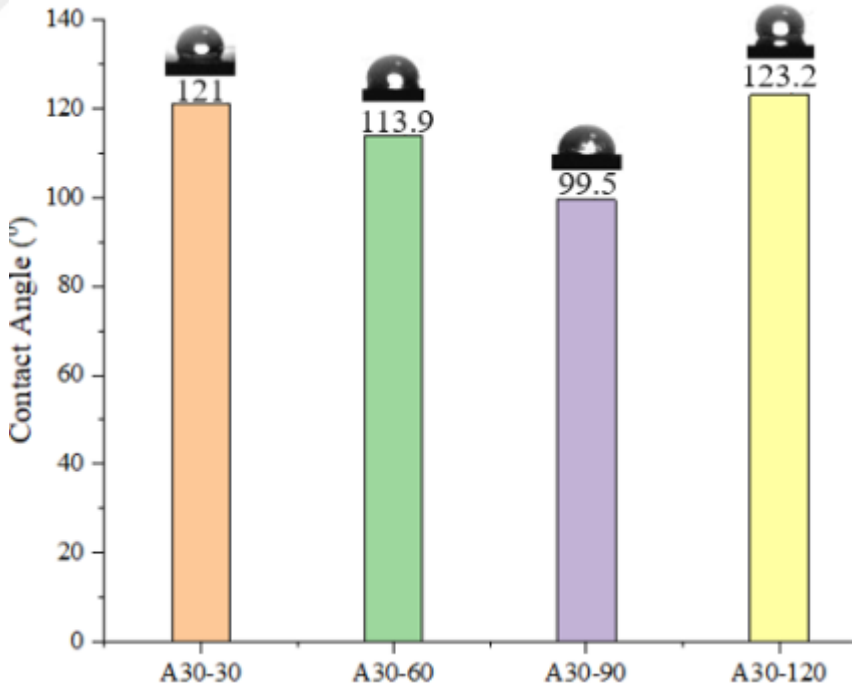


Figure 4.31 Water contact angle values of Group 2.

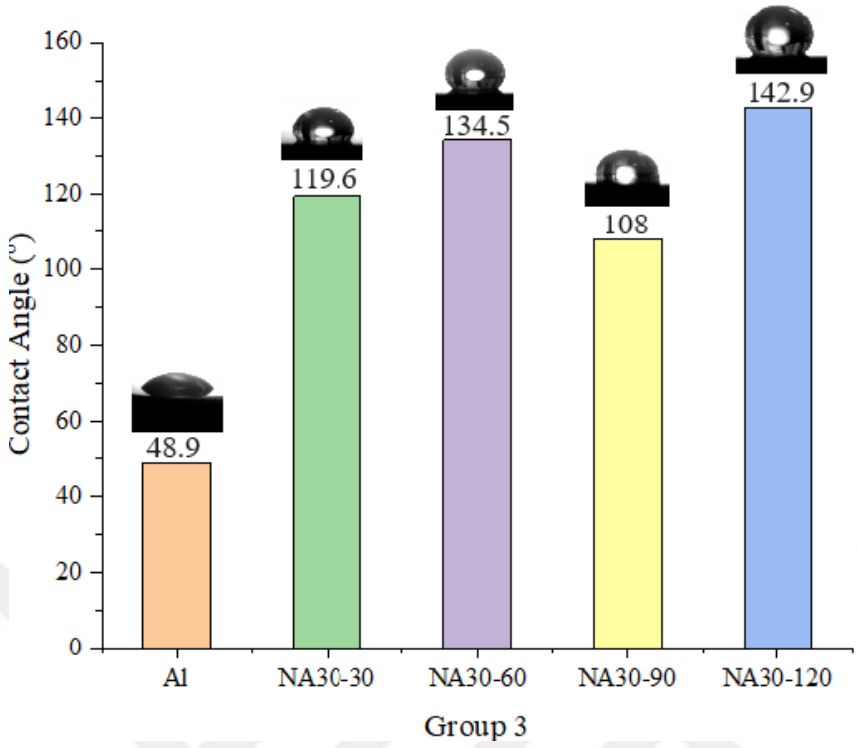


Figure 4.32 Water contact angle values of Group 3.

Figure 4.27 and Figure 4.30 shows that as the voltage increases, hydrophobicity also increases. Hydrophobicity is inversely proportional to the amount of Al in the material. In addition, the adsorption effect of organics in the atmosphere on the oxide film also influences the hydrophobicity. The nano-scale pore structures that trap air in the SEM images of the materials we anodized have imparted hydrophobic properties to the material (Savio et al., 2021). As seen in Figure 4.28 and Figure 4.29, there is an increase in the water contact angle after anodizing; however, it has been observed that this value does not change with the duration of the anodization process. Figure 4.31 and Figure 4.32 graphically shows the contact angle values. Fang and his friends (2018) prepare hydrophobic aluminum oxide film. The results in the literature have shown that the water contact angle does not depend on the oxide layer thickness but only on the pore size (Guo et al., 2013). Since the pore size values, or in other words, the surface air fraction of Group 1 and Group 2 did not change significantly despite the increase in anodization time, the water contact angles also did not change much. Guo and his friends (2013) fabricated AAO with using oxalic acid as an electrolyte and they observed contact angle 114°. As a result, out data consistent with the

literature. The increase in the water contact angle is due to the reduction of the liquid-solid contact area on the top surface or the increase in the liquid-air contact area (Jeong C. et al., 2015). AAO can be utilized as a hydrophilic or hydrophobic surface area for cell proliferation (Davoodi et al., 2020). At the same time Kang and his collagues (2020) use the carbon coating by CVD method in order to obtain anodized aluminum oxide membranes for their hydrophobicity. For membranes with small diameters, water can penetrate the AAO surface more easily. The increase in pore diameter reduces the contact area, thereby increasing the contact angle (Guo et al., 2013).

CHAPTER FİVE
CONCLUSION & FUTURE WORKS

In this study, AAO membranes were obtained at room temperature by a two-step anodization method, divided into three groups with different durations and voltages. The pore diameter, interpore distance, wall thickness, barrier layer thickness, pore density, and porosity values were calculated. Consistent with the literature, it was shown that the pore diameter and interpore distance values depend on the voltage and anodization time, and that these parameters increase with increasing voltage and time. As observed from the SEM images and numerical values, it can be concluded that an anodization duration of 30 minutes is short. Looking at the results of all groups, pore diameters smaller than 50 nm were obtained. Changes in Z-scan and deflection values are also evident in the AFM images compared to untreated aluminum. It has also been shown that the anodization process makes the surface hydrophobic. This study demonstrates that AAO membranes with very small nanopores can be produced simply and cost-effectively. Depending on the type of study, this nanoporous structure can be tailored to the desired condition by changing the voltage, anodization time, and type of electrolyte. AAO membranes are used in biosensors, filtration, sensors, drug delivery, and even cancer therapies. There are many applications of AAOs depending on their pore size, pore distance and length, porosity, surface area, and hardness. This study has provided significant findings by examining the structural properties of AAO membranes.

In future studies, the effects of different electrolyte solutions and varying anodization conditions on the pore structure and mechanical properties of AAO could be examined in more detail. Hardness values can be obtained by performing nanoindentation tests. Furthermore, advanced simulation and modeling studies can be conducted to better understand the formation mechanisms and pore structure dynamics of AAO. Additionally, the effects of functional coatings (such as hydrophobic coatings and metal nanocomposites) and surface modifications could be investigated to improve the surface properties of AAO and make it useful for specific applications.

REFERENCES

Abrahami, S. T. (2016). Cr (VI)-free pre-treatments for adhesive bonding of aerospace aluminium alloys. *Delft University of Technology*.

Aerts, T., Dimogerontakis, T., De Graeve, I., Fransaer, J., & Terryn, H. (2007). Influence of the anodizing temperature on the porosity and the mechanical properties of the porous anodic oxide film. *Surface and Coatings Technology, 201*(16-17), 7310-7317.

Alkire, R. C., Gogotsi, Y., & Simon, P. (2008). *Nanostructured materials in electrochemistry*. John Wiley & Sons.

Ateş, S., Baran, E., & Yazıcı, B. (2018). The nanoporous anodic alumina oxide formed by two-step anodization. *Thin Solid Films*, *648*, 94-102.

Bengough, G. D., & Stuart, J. M. (1923). Improved process of protecting surfaces of aluminium of aluminium alloys. *UK patent*, *223*(994).

Bertin, F., Piccardo, A., Denes, E., Delepine, G., & Tricard, J. (2018). Porous alumina ceramic sternum: a reliable option for sternal replacement. *Annals of Thoracic Medicine*, *13*(4), 226-229.

Bocchetta, P., Sunseri, C., Bottino, A., Capannelli, G., Chiavarotti, G., Piazza, S., & Di Quarto, F. (2002). Asymmetric alumina membranes electrochemically formed in oxalic acid solution. *Journal of applied electrochemistry*, *32*, 977-985.

Bridges, C. R., Schon, T. B., DiCarmine, P. M., & Seferos, D. S. (2013). Template directed synthesis of plasmonic gold nanotubes with tunable IR absorbance. *JoVE (Journal of Visualized Experiments), (74),* e50420.

Brudzisz, A. M., Giziński, D., & Stępniowski, W. J. (2021). Incorporation of ions into nanostructured anodic oxides—Mechanism and functionalities. *Molecules*, *26*(21), 6378.

Chang, J. K., Lin, C. M., Liao, C. M., Chen, C. H., & Tsai, W. T. (2004). Effect of heat-treatment on characteristics of anodized aluminum oxide formed in ammonium adipate solution. *Journal of the Electrochemical Society*, *151*(3), B188.

Chen, W., Wu, J. S., & Xia, X. H. (2008). Porous anodic alumina with continuously manipulated pore/cell size. *ACS nano*, *2*(5), 959-965.

Cheng, C., & Ngan, A. H. W. (2015). Theoretical pore growth models for nanoporous alumina. *Nanoporous alumina: Fabrication, structure, properties and applications*, 31-60.

Cheng, T. C., & Chou, C. C. (2015). The Electrical and Mechanical Properties of Porous Anodic 6061‐T6 Aluminum Alloy Oxide Film. *Journal of Nanomaterials*, *2015*(1), 371405.

Choudhary, R. K., Sreeshma, K. P., & Mishra, P. (2017). Effect of surface roughness of an electropolished aluminum substrate on the thickness, morphology, and hardness of aluminum oxide coatings formed during anodization in oxalic acid. *Journal of Materials Engineering and Performance*, *26*, 3614-3620.

Chu, S. Z., Wada, K., Inoue, S., Isogai, M., Katsuta, Y., & Yasumori, A. (2006). Large-scale fabrication of ordered nanoporous alumina films with arbitrary pore intervals by critical-potential anodization. *Journal of the Electrochemical Society*, *153*(9), B384.

Davoodi, E., Zhianmanesh, M., Montazerian, H., Milani, A. S., & Hoorfar, M. (2020). Nano-porous anodic alumina: Fundamentals and applications in tissue engineering. *Journal of Materials Science: Materials in Medicine*, *31*, 1-16.

Domagalski, J. T., Xifre-Perez, E., & Marsal, L. F. (2021). Recent advances in nanoporous anodic alumina: Principles, engineering, and applications. *Nanomaterials*, *11*(2), 430.

Durmuşoğlu, E. G. (2012) *Nanoporoz Anodik Alüminanın Alüminyum Yüzeyinden Ayırılması*. (Master Thesis, İstanbul Teknik Üniversitesi).

Eessaa, A. K., & El-Shamy, A. M. (2023). Review on fabrication, characterization, and applications of porous anodic aluminum oxide films with tunable pore sizes for emerging technologies. *Microelectronic Engineering*, 112061.

Fadillah, L. (2021). Formation of nanostructured anodic films on iron and their electrode applications (Doctoral dissertation, Hokkaido University).

Fang, C., Pu, M., Zhou, X., Lei, W., Pei, L., & Wang, C. (2018). Facile preparation of hydrophobic aluminum oxide film via sol-gel method. *Frontiers in Chemistry*, *6*, 308.

Flamme, K. E. L., Mor, G., Gong, D., Tempa, T. L., Fusaro, V. A., Grimes, C. A., & Desai, T. A. (2005). Nanoporous alumina capsules for cellular macroencapsulation: transport and biocompatibility. *Diabetes technology & therapeutics*, *7*(5), 684-694.

Giacomello, A., Meloni, S., Chinappi, M., & Casciola, C. M. (2012). Cassie–Baxter and Wenzel states on a nanostructured surface: phase diagram, metastabilities, and transition mechanism by atomistic free energy calculations. *Langmuir*, *28*(29), 10764-10772.

Goh, X. Y., Ong, R. H., Nguyen, P. T., Bai, T., Aw, D., Li, T., ... & Duong, H. M. (2023). Advanced fabrication and multi-properties of aluminum-based aerogels from aluminum waste for thermal insulation and oil absorption applications. *Molecules*, *28*(6), 2727.

Guo, C., Wang, X. W., & Yuan, Z. H. (2013). Pore diameter-dependence wettability of porous anodized aluminum oxide membranes. *Journal of Porous Materials*, *20*, 673-677.

Han, E. D., Kim, B. H., & Seo, Y. H. (2017). Anti-cell adhesion characteristics of nanotextured surface for implantable biomedical device. *International Journal of Precision Engineering and Manufacturing*, *18*, 239-244.

Han, X. Y., & Shen, W. Z. (2011). Improved two-step anodization technique for ordered porous anodic aluminum membranes. *Journal of Electroanalytical Chemistry*, *655*(1), 56-64.

Iwai, M., & Kikuchi, T. (2021). Fabrication of unique porous alumina films with extremely high porosity and an ultra-flat barrier layer by anodizing aluminum in sodium metaborate. *Electrochimica Acta*, *399*, 139440.

Jeong, C., Lee, J., Sheppard, K., & Choi, C. H. (2015). Air-impregnated nanoporous anodic aluminum oxide layers for enhancing the corrosion resistance of aluminum. *Langmuir*, *31*(40), 11040-11050.

Jessensky, O., Müller, F., & Gösele, U. (1998). Self-organized formation of hexagonal pore arrays in anodic alumina. *Applied physics letters*, *72*(10), 1173-1175.

Juhl, A. D. (2003). Theoretical Introduction to Pulse Anodizing. AAC, *San Francisco*.

Kang, G. S., Baek, Y., & Yoo, J. B. (2020). Relationship between surface hydrophobicity and flux for membrane separation. *RSC advances*, *10*(66), 40043-40046.

Kavas, B. (2011) *Nanoporoz Anodik Alüminyum Oksitin Mekanik Özellikleri Ve Sürtünme Davranışı*. (Master's Thesis, İstanbul Teknik Üniversitesi).

Keller, F., Hunter, M. S., & Robinson, D. L. (1953). Structural features of oxide coatings on aluminum. *Journal of the Electrochemical Society*, *100*(9), 411.

Khan, H., Yerramilli, A. S., D'Oliveira, A., Alford, T. L., Boffito, D. C., & Patience, G. S. (2020). Experimental methods in chemical engineering: X‐ray diffraction spectroscopy—XRD. *The Canadian journal of chemical engineering*, *98*(6), 1255-1266.

Kikuchi, T., Kunimoto, K., Ikeda, H., Nakajima, D., Suzuki, R. O., & Natsui, S. (2019). Fabrication of anodic porous alumina via galvanostatic anodizing in

alkaline sodium tetraborate solution and their morphology. *Journal of electroanalytical chemistry*, *846*, 113152.

Kikuchi, T., Nakajima, D., Nishinaga, O., Natsui, S., & O Suzuki, R. (2015). Porous aluminum oxide formed by anodizing in various electrolyte species. *Current nanoscience*, *11*(5), 560-571.

Kovaleva, E. G., Molochnikov, L. S., Tambasova, D., Marek, A., Chestnut, M., Osipova, V. A., & Smirnov, A. I. (2020). Electrostatic properties of inner nanopore surfaces of anodic aluminum oxide membranes upon high temperature annealing revealed by EPR of pH-sensitive spin probes and labels. *Journal of Membrane Science*, *604*, 118084.

Ku, C. A., Yu, C. Y., Hung, C. W., & Chung, C. K. (2023). Advances in the Fabrication of Nanoporous Anodic Aluminum Oxide and Its Applications to Sensors: A Review. *Nanomaterials*, *13*(21), 2853.

Kutlu, F. (2014). *Anodik alüminyum oksit (AAO) nano kalıpların yapımı* [Master's thesis]. Marmara Universitesi.

Lee, W. (2010). The anodization of aluminum for nanotechnology applications. JOM Journal of the Minerals, *Metals and Materials Society*, *62*(6), 57.

Lee, W., & Park, S. J. (2014). Porous anodic aluminum oxide: anodization and templated synthesis of functional nanostructures. *Chemical reviews*, *114*(15), 7487-7556.

Lee, W., Ji, R., Gösele, U., & Nielsch, K. (2006). Fast fabrication of long-range ordered porous alumina membranes by hard anodization. *Nature materials*, *5*(9), 741-747.

Lee, W., Kim, J. C., & Gösele, U. (2010). Spontaneous current oscillations during hard anodization of aluminum under potentiostatic conditions. *Advanced functional materials*, *20*(1), 21-27.

Leontiev, A. P., Roslyakov, I. V., & Napolskii, K. S. (2019). Complex influence of temperature on oxalic acid anodizing of aluminium. *Electrochimica Acta*, *319*, 88-94.

Li, J., Zhang, Z., Li, Y., Ma, Y., Chen, L., Zhang, Z., & Sun, R. (2016). Self-organization process of aluminum oxide during hard anodization. *Electrochimica Acta*, *213*, 14-20.

Ling, Z., & Li, Y. (2015). Mechanisms of nanoporous alumina formation and self-organized growth. *Nanoporous alumina: Fabrication, structure, properties and applications*, 1-30.

Liu, S., Tian, J., & Zhang, W. (2021). Fabrication and application of nanoporous anodic aluminum oxide: a review. *Nanotechnology*, *32*(22), 222001.

Maawad, E. K. S. (2013). *Residual Stress Analysis and Fatigue Behavior of Mechanically Surface Treated Titanium Alloys:(Vom Promotionsausschuss Der Technischen Universität Clausthal Im Jahr 2012 Als Dissertation Angenommene Arbeit)*. Helmholtz-Zentrum Geesthacht.

Manzoor, S., Ashraf, M. W., Tayyaba, S., & Hossain, M. K. (2021). Recent progress of fabrication, characterization, and applications of anodic aluminum oxide (AAO) membrane: A review. *arXiv preprint arXiv:2112.08450*.

Marchal, D. (2003). Small-angle neutron scattering by porous alumina membranes made of aligned cylindrical channels. *Journal of applied crystallography*, *36*(3), 713-717.

Martín, J., Manzano, C. V., Caballero-Calero, O., & Martín-González, M. (2013). High-aspect-ratio and highly ordered 15-nm porous alumina templates. *ACS applied materials & interfaces*, *5*(1), 72-79.

Masuda, H. M. H., & Satoh, M. S. M. (1996). Fabrication of gold nanodot array using anodic porous alumina as an evaporation mask. *Japanese Journal of Applied Physics*, *35*(1B), L126.

Masuda, H., Hasegwa, F., & Ono, S. (1997). Self‐ordering of cell arrangement of anodic porous alumina formed in sulfuric acid solution. *Journal of the electrochemical society*, *144*(5), L127.

Masuda, H., Yada, K., & Osaka, A. (1998). Self-ordering of cell configuration of anodic porous alumina with large-size pores in phosphoric acid solution. *Japanese Journal of Applied Physics*, *37*(11A), L1340.

Miller, M. A. (1960). *U.S. Patent No. 2,920,018*. Washington, DC: U.S. Patent and Trademark Office.

Mobasser, S., & Firoozi, A. A. (2016). Review of nanotechnology applications in science and engineering. *J Civil Eng Urban*, *6*(4), 84-93.

Mohamed, O. (2019) *Synthesis and Characterization of Al6061/Al2O3 Metal Matrix Nanocomposites Fabricated by Stir-Casting* [Published doctoral dissertation]. Clausthal University.

Mokhtari, S., Karimzadeh, F., Abbasi, M. H., & Raeissi, K. (2017). Development of super-hydrophobic surface on Al 6061 by anodizing and the evaluation of its corrosion behavior. *Surface and Coatings Technology*, *324*, 99-105.

Morel, X., Rias, A., Briat, B., El Aouni, A., D'Hermies, F., Adenis, J. P., & Renard, G. (1998). Biocompatibility of a porous alumina orbital implant. Preliminary results of an animal experiment. *Journal Francais D'ophtalmologie*, *21*(3), 163-169.

Nielsch, K., Choi, J., Schwirn, K., Wehrspohn, R. B., & Gösele, U. (2002). Self-ordering regimes of porous alumina: the 10 porosity rule. *Nano letters*, *2*(7), 677-680.

Nishinaga, O., Kikuchi, T., Natsui, S., & Suzuki, R. O. (2013). Rapid fabrication of self-ordered porous alumina with 10-/sub-10-nm-scale nanostructures by selenic acid anodizing. *Scientific reports*, *3*(1), 2748.

Oh, H. J., Park, G. S., Kim, J. G., Jeong, Y., & Chi, C. S. (2003). Surface roughness factor of anodic oxide layer for electrolytic capacitors. *Materials chemistry and physics*, *82*(2), 331-334.

Ono, S., & Masuko, N. (1992). The duplex structure of cell walls of porous anodic films formed on aluminum. *Corrosion science*, *33*(3), 503-507.

Ono, S., & Masuko, N. (2003). Evaluation of pore diameter of anodic porous films formed on aluminum. *Surface and Coatings Technology*, *169*, 139-142.

Ono, S., Saito, M., & Asoh, H. (2005). Self-ordering of anodic porous alumina formed in organic acid electrolytes. *Electrochimica Acta*, *51*(5), 827-833.

Ono, S., Saito, M., Ishiguro, M., & Asoh, H. (2004). Controlling factor of self-ordering of anodic porous alumina. *Journal of the Electrochemical Society*, *151*(8), B473.

O'sullivan, J. P., & Wood, G. C. (1970). The morphology and mechanism of formation of porous anodic films on aluminium. *Proceedings of the Royal Society of London. A. Mathematical and Physical Sciences*, *317*(1531), 511-543.

Palibroda, E. (1984). Le mécanisme du développement de l'oxyde poreux de l'aluminium II. L'oxyde poreux et la tension électrique de la couche barrière. *Surface technology*, *23*(4), 341-351.

Pandey, A., Dalal, S., Dutta, S., & Dixit, A. (2021). Structural characterization of polycrystalline thin films by X-ray diffraction techniques. *Journal of Materials Science: Materials in Electronics*, *32*, 1341-1368.

Paolini, G., Masoero, M., Sacchi, F., & Paganelli, M. (1965). An investigation of porous anodic oxide films on aluminum by comparative adsorption, gravimetric and electronoptical measurements. *Journal of the electrochemical Society*, *112*(1), 32.

Pashchanka, M., & Schneider, J. J. (2016). Self-ordering regimes of porous anodic alumina layers formed in highly diluted sulfuric acid electrolytes. *The Journal of Physical Chemistry C*, *120*(27), 14590-14596.

Paz Martínez-Viademonte, M., Abrahami, S. T., Hack, T., Burchardt, M., & Terryn, H. (2020). A review on anodizing of aerospace aluminum alloys for corrosion protection. *Coatings*, *10*(11), 1106.

Poinern, G. E. J., Ali, N., & Fawcett, D. (2011). Progress in nano-engineered anodic aluminum oxide membrane development. *Materials*, *4*(3), 487-526.

Popat, K. C., Chatvanichkul, K. I., Barnes, G. L., Latempa Jr, T. J., Grimes, C. A., & Desai, T. A. (2007). Osteogenic differentiation of marrow stromal cells cultured on nanoporous alumina surfaces. *Journal of biomedical materials research Part A*, *80*(4), 955-964.

Quebbou, Z., Chafi, M., & Omari, L. E. H. (2021). Corrosion resistance of 5005 aluminum alloy by anodizing treatment in a mixture of phosphoric and boric acids. *Materials Today: Proceedings*, *37*, 3854-3859.

Ruiz-Clavijo, A., Caballero-Calero, O., & Martín-González, M. (2021). Revisiting anodic alumina templates: From fabrication to applications. *Nanoscale*, *13*(4), 2227-2265.

Sammi, H., Nair, R. V., & Sardana, N. (2021). Recent advances in nanoporous AAO based substrates for surface-enhanced raman scattering. *Materials Today: Proceedings*, *41*, 843-850.

Savio, L., Bhavitha, K. B., Bracco, G., Luciano, G., Cavallo, D., Paolini, G., ... & Smerieri, M. (2021). Correlating hydrophobicity to surface chemistry of microstructured aluminium surfaces. *Applied Surface Science*, *542*, 148574.

Schwirn, K., Lee, W., Hillebrand, R., Steinhart, M., Nielsch, K., & Gösele, U. (2008). Self-ordered anodic aluminum oxide formed by H2SO4 hard anodization. *ACS nano*, *2*(2), 302-310.

Seo, Y., & Jhe, W. (2007). Atomic force microscopy and spectroscopy. *Reports on Progress in Physics*, *71*(1), 016101.

Shamsuddin, S. A., Derman, M. N., Hashim, U., & Tahir, M. F. M. (2021, May). Study on the effects of anodizing voltage to the AAO thin film dimensional properties synthesized by single step anodization method. In *AIP Conference Proceedings* (Vol. 2339, No. 1). AIP Publishing.

Stępniowski, W. J., & Bojar, Z. (2011). Synthesis of anodic aluminum oxide (AAO) at relatively high temperatures. Study of the influence of anodization conditions on the alumina structural features. *Surface and Coatings technology*, *206*(2-3), 265-272.

Sulka, G. D. (2008). Highly ordered anodic porous alumina formation by self-organized anodizing. *Nanostructured materials in electrochemistry*, 1-116.

Sulka, G. D., & Parkoła, K. G. (2006). Anodising potential influence on well-ordered nanostructures formed by anodisation of aluminium in sulphuric acid. *Thin Solid Films*, *515*(1), 338-345.

Sulka, G. D., & Parkoła, K. G. (2007). Temperature influence on well-ordered nanopore structures grown by anodization of aluminium in sulphuric acid. *Electrochimica Acta*, *52*(5), 1880-1888.

Sulka, G. D., & Stępniowski, W. J. (2009). Structural features of self-organized nanopore arrays formed by anodization of aluminum in oxalic acid at relatively high temperatures. *Electrochimica Acta*, *54*(14), 3683-3691.

Syamdri, F. D., & Wibowo, R. (2020). The effect of sulphuric acid and oxalic acid on the formation of anodic aluminium oxide templates using two-step anodization method. In *Journal of Physics: Conference Series* (Vol. 1442, No. 1, p. 012063). IOP Publishing.

Taylor, C. S., Tucker, C. M., & Edwards, J. D. (1945). Anodic coatings with crystalline structure on aluminum. *Transactions of the Electrochemical Society*, *88*(1), 325.

Terryn, H. (1987). *Electrochemical Investigation of AC Electrograining of Aluminium and its Porous Anodic Oxidation*.

Thompson, G. E. (1997). Porous anodic alumina: fabrication, characterization and applications. *Thin solid films*, *297*(1-2), 192-201.

Tu, G. C., & Huang, L. Y. (1987). Hard anodizing of 2024 aluminium alloy using pulsed DC and AC power. *Transactions of the IMF*, *65*(1), 60-66.

Uchi, H., Kanno, T., & Alwitt, R. S. (2001). Structural features of crystalline anodic alumina films. *Journal of the Electrochemical Society*, *148*(1), B17.

Var, İ., & Sağlam, S. (2015). Gıda Endüstrisinde Nanoteknoloji Uygulamaları. *Gıda, 40*(2), 101-108.

Wang, Q., Long, Y., & Sun, B. (2013). Fabrication of highly ordered porous anodic alumina membrane with ultra-large pore intervals in ethylene glycol-modified citric acid solution. *Journal of Porous Materials*, *20*, 785-788.

Wei, Q., Fu, Y., Zhang, G., Yang, D., Meng, G., & Sun, S. (2019). Rational design of novel nanostructured arrays based on porous AAO templates for electrochemical energy storage and conversion. *Nano Energy*, *55*, 234-259.

Wernick, S., & Pinner, R. (1987). The surface treatment and finishing of aluminium and its alloys.

Wood, G. C., Skeldon, P., Thompson, G. E., & Shimizu, K. (1996). A model for the incorporation of electrolyte species into anodic alumina. Journal of the *Electrochemical Society*, *143*(1), 74.

Xu, X., Liu, Z., Zhang, B., Chen, H., Zhang, J., Wang, T., ... & Huang, P. (2019). Effect of Mn content on microstructure and properties of 6000 series aluminum alloy. *Applied Physics A*, *125*, 1-9.

Xu, Y., Thompson, G. E., Wood, G. C., & Bethune, B. (1987). Anion incorporation and migration during barrier film formation on aluminium. *Corrosion science, 27*(1), 83-102.

Ying, L., Xie, Y., Fu, Z., Shi, H., & Wang, G. (2019). Study on direct current electro-deposition of copper nanowires in anodic alumina membrane pores. *Coatings, 9*(6), 378.

Zaraska, L., Brudzisz, A., Wierzbicka, E., & Sulka, G. D. (2016). The effect of electrolyte change on the morphology and degree of nanopore order of porous alumina formed by two-step anodization. *Electrochimica Acta, 198*, 259-267.

Zaraska, L., Stępniowski, W. J., Ciepiela, E., & Sulka, G. D. (2013). The effect of anodizing temperature on structural features and hexagonal arrangement of nanopores in alumina synthesized by two-step anodizing in oxalic acid. *Thin Solid Films, 534*, 155-161.

Zaraska, L., Sulka, G. D., Szeremeta, J., & Jaskuła, M. (2010). Porous anodic alumina formed by anodization of aluminum alloy (AA1050) and high purity aluminum. *Electrochimica Acta, 55*(14), 4377-4386.

Zhang, H., Yin, L., Shi, S., Liu, X., Wang, Y., & Wang, F. (2015). Facile and fast fabrication method for mechanically robust superhydrophobic surface on aluminum foil. *Microelectronic Engineering, 141*, 238-242.

Zhu, C., Zheng, Z., Cao, F., Xiang, Y., & Peng, Z. (2021). High-temperature properties of Al2O3/SiO 2 composites. *Journal of sol-gel science and technology, 97*, 63-70.